Spectropolarimetry of Active Regions on the Sun

A Thesis

Submitted for the Degree of

Doctor of Philosophy

In

Department of Physics

Mangalore Univerity

by

Nagaraju, K.

Indian Institute of Astrophysics

Bangalore

June 2008

Declaration

I hereby declare that this thesis, submitted to Mangalore University, Mangalore, for the award of a Ph.D. degree, is a result of the investigations carried out by me at Indian Institute of Astrophysics, Bangalore, under the supervision of Professor K. E. Rangarajan. The results presented herein have not been subject to scrutiny, by any university or institute, for the award of a degree, diploma, associateship or fellowship whatsoever.

Nagaraju, K.

(Candidate)

Indian Institute of Astrophysics

Bangalore-560034, India

Certificate

This is to certify that the thesis entitled **'Spectropolarimetry of active regions on the Sun'** submitted to Mangalore University by **Mr. Nagaraju, K.** for the award of the degree of Doctor of Philosophy in the faculty of Physics, is based on the results of the investigations carried out by him under my supervision and guidance, at the Indian Institute of Astrophysics. This thesis has not been submitted for the award of any degree, diploma, associateship, fellowship, etc. of any university or institute.

Prof. K. E. Rangarajan

(Supervisor)

Indian Institute of Astrophysics

Bangalore-560034, India

Acknowledgments

I am greatly indebted to my supervisor, Dr. K.E. Rangarajan for his invaluable advice at appropriate times and constant guidance all through my PhD career. His ready availability and willingness to discuss with me, irrespective of the hour of the day, helped me stay focussed at my work.

I thank Prof. Hasan, the Director, Indian Institute of Astrophysics, for his encouragement and support extended to our instrumentation project. Also, for all necessary facilities provided for my research work. I would also like to thank the Chairman and members of Board of Graduate Studies for their kind help in various forms throughout my PhD career at IIA.

I thank Prof. K. M. Balakrishna, the current Chairman of the Physics department, Mangalore University and also the earlier chairmen for their kind help at all stages of my communication to Mangalore University. I would like to express my great appreciation for the efficiency of the administration at Mangalore University which helped in smooth processing of my PhD registration and at the later stages as well. Special thanks to Ms. Sonia for her valuable information regarding my PhD registration procedures.

A few lines are too short to make a complete account of my deep appreciation for my collaborator, Dr. Sankarasubramanian who is currently working in ISRO,

Bangalore. His zeal towards this work is quite evident in the number of hours per week he extracted from his busy schedule for the discussions with me. Continuous interactions with him has helped to learn the basics of solar physics and instrumentation. His expertise in this field, which he generously shared with me helped me to get acquainted with various methods of analyzing data.

I wish to thank Prof. K. N. Nagendra as it was a great pleasure to be associated with him. The depth of knowledge he possesses has been an inspiration for me and a major contributor to my learning of radiative transfer in detail. This has helped me in various stages of my work.

I am grateful to Prof. Sharath Ananthamurthy Bangalore University and G. S. D. Babu, MPBIFR, Bangalore. It is their constant encouragement which set me in the track of going for a PhD.

Thanks to Mr. P. U. Kamath for the polarimeter design, fabrication and installation at Kodaikanal for observations. Thanks to Mr. P. K. Mahesh who along with P. U. Kamath helped me in procuring the laboratory equipments. Thanks also to Mr. Samson and Mr. Thimmaiah for the fabrication of a prototype polarimeter which was a starting point for a more sophisticated polarimeter which is currently installed at Kodaikanal. Thanks to Mr. George for his ready availability to fix the mechanical problems which we often used to encounter during the observations.

I thank Dr. K. B. Ramesh from whom I learnt a lot about basics of optics and

solar physics. Without his help it would have been a difficult task for the successful completion of the laboratory experiments. I am grateful to Prof. Jagdev Singh for lending some of the instruments required for imaging setup at the focal plane of KTT which helped in simultaneous spectropolarimetry and imaging. Also, his constant encouragement and support for our project is greatly appreciated here. Thanks to Dr. Raghavendra Prasad for providing some of the laboratory equipments as well as the laboratory space to carry out experiments to study the properties of optical components used in the polarimeter. Special thanks to Dr. Ravinder Kumar Banyal who helped me to carry out these experiments. I thank Mr. A. V. Ananth for his support for our instrumentation project and for providing lab space to carry out the experiment to study the polarimetric efficiency.

The efforts and enthusiasm of Mr. Devendran and Mr. Hariharan and their assistance in carrying out solar observations is a great deal of help in this thesis work. Because of which we could carry out several observations which helped in getting a good quality data presented in this thesis. Thanks to Mr. S. Ramamoorthy for taking care of power needs during observations and his company all through my stay at Kodaikanal. I extend my thanks to Prof. S. S. Gupta, Dr. Sundararaman and Mr. Basha for providing me adequate facilities during my stay at Kodaikanal. Selevendran, Kumarvelu, Loganathan and Michael are acknowledged here for the friendly environment provided by them during my stay over there.

Thanks to Dr. B. A. Varghese and Mr. J. S. Nathan for their help in fixing the

computer related problems. Computer support group is thanked here for their their kind help in all aspects of computer related problems. Special thanks to Fayaz who helped me printing this thesis.

Thanks to Librarian, library staff and trainees because of whom I hardly faced any problem in getting the required documents. I also thank Library staff of Kodaikanal for their help in accessing the library books during my stay at Kodaikanal.

I thank Dr. Dipankar Banerjee, who has been an encouragement and support throughout the period of my work. Thanks also to Dr. S. P. Rajaguru for his friendly discussions which made my stay at IIA very lively. I would like to thank Dr. Ravindra for providing us the extrapolated magnetic field strengths in the higher layers which helped in strengthening our arguments in a paper which forms a part of this thesis. Thanks to Dr. Balasubramaniam, interacting with whom clarified my doubts regarding H α line formation. Hector Socas Novarro's help in sorting out some of the problems related to Stokes inversion is acknowledged here. Thanks to Han Uitenbroek for providing his 'RH' radiative transfer code which helped me in gaining more understanding of the H α spectral line formation. Thanks to High Altitude Observatory for making available the Stokes inversion codes as well as Instituto de Astrofsica de Canarias group for the SIR inversion code. Thanks to *Hinode* and *SOHO* group for making available the data which helped us to validate the measurements at Kodaikanal.

I thank all Ph.D students who helped me in various stages of my thesis work. Thanks also to the project students, research and engineering trainees who made my stay in IIA enjoyable. I thank all the scientific staff at IIA, interacting with whom I gained good knowledge about Astronomy and Astrophysics. The administrative and technical staff at IIA are thanked for providing adequate facilities for my stay in IIA. Thanks to all my family members for their unwavering support during my PhD career.

Abstract

The production, evolution and dissipation of the magnetic field on the Sun is a fascinating field of research in solar physics. Apart from this, the magnetic field play a major role in processes like solar eruptions such as flares and coronal mass ejections. Prediction of such eruptions on the Sun requires the precise information of the magnetic field and associated dynamics. Spectropolarimetry is a powerful diagnostic tool to understand such dynamics associated with the magnetic field. The solar telescope at Kodaikanal equipped with a high dispersion spectrograph provides an opportunity to measure the magnetic fields through spectropolarimetry with an addition of a polarimeter.

As part of this thesis work a dual-beam polarimeter was designed, fabricated and installed as a backend instrument to the spectrograph at Kodaikanal Tower Telescope (KTT) for the spectropolarimetric observations on the Sun. The polarimeter consists of a Polarizing beam displacer (PBD) and two waveplates out of which one acts as a quarter- and other as a half- waveplate at the design wavelength (λ6300). In chapter 1, we discuss about the modulation/demodulation scheme suitable for this polarimeter setup is discussed. Out of various schemes studied for the measurement of a general polarization state of the light using this polarimeter, an eight stage modulation scheme was found to be appropriate Nagaraju et al. [2007]. This scheme requires eight successive intensity measurements to obtain one set of Stokes parameters, viz I, Q, U and V. In this scheme, the four Stokes parameters are

weighted equally in all the eight stages of modulation resulting in total polarimetric efficiency of unity. The gain table error inherent in dual beam system is reduced by using the well known beam swapping technique ([Donati et al., 1990, Semel et al., 1993, Bianda et al., 1998]. The wavelength dependent polarimetric efficiencies of the polarimeter in measuring Stokes parameters due to the chromatic nature of the waveplates are studied in detail. Laboratory experiments were carried out in order to verify the wavelength dependence of the efficiencies of the polarimeter. The modulation scheme presented in this chapter produces better Stokes Q and V efficiencies for wavelengths larger than the design wavelength whereas Stokes U has better efficiency in the shorter wavelength region.

The observational setup for simultaneous spectropolarimetry and imaging of a region-of-interest (ROI) along with data reduction and analysis procedures are described in chapter 3. The dual-beam polarimeter setup described above is placed in front of the spectrograph slit. For simultaneous imaging, a part of the beam entering the polarimeter is channeled in the perpendicular direction using a non-polarizing beam splitter. The images are obtained in wide wavelength band in the redder side of the visible spectrum. The band width of the filters used for imaging is about 800 Å. Spectroplarimetric data reduction involves regular dark and flat corrections. Further these data are accounted for polarimeter and telescope responses. The data are corrected for polarimeter response using the calibration data obtained almost on daily basis during the observations. The telescope response is corrected using a telescope model developed by Balasubramaniam et al. [1985] and Sankarasubramanian

[2000]. Further, residual cross-talks among Stokes parameters are corrected using a statistical method [Sanchez Almeida and Lites, 1992, Schlichenmaier and Collados, 2002].

The data analysis procedures discussed in this chapter include the COG method for LOS velocity and magnetic field measurements, Milne-Eddington inversion for deriving vector magnetic field at the photosphere and weak-field-approximation method to derive vector magnetic field at the chromosphere.

In chapter 3, we also describe the experiments that were carried out to characterize the measurements at KTT. An experiment was carried out to measure the spectral resolution of the spectrograph at KTT as well as to optimize the slit width. A He-Ne laser source (6328 Å) was used fofor this experiment. It was found through this experiment that the slit width of 48 μ is optimum for the spectrograph setup at KTT and the corresponding spectral resolution is 32.47 mÅ. From another experiment to study the behavior of the noise in the polarization data with respect to the exposure time, it was found that the noise in the measured Stokes parameters is mostly limited by the photon noise. It was confirmed through this experiment that the precision in the polarization measurement can be achieved better than 0.1 % by increasing the exposure time implying that the polarimeter is photon starved. However, the polarimetric calibration accuracy is limited to 0.3% for Stokes-Q, 0.36% for Stokes-U and 0.34% for Stokes-V parameter, which is mostly attributed to the uncertainty in the retardance of the calibration retarder. The photospheric magnetic field mea-

surements at KTT matches very will with that of space based spectropolarimetric measurements by *Hinode* after a spatial smearing of *Hinode* data by $5.12'' \times 5.12''$.

Spectropolarimetric observations of several active regions have been carried out around H α (λ6563) spectral region. This wavelength region contains two lines which can be used to study the magnetic coupling between the photosphere and chromosphere. Out of two lines in this wavelength region, one is H_α itself, which forms at the chromospheric heights, and the other is Fe I line at 6569 Å, which forms at the photospheric heights. Since the wavelength separation between these two lines is only 7 Å, it was possible to record them simultaneously by the charge coupled device (CCD) detector available at KTT. Hence the analysis of these two lines provides co-temporal and co-spatial information at photosphere and chromosphere.

In chapter 4, structuring of magnetic field at the photosphere and chromosphere is discussed above three active regions viz., NOAA 10875 (AR1), 10940 (AR2) and 10941 (AR3). The umbra of AR1 possess 3 to 4 light bridges with partially surrounded penumbra. However, it is an isolated sunspot. AR2 consists of a relatively round and simple sunspot but, surrounded by the activity which exhibit opposite polarity to the main sunspot. On the other hand, AR3 is an isolated, simple and round sunspot. For all three sunspots analyzed in this thesis, the magnetic field measured at the photosphere is consistent with the well known distribution, meaning, the field strength is strongest in the central umbra and decreases gradually towards the periphery of the sunspot. On the other hand, field inclination is close to local

vertical and gradually increases along the radius of the sunspot. The magnetic field topology inferred through H α observations above these sunspots are consistent with the X-ray and EUV structures. The EUV structures observed by *SOHO*/EIT show highly complicated structures, while AR2 exhibit loop structures with one of their foot points located in the main sunspot and other in the nearby activity. On the other hand, AR3 exhibit fountain like structure which is typical of a simple isolated sunspot.

In chapter 5, the velocity stratification at the photosphere and chromosphere above the active regions AR1, AR2 and AR3 is discussed. All the three spots studied in this chapter exhibit the velocity structure which is consistent with the well known Evershed effect at the photosphere. But, at the chromosphere, velocity structure is consistent with the inverse Evershed effect only in AR1, where as AR2 and AR3 do not exhibit any such systematic pattern. They show mix of up- and downflows distributed in a random manner. A possible explanation for this is discussed in this chapter.

The velocity gradients at the photosphere and chromosphere are studied using the bisector technique applied to Stokes-I profiles of Fe I line at λ6569 and H α respectively. The velocity gradients are derived using the differences in wavelength positions of line wing and core side bisectors. At the photosphere, a strip of negative velocity gradients are observed around the central penumbral region.

From the bisector analysis of Hα Stokes-I profiles, a monotonic increase in the velocity gradients towards the central umbra is observed in all the three spots. The magnitude of the velocity gradients of all the three spots are comparable and show similar kind of functional form with respect to the magnetic field strengths though the magnetic field topology above these spots are different from each other. However, the velocity maps corresponding to the individual bisectors with respect to central umbra show different structures for these spots. The velocity structures at lower and higher layers above AR1 are similar, where as flow reversal is observed for AR2, with lower layers showing redshifts and higher layers showing blue shifts with respect to the central umbra. The change over from redshifts to blueshifts is gradual. Above AR3, the velocity pattern at the higher layers is more or less similar to that of lower layers. At few locations, AR3 exhibit flow reversals.

In this chapter we also discuss about the results from Stokes-V amplitude asymmetries. The amplitude asymmetries are smaller in the umbral photosphere compared to the penumbral photosphere. In the umbral chromosphere, the Stokes-V amplitude asymmetries are larger compared to their photospheric counterparts. Possible explanations for this larger amplitude asymmetries in the umbral chromosphere are discussed. One interesting point observed regarding the distribution of the amplitude asymmetry over the sunspots studied in this thesis is that, large number of points have positive amplitude asymmetry for positive a polarity sunspot and negative amplitude asymmetry for negative a polarity sunspots.

Contents

List of Figures

List of Tables

Chapter 1

Introduction

Sun is the nearest star and a major energy source for life on the Earth. Thus the energy output from the Sun is very important in sustaining life on the Earth. This energy output, generally known as the total solar irradiance, is known to vary with time and is well correlated with the sunspot cycle [Foukal et al., 2006, Tapping et al., 2007]. Sunspot cycle (also known as solar cycle) is a periodic variation of sunspot number with time and the period of variation is $\approx$ 11 years [Solanki, 2003]. The variation in the total solar irradiance is small ($\approx 1\%$) and this may not have immediate effect on the activities on the Earth [Foukal et al., 2006]. But, the activities like sudden burst of energy from the Sun can have considerable impact on our daily activities. These sudden bursts of energy, known as solar eruptions, are generally associated with the magnetic fields. They are maximum during the solar maximum.

The energetic particles released during these eruptions can, when they are Earth directed, disrupt telecommunications, failure of power grids, problematic to human's space activities and etc. The prediction of the energetic phenomenon on the Sun has tremendous usefulness in preventing these damages. Also, in a more general sense, the activities on the Sun have direct impact on weather forecast on the Earth. Prediction of these phenomena requires a detailed knowledge of the magnetic field related dynamics in the solar atmosphere and interior.

1.1 Velocity and Magnetic Fields in Solar Atmosphere

The systematic study of the magnetic fields on the Sun was started around 1611 by Galileo by using the then newly invented telescope. But, it was not known until the discovery of George Ellery Hale in 1908 that the sunspots are regions of strong magnetic field [Hale, 1908]. Since then, the magnetic field has become firmly established as the root cause of the sunspot phenomenon. Sunspots are relatively cool and appear dark on the surface of the Sun. Each sunspot is characterized by a dark core, the umbra, and a less dark halo, the penumbra. More complicated distribution of the magnetic field (appears as cluster of dark regions on the visible surface of the Sun) is collectively known as active region. Sunspots are the major constituents of active regions. Other activities like pores, sunspots with partially

developed penumbra can also be part of the active region. Pores are dark regions which are relatively smaller compared to sunspots without the penumbra. In rare cases, isolated sunspots are observed which are also called in general as active regions. Also, it has been fairly well established that the magnetic field is distributed all over the surface of the Sun but, on much smaller scales than the sunspots. The faculae, network, G-band bright points form part of such small scale structures. In this thesis we concentrate only on the magnetic phenomenon confined to active regions, particularly sunspots.

As noted above, a sunspot can be broadly divided into two regions viz., umbra and penumbra. But, the high spatial resolution observations have revealed that these regions themselves are highly structured and exhibit very complicated magnetic field configuration at all heights in the solar atmosphere. For example, umbral dots-relatively bright and tiny dots in the umbral region and light bridges-relatively bright and fairly wide lanes dividing the umbra into two parts, are some of the fine structures of the umbra which exhibit reduced magnetic field strength. The origin or formation of these fine structures is a topic of hot debate in current solar physics research (see a recent review by [Scharmer et al., 2007]).

Sunspots are called so only if the umbra is surrounded by the penumbra, otherwise it is called as pore. Penumbra possess bright and dark filamentary structures with varied magnetic field strengths and inclinations. Even though, high resolution observations have started to reveal more and more finer structures of penumbra,

the question of penumbral formation is yet to find a satisfactory answer. One of the most important properties of penumbra is the Evershed flow which has daunted researchers for almost a century since the time of its discovery. Evershed flow was discovered in 1908 by John Evershed using a spectrograph at Kodaikanal [Evershed, 1909]. Evershed flow is predominantly a radial horizontal outflow of plasma from sunspot to the surroundings. Recent high resolution observations have revealed that the flows are confined to dark filaments of penumbra which are locally horizontal and exhibit weaker field strength compared to ambient field [Weiss, 2006]. Also, the Evershed flow is height dependent. In the photosphere, the flow decreases rapidly with the height. Above the temperature minimum the flow reverses. This is known as inverse Evershed effect [St. John, 1913].

There are various mechanisms/models proposed to explain the Evershed flow. One of the mechanisms proposed is the siphon flow mechanism for both the photospheric and chromospheric Evershed flows [Meyer and Schmidt, 1968, Thomas and Montesinos, 1993]. In this mechanism, the driving force of the motion is the gas pressure difference between two foot points of a magnetic loop exhibiting different field strengths. Since the presence of the magnetic field reduces the gas pressure, the plasma is expected to flow from weak field or field free region towards the stronger field region. The observations can be easily explained by the siphon flow model in the chromosphere as the flow is towards the stronger magnetic field region, the sunspot. However, we encounter difficulties for a similar kind of scenario in the photosphere. Following the same reasoning as above, the flow should be directed toward the spot

even at the photosphere, but the opposite is observed. In order to overcome the difficulties, we have to assume that the outer footpoint of the loop ends up in an intense magnetic feature, which however is difficult to verify observationally and appears to contradict the fact that the magnetic field strength in the penumbra drops rapidly outwards [Solanki, 2003].

Another mechanism proposed to explain the Evershed flow is the moving flux tube model [Schlichenmaier et al., 1998a,b]. In this model a part of the thin penumbral flux tube, which ends up lying horizontally at the surface, starts below the surface at the outer magnetopause of the sunspot. It reaches the surface due to buoyancy and carries hot gas along with it. The excess pressure due to the high temperature of the gas at the up-stream footpoint of this tube accelerates the gas outward along the horizontal part of the flux tube. The flow starts as hot gas in the inner penumbra and cools rapidly during its passage toward the outer penumbral boundary. However, this model also faces a similar problem as that of siphon flow model which requires the upflowing footpoint possess weaker field strength than the downflowing footpoint. Also, it was shown by Thomas [2006] that the sea-serpent flow configurations suggested by this model [Schlichenmaier, 2003] are gravitationally unstable.

The discovery of dark cores in the bright penumbral filaments with the help of high resolution observations [Scharmer et al., 2002] prompted another model for penumbra known as gappy penumbral model [Spruit and Scharmer, 2006]. These

dark cores contain the major part of the Evershed flow. According to Spruit and Scharmer [2006], the dark cores are nothing but the nearly field free regions below the visible surface. The darkness of the cores is explained as the result of locally enhanced gas pressure associated with the gaps combined with an overall drop of temperature with height. It has been shown recently by Scharmer et al. [2008] through 3D radiation-magneto-hydrodynamical simulation that the Evershed flow represents the horizontal-flow component of overturning convection in gaps with strongly reduced field strength. This model is still in the preliminary stages of development and yet to explain all the observed properties of penumbra. The filamentary structures produced in this simulation are much shorter than observed length of the filaments [Rimmele and Marino, 2006, Rimmele, 2008]. Simultaneous measurements of velocity and magnetic field with high spatial resolution are required further to verify these models and understand the dynamics that take place in the sunspots.

As noted above, despite a number of unresolved issues, significant progress in understanding the sunspot dynamics has been achieved at the photospheric heights. However, sunspot at the photosphere is just a cross-section of a large scale magnetic structure whose foot points are believed to be anchored at the base of the convection zone and their structures extending upto corona and beyond. At the chromosphere and corona, understanding of the plasma dynamics associated with the magnetic field is yet to achieve the kind of maturity that is achieved at the photosphere. This is because the simultaneous measurements of velocity and magnetic field at these heights are rare.

Many authors in the past have studied the plasma flow in the chromosphere and above. Beckers [1964], Maltby [1975], Georgakilas et al. [2003] have observed in H α filtergrams, that the gas flow in chromosphere is confined to dark channels. Dialetis et al. [1985], Alissandrakis et al. [1988] and Dere et al. [1990] have reported that the flow is almost horizontal in the superpenumbra but becomes increasingly vertical (downflows) towards the umbra. However, Abdussamatov [1971] and Lites [1980] report actually upflows. Lites [1980] have interpreted these upflows as due to the umbral flashes. Choudhary et al. [2002] have also reported upflows near the neutral lines. In some cases both down- and upflows within a sunspot are observed [Kjeldseth-Moe et al., 1988, Brynildsen et al., 1999, 2001]. Recently, Lagg et al. [2007] have reported the downflows up to the speed of 40 kms^{-1} in the vicinity of a growing pore through high resolution observations in He I (λ10830) triplet. Their two magnetic component inversion reveal that these downflows always coexist with a second atmospheric component almost at rest (or slow) within the same resolution element.

There are quite a number of magnetic field measurements that have been carried out in the chromosphere and low corona. However, only in rare cases the magnetic fields are derived by taking into account the radiative transfer effects, which is inevitable at these heights [Socas-Navarro, 2005, Solanki et al., 2003]. See a recent review on this topic by Harvey [2006] and for more comprehensive review by Solanki [2003]. A general conclusion on the magnetic field distribution from these reviews is that the magnetic field is more homogeneous in the upper atmosphere. It can be fol-

lowed over a larger distance in the upper atmosphere and decreases more slowly with distance from the sunspot axis. We mention here about some of the intriguing observations which are more relevant to this thesis. Strong magnetic field concentration in lower corona which is as large as 1800 G has been reported by White et al. [1991]. This strong field region is offset from photospheric umbra. Some more authors have also found evidence for equally strong fields in the upper chromosphere and lower corona (see Solanki [2003] for more details). Recent observations by Balasubramaniam et al. [2004], Hanaoka [2005] in H α have indicated the quicker weakening of line-of-sight (LOS) field strengths in the umbral chromosphere. We will see in chapter 4 that how the magnetic field distribution at the chromosphere is affected by its distribution at the photosphere. Some authors have even reported the reversal of magnetic polarity with respect to its photospheric counterpart above flaring sunspot umbrae [Wang and Shi, 1992, Dara et al., 1993, Li et al., 1994]. It was shown in a simple yet more elegant way by Sanchez Almeida [1997] that a weak core emission can cause reversal in the Stokes-V signal which in turn is responsible for the polarity reversal observed in the magnetograms. Later this was confirmed by Briand and Vecchio [2003] and Balasubramaniam et al. [2004] through spectropolarimetric observations.

Simultaneous measurement of velocity and magnetic field at different heights, namely the photosphere, chromosphere and corona is crucial to understand the onset of solar eruptions. Typically, the active regions which show complex magnetic field distribution give rise to solar eruptions such as flares, coronal mass ejections (CMEs)

(e.g., Aschwanden [2005], Schrijver [2007], Schrijver et al. [2008]). It is believed that these eruptions are produced when the opposite polarity magnetic fields interact and partially energized by the electric current developed during this interaction. When the opposite polarity fields are forced to move towards each other they will be stressed and free energy will be generated. These stressed fields tend to reconfigure themselves to minimum potential configuration during which enormous amount of energy will be released. This process is called magnetic reconnection. But the key mechanism which produces these stressed fields is not understood yet though there are various models proposed [Sturrock, 1989, Sterling and Moore, 2004, Antiochos, 1998, Mackay and van Ballegooijen, 2006]. Verifying these models requires a detailed knowledge about the stratification of velocity and magnetic fields in the solar atmosphere (e.g., Socas-Navarro [2005]).

Apart from the issues mentioned above, the magnetic field measurement is important to address the problems related to chromospheric and coronal heating (see the reviews by Erdélyi [2005], Erdélyi and Ballai [2007]).

As discussed above, simultaneous measurement of velocity and magnetic field at different heights in the solar atmosphere is important to address various issues in the solar physics. Lot more efforts are needed both from observation and theoretical side to understand the magnetic related dynamics in the solar atmosphere. Our aim in this thesis is to study in detail the velocity and magnetic structuring, simultaneously at the photosphere and chromosphere through spectropolarimetric observations.

1.2 Remote Sensing of Solar Magnetic Fields: Zeeman Diagnostic

Zeeman effect is one of the most widely used solar magnetic diagnostics on the Sun since the time of Hale [1908]. The essence of Zeeman effect is the splitting of bound energy levels in the presence of external magnetic field (Figure 1.1). This splitting of energy levels results in number of spectral lines depending on the J (the total angular momentum) value of the energy levels involved in the transitions. The splitted lines are shifted symmetrically about the original wavelength position of a given spectral line. For illustration purpose we have considered a simple case, the normal Zeeman effect to show the splitting of spectral lines in the presence of magnetic field and their polarization properties (Figure 1.1). In this example we have considered a spectral line formed due to transition between the atomic energy levels having total angular momentum values $J = 1$ and $J = 0$. In the absence of magnetic field there is only one spectral line. In the presence of external magnetic field there are three lines. The displacement of the spectral lines is directly proportional to the magnetic field strength, square of the wavelength and the effective Landé-g factor of the atomic transition [Stix, 2004]. In other words, the wavelength separation is given by

$$\Delta\lambda_B = 4.67 \times 10^{-13} g B \lambda^2, \tag{1.1}$$

where, $\Delta\lambda_B$ and λ are expressed in Å and B in G.

The spectral lines displaced on either side of the line are generally known as σ components and the lines (line) which are at the line center are known as π components. Splitting of spectral lines in the solar spectrum around $\lambda 5250$ in a sunspot region is shown in Figure 1.2.

From the measurement of the splitting, one can get the direct estimation of the field strength but not its inclination. However, the polarization information contained in the spectral lines can be used to infer the field inclination. Zeeman effect produces a characteristic polarization in spectral lines depending on the orientation of the field with respect to the LOS. When the field is along the LOS then, only the σ components will be seen and are circularly polarized in opposite sense of rotation with each other. For this reason they are usually termed as $\sigma^{\pm}$. When the field is inclined in perpendicular direction, the radiation emitted will be fully linearly polarized with the π components polarized along the field direction and σ components polarized in the perpendicular direction. For the field inclination in an arbitrary direction, they are elliptically polarized. Hence, the measurement of the polarization in spectral lines gives full information on vector properties of the magnetic field.

1.3 Solar Polarimetry

Measurement of line polarization is an essential step towards remote sensing of the solar magnetic fields. The instrument used for measuring the polarization is known

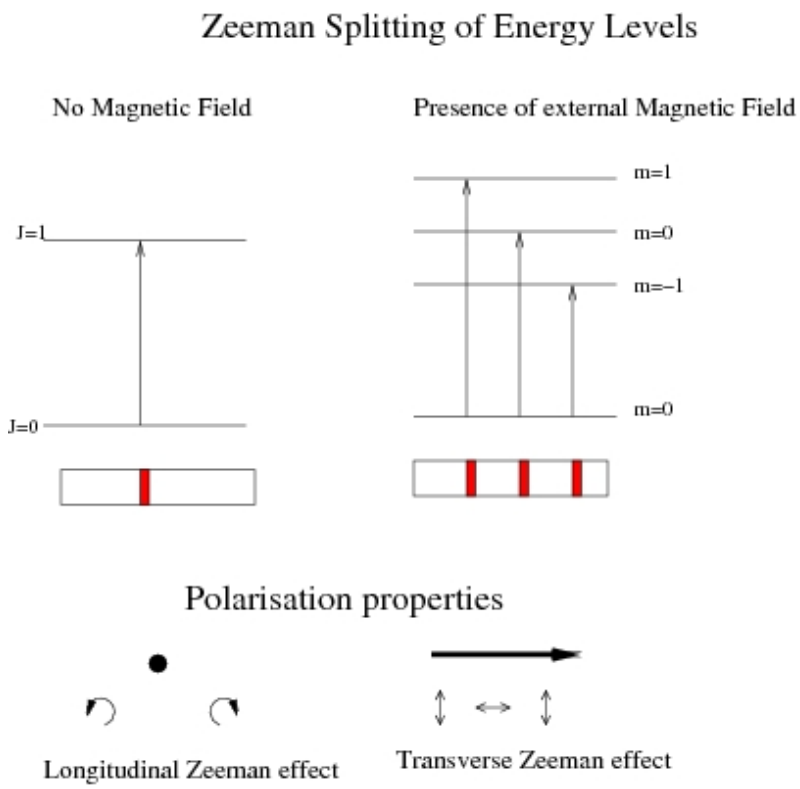

Figure 1.1: Demonstration of the normal Zeeman effect along with the polarization properties of a spectral line when the magnetic field is parallel and perpendicular to the LOS. The dark dot indicates the magnetic field pointing towards the observer (longitudinal Zeeman effect) and the arrow represents the magnetic field perpendicular (transverse Zeeman effect) to the observer. This example is for an absorption line. For an emission line, the sense of rotation for circular polarization will be opposite.

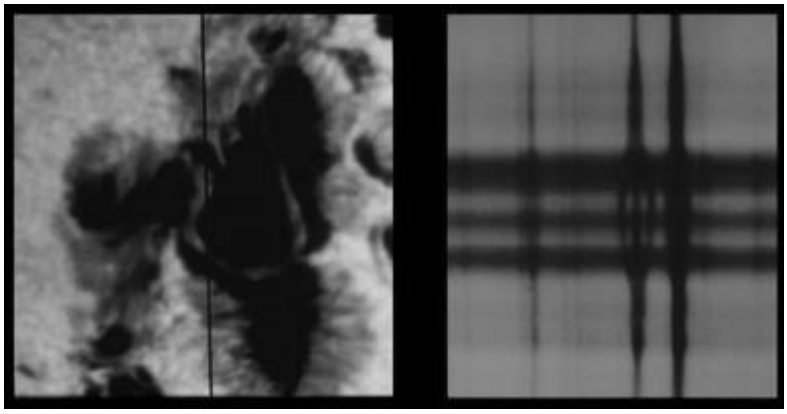

Figure 1.2: Sunspot image with spectrum around 5250 Å correspond to the slit position, seen as dark vertical line on the image, observed on 4th July 1974, at Kitt Peak National Observatory.

as polarimeter. Before going into the details of the polarization measurement, it is important to understand what are the essential measurements required to extract the polarization information, because, the detectors are sensitive to the light but, not to its polarization properties. That means, the polarization information should be imprinted on to the intensity. The general state of partially polarized light is represented through the Stokes parameters [Stokes, 1852, Chandrasekhar, 1960] which are defined in terms of intensities modulated using the appropriate optical devices. Often they are termed as Stokes-I, Q, U and V parameters. Stokes-I represents total intensity, Q and U represent linear polarization and V represent circular polarization (see Chandrasekhar [1960], Rees [1987] for details). To get more insight into the practical definition of Stokes parameters in terms of measurable quantities, we reproduce here the definitions given in Rees [1987], without going into the details of formal mathematical definitions which can be found in Chandrasekhar [1960] as well as in Rees [1987].

Imagine six intensity measurements with the following polarizer angle (θ) settings with and without a retarder of retardance ϵ:

$$\begin{aligned} \epsilon &= 0 \ \text{(no retarder)} \\ \theta &= 0, \frac{\pi}{4}, \frac{\pi}{2}, \frac{3\pi}{4} \end{aligned}$$

so the device transmits only linearly polarized light at these respective orientations; and

$$\begin{aligned} \epsilon &= \frac{\pi}{2} \\ \theta &= \frac{\pi}{4}, \frac{3\pi}{4} \end{aligned}$$

so the device transmits respectively right and left circularly polarized light. The corresponding intensities are represented as I_1, I_2, I_3, I_4, I_5, and I_6.

$$\begin{aligned} I_1 &= I_{trans}(0,0) \\ I_2 &= I_{trans}(\pi/2,0) \\ I_3 &= I_{trans}(\pi/4,0) \\ I_4 &= I_{trans}(3\pi/4,0) \\ I_5 &= I_{trans}(\pi/4,\pi/2) \\ I_6 &= I_{trans}(3\pi/4,\pi/2) \end{aligned} \tag{1.2}$$

Then the Stokes parameters are defined as,

$$\begin{aligned} I &= I_1 + I_2 \\ Q &= I_1 - I_2 \\ U &= I_3 - I_4 \\ V &= I_5 - I_6 \end{aligned} \tag{1.3}$$

In other words, Stokes-Q is the difference in intensities measured with the polarizer along and perpendicular to a chosen reference, Stokes-U is the difference in intensities measured with the polarizer at 45^o and 135^o and Stokes-V is the difference in intensities corresponding to right and left circular polarization. Stokes-I can be a summation of either I_1 and I_2, or I_3 and I_4 or I_5 and I_6.

As it is clear from equation 1.3 that each Stokes parameter is defined in terms of difference in intensities measured at different times or by different detectors at the same time by suitably modulating the input light. Forming the difference of intensity measurements obtained at different times may introduce spurious polarization because of the change in intensity due to various reasons (for eg. variation in the intensity of source itself, or intensity fluctuation due to varying sky transparency and etc). In astronomical observations, the fluctuation caused due to atmospheric variation is one of the major contributor to the spurious polarization. However, these effects could be reduced using a fast modulation scheme. In other words, measuring the intensities at the faster rate (> 1 kHz) the atmospheric induced effects could be

minimized [Stenflo and Povel, 1985, Lites, 1987]. In the limit where the modulation of the polarization is much more rapid than the seeing fluctuations (i.e. for frequencies > 1kHz), seeing induced cross-talk is not of concern. Faster modulation has been realized through Zurich IMaging POLarimeter (ZIMPOL; Povel et al. [1991], Stenflo et al. [1992]). Through this it has been possible to achieve the precision in polarization measurement close to $10^{-5} \times I_c$, where I_c is the continuum intensity, along with the polarization free telescope THEMIS [Arnaud et al., 1998]. One of the main limitations of this kind of schemes is the requirement of a specially designed CCDs. Slightly slower modulation scheme was suggested by Lites [1987] based on rotating waveplate on the order of few hundred Hz. This option is used, for instance, by ASP (Elmore et al. [1992], POLIS (Beck et al. [2005]), and SPINOR (Socas-Navarro et al. [2006]). These polarimeters are dual-beam systems about which more details are discussed in the following section.

In dual-beam polarimetry, the spurious polarization introduced by the intensity fluctuations is reduced by recording simultaneously the orthogonally polarized beams. For e.g., practically no spurious Q is introduced if the intensities I_1 and I_2 of Eq. 1.3 are recorded simultaneously. This can be achieved using a polarizing beam splitter which produces two orthogonal linearly polarized beams. It was shown by Lites [1987] that in dual-beam system, the seeing induced cross-talks among Stokes parameters are factors of 3-5 smaller than in single beam system. Also, in ideal condition there is no loss of photons, because both orthogonal polarized beams are recorded. However, in dual beam polarimetry two beams need to be recorded onto

two different detectors or different pixels of the same detector. If the detectors/pixels responses are not uniform then spurious polarization will be introduced because of the so called gain table errors. This has been overcome by using a beam-swapping technique [Donati et al., 1990, Semel et al., 1993, Bianda et al., 1998].

Significant progress has been achieved in understanding of magnetic dynamics on the Sun in the past two decades from the success of the ground based observations with the help of polarimeters such as Advanced Stokes Polarimeter (ASP; Elmore et al. [1992]), Zurich IMaging POLarimeter (ZIMPOL; Stenflo et al. [1992]), La Palma Stokes Polarimeter (LPSP; Mártinez Pillet et al. [1999]), Diffraction Limited Stokes Polarimeter (DLSP; Sankarasubramanian et al. [2004]), in the visible wavelengths and Tenerife Infrared Polarimeter (TIP; Mártinez Pillet et al. [1999]), in near-infra-red (NIR) wavelengths. Also, space based magnetometry such as Michelson Doppler Imager (MDI) on board SOlar and Heliospheric Observatory (*SOHO*/MDI; Scherrer et al. [1995]) for LOS magnetic field measurements, spectropolarimeter as part of Solar Optical Telescope onboard *Hinode* (*Hinode*/SOT; Kosugi et al. [2007], Lites et al. [2007]).

It would be of interest to note here that the first measurements of the magnetic field at Kodaikanal was due to Bhattacharyya [1969], who built a longitudinal magnetograph to map the general magnetic field of the Sun. His technique was similar to that of Babcock's, in using an electro-optic modulator (ADP crystal) to alternately chop the right and left circular polarized components of the Zeeman broadened lines.

At the exit of the spectrograph the wings of the spectral line Fe I λ5250.22 as well as the line center were isolated to simultaneously measure the magnetic and velocity fields.

The first spectropolarimeter at Kodaikanal was built by Balasubramaniam [1988]. A quarter waveplate (QWP) followed by a polaroid were used as polarization analyzer. The QWP and the polaroid can independently be turned by a mechanical wheel arrangement about the direction of the incoming beam. The system was hooked on to the slit assembly during the polarimetric observations. The Stokes profiles used to be recorded in six successive combinations with a 35 mm camera at the exit of the spectrograph. Later on Sankarasubramanian [2000] has developed a polarimeter which uses the same principle but with film camera replaced by a CCD camera and the rotation of the polaroid was automatized through a stepper motor. Both these polarimeters are so called single beam polarimeters. As it was discussed, in single beam polarimeters efficiency is less and the polarisation accuracy is vulnerable to fluctuations in the input intensity mostly produced by the Earth's atmospheric turbulence. For this purpose, a dual beam polarimeter has been fabricated and installed at Kodaikanal for spectropolarimetric observations [Nagaraju et al., 2007, 2008b].

1.4 Radiative Transfer

The energy generated in the core of the Sun through nuclear fusion is transported to surface and get radiated away in various forms. From core to about $0.7R_{\odot}$ ($R_{\odot}$-the radius of the Sun), the energy is transported through radiative means and from $0.7R_{\odot}$ to the surface of the Sun, it is through convective means. In the solar atmosphere, the energy transport is through radiative transfer. The very fact that the existence of the temperature gradient in the solar atmosphere is the cause of spectral line formation through radiative transfer suggest that they sample a range of heights in the solar atmosphere. Hence the detailed analysis of these lines will result in a wealth of information on the physical conditions in the solar atmosphere. To derive meaningful physical parameters from the spectral lines, it is important to take into account the radiative transfer effects.

Pioneering work in formulating polarized radiative transfer equation (RTE) was by Chandrasekhar [1960] and later Unno [1956] formulated the polarized radiative transfer in a magnetic medium including the Zeeman effect. In this case the magneto optical effects were neglected and the equations were formulated in a restricted geometry. More general treatment was given by Rachkovsky [1962] including the magneto-optical effects. Quantum mechanical treatment of radiative transfer was by Degl'Innocenti and Degl'Innocenti [1972]. Later on Jefferies et al. [1989] have revised the whole formulation of the radiative transfer equation (RTE) by clarifying the confusions regarding the sign conventions. Their formulation was based on classi-

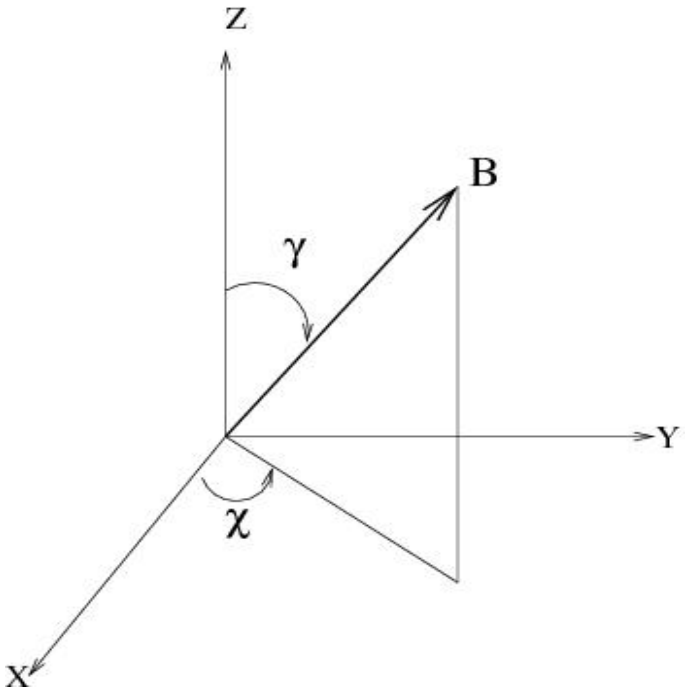

Figure 1.3: A diagram showing the LOS coordinate system in which the magnetic field, **B** is inclined at an angle γ with respect to Z-axis. The LOS is along the Z-axis. The azimuth of the field is represented by χ in this coordinate system.

cal theory of electrodynamics. They also discuss the similarity between the classical and quantum theories.

Polarized radiative transfer equation can be written in a LOS coordinate system (Figure 1.3) with Z-axis along the LOS (see for eg., Jefferies et al. [1989]) as,

$$\frac{d\mathbf{I}}{dz} = -\mathbf{K}(\mathbf{I} - \mathbf{S}) \tag{1.4}$$

where $\mathbf{I} = (I, Q, U, V)^T$ is the Stokes vector with T representing the transpose, $\mathbf{K}$ is the absorption matrix and $\mathbf{S}$ is the source function.

Often in the photosphere, the atmosphere is considered to be in local-thermodynamic-equilibrium (LTE) and also plane parallel. Thus the source function in equation 1.4 is assumed to be Planckian. Further to solve RTE, usually it is assumed as a linear function of height. On the other hand, the structure of absorption matrix is more complicated through which one has to derive the connection between the Stokes parameters and the atmospheric parameters.

$$\mathbf{K} = \begin{pmatrix} \kappa_I + \kappa_c & \kappa_Q & \kappa_U & \kappa_V \\ \kappa_Q & \kappa_I + \kappa_c & \kappa'_V & -\kappa'_U \\ \kappa_U & -\kappa'_V & \kappa_I + \kappa_c & \kappa'_Q \\ \kappa_V & \kappa'_U & -\kappa'_Q & \kappa_I + \kappa_c \end{pmatrix}.$$

where κ_c is continuum opacity. The line opacities are defined through

$$\begin{aligned} \kappa_I &= \frac{1}{2}\left[\left(\frac{\kappa_r + \kappa_l}{2}\right)(1 + \cos^2\gamma) + \kappa_p \sin^2\gamma\right], \\ \kappa_Q &= \frac{1}{2}\left(\kappa_p - \frac{\kappa_r + \kappa_l}{2}\right)\sin^2\gamma\cos2\chi, \\ \kappa_U &= \frac{1}{2}\left(\kappa_p - \frac{\kappa_r + \kappa_l}{2}\right)\sin^2\gamma\sin2\chi, \\ \kappa_V &= \left(\frac{\kappa_r - \kappa_l}{2}\right)\cos\gamma, \\ \kappa'_Q &= \frac{1}{2}\left(\kappa'_p - \frac{\kappa'_r + \kappa'_l}{2}\right)\sin^2\gamma\cos2\chi, \\ \kappa'_U &= \frac{1}{2}\left(\kappa'_p - \frac{\kappa'_r + \kappa'_l}{2}\right)\sin^2\gamma\sin2\chi, \\ \kappa'_V &= \left(\frac{\kappa'_r - \kappa'_l}{2}\right)\cos\gamma. \end{aligned} \tag{1.5}$$

The absorption and magneto-optic coefficients κ and κ' are given by

$$\begin{aligned} \kappa(v) &= \kappa_0 H(a,v) \\ \kappa(v)' &= \kappa_0 2F(a,v), \end{aligned} \tag{1.6}$$

where

$$\begin{aligned} H(a,v) &= \frac{1}{\pi}\int_{-\infty}^{+\infty} \frac{e^{-y^2}dy}{(v-y)^2+a^2} \\ F(a,v) &= \frac{1}{2\pi}\int_{-\infty}^{+\infty} \frac{(v-y)e^{-y^2}dy}{(v-y)^2+a^2}. \end{aligned} \tag{1.7}$$

with κ_p, κ'_p are evaluated with $v = (\nu - \nu_0)/\Delta\nu_D$ and κ_{lr}, κ'_{lr} evaluated with $v = (\nu \mp \nu_L - \nu_0)/\Delta\nu_D = v \mp v_b$, with $v_b = \nu_L/\Delta\nu_D$. The Larmor frequency is given by $\nu_L = eB/4\pi mc$ with e-the electron charge, m-the electron mass, c-the speed of light and B-the magnetic field strength. The quantities ν_0 and ν represent the frequency points of line center and frequency points within the line, $\Delta\nu_D$ represent the Doppler width and a represent the damping parameter of the atomic transition. The magnetic field information is incorporated in RTE through absorption matrix elements (see Eq. 1.6). In the equation 1.6 the symbols γ and χ represent the field inclination and azimuth of the magnetic field, respectively, in the LOS co-ordinate system (see Figure 1.3).

One can easily notice that the Stokes profiles depend on the atmospheric param-

eters in a highly non-linear form through absorption matrix and the source function vector. To disentangle these effects, least-squares inversion techniques based on analytical or numerical solutions of the RTE are needed which will be discussed in section 1.5. In the following section we will see under certain assumptions how to connect the polarization information to the magnetic field parameters in a simpler way.

1.4.1 Weak Field Approximation

If the splitting of spectral lines due to Zeeman effect is smaller compared to its Doppler broadening ($v_b < 1$) then $H(a, v \pm v_b)$ can be written in terms of a Taylor series as

$$H(a, v \pm v_b) \approx H(a, v) \pm v_b H'(a, v) + \frac{v_b^2}{2} H''(a, v) + ... \tag{1.8}$$

By neglecting the higher order terms the RTE simplifies in such a way that the Stokes parameters are disentangled and following relations can be derived [Jefferies et al., 1989, Jefferies and Mickey, 1991].

$$V(v) = v_b cos\gamma \frac{\partial I}{\partial v} \tag{1.9}$$

$$Q(v) = -\left(\frac{v_b \sin\gamma}{2}\right)^2 \frac{H''(a, v)}{H'(a, v)} \frac{\partial I}{\partial v} \cos 2\chi \tag{1.10}$$

$$U(v) = -\left(\frac{v_b \sin\gamma}{2}\right)^2 \frac{H''(a, v)}{H'(a, v)} \frac{\partial I}{\partial v} \sin 2\chi \tag{1.11}$$

1.5 Inversion Techniques

The information on the properties of solar magnetic atmosphere is contained in the observed Stokes profiles emerged from it. Extracting this information is not easy, because the observed profiles depend on the atmospheric parameters in a highly non-linear manner through the absorption matrix and the source function vector (Eq. 1.4). Least-squares inversion techniques (ITs) based on analytical or numerical solutions of the radiative transfer equation have been the most reliable means of converting polarization spectral information into meaningful atmospheric parameters (see reviews on this topic by Del Toro Iniesta and Ruiz Cobo [1996], Socas-Navarro [2001] and Bellot Rubio [2006]). These methods compare the observed Stokes profiles with synthetic profiles emerging from an initial guess model atmosphere. The misfit is used to modify the atmospheric parameters until the synthetic profiles match the observed ones. This procedure yields a model atmosphere capable of explaining the measurements, within the assumptions and limitations of the model.

Pioneering work on the development of ITs is by Harvey et al. [1972] and Auer et al. [1977] usually known in the literature as Unno-fitting technique. They have used Marquardt method to solve the inversion problem. Their method was based on Unno's solution of the RTE which neglected the magneto-optical (MO) effects. They have assumed Milne-Eddington model atmosphere in which magnetic field vector and the velocity along LOS are constant with depth. This technique was later on generalized by Landolfi et al. [1984] to include MO effects. Further, Skumanich and

Lites [1987] improvised this method by including a free parameter for the influence of scattered light, and/or the unresolved character of observations. Fraction of this parameter is considered as magnetic fill factor. The technique was later extended to account for some NLTE effects by Lites et al. [1988].

Despite the results presented in this thesis are based on the IT which assumes Milne-Eddington atmosphere, for the sake of completeness we mention here about the other ITs which are most commonly in use. The IT proposed by Landi Degl'Innocenti and Landolfi [1982], Landolfi [1987], Ruiz Cobo and del Toro Iniesta [1992] are based on so called response functions, and hence the acronym SIR (Stokes Inversion based on Response functions), which takes into account the gradients in the physical parameters such as velocity, magnetic field and etc. This technique was generalized to include non-LTE effects by Socas-Navarro et al. [1998, 2000].

Sanchez Almeida [1997] has developed an IT to recover the microstructured magnetic atmospheres (MISMA) by fitting Stokes profiles. These model atmospheres incorporate small-scale (on the scales smaller than the mean free path of the photons) fluctuations of the magnetic field vector, the velocity, the temperature and etc.

1.6 Motivation for the Thesis

It was seen in the beginning of this chapter that most of the issues in solar physics require the accurate measurement of velocity and magnetic fields. Spectropolarimetry is one of the most powerful techniques to accurately measure them. High dispersion and high resolution spectrograph installed at KTT [Bappu, 1967], can be used to its full potential by adding a polarimeter to this spectrograph. In the past, the polarimeters were built and used at KTT by Balasubramaniam [1988] and Sankarasubramanian [2000]. However, the accuracy of these polarimeters was limited because they are single beam systems. Towards the aim of achieving better efficiency and accuracy in the measurement of the polarization, a dual beam polarimeter has been fabricated and installed at KTT. Chapters 2 and 3 of this thesis describe the polarimeter setup and its characterization.

Measurement of the magnetic field at the photosphere is relatively well established. Achieving the same in the chromosphere and corona is very rare [Solanki et al., 2003, Socas-Navarro, 2005, Lagg, 2007]. The reasons for this are: (i) there are very few spectral lines available for chromospheric studies in the visible wavelength region-the spectral range in which the instrumentation is relatively easy (easy availability of the polarization optics, CCD detectors and etc.), (ii) converting the polarization information in the spectral lines to meaningful physical parameters is not well established, (iii) the solar atmosphere is not in thermodynamic equilibrium which can be assumed locally at the photosphere. In this regard, simultaneous mea-

surement of the magnetic field at the photosphere and chromosphere will help in understanding the measurements at the chromosphere. Once the reliability of field measurement in the chromosphere is established then this will be an important input to understand the dynamics that take place in the higher layers of the solar atmosphere. The effort in this thesis is to establish the reliability of the magnetic field measurement in the chromosphere through H α spectropolarimetry in conjunction with the simultaneous measurement of the photospheric magnetic field.

Chapter 2

An Efficient Modulation Scheme for Dual-Beam Polarimetry

2.1 Introduction

In classical electromagnetic theory, the properties of light may be described in terms of the electric wave vector (**E**) in the plane perpendicular to the direction of propagation (e.g., Born and Wolf [1999]). Detectors are sensitive only to the intensity, which is the square of amplitude of **E**, but not to its amplitude or phase, which together define the state of polarization viz. linear, circular or in general elliptical. Hence all the polarimetric techniques are based on the basic principle of introducing the

information of polarization (through altering amplitude and/or phase of **E**) into the intensity of the transmitted light. This is called polarization modulation or simply the modulation. A simple polarimeter consists of a number of retarders or waveplates (usually, one or two) followed by a linear analyzer (nothing but a linear polarizer). The retarders modify the polarization state of the incoming light in an adequate way such that the analyzer only transmits, at the end, the desired component of the electric field. A number of measurements varying the retarders (either their retardance or their orientation) makes it possible to obtain a set of intensities from which one can retrieve efficiently the polarization state of the input light. This process is called modulation scheme. Most commonly, the number of measurements obtained are sequential. In this case, the orientation of the analyzer is fixed. In some cases, linear polarization measurements are done through sequential measurements by orienting the analyzer at appropriate angles. Further, to measure the circular component of the light a retarder with an appropriate retardance is used in combination with the analyzer (see Eq. 1.3). The later polarimeters are not preferred because of the complications such as optical aberrations and polarization dependent fringes introduced due to the use of different optics for different measurements. Most of the polarimeters used in solar observations perform with fixed orientation of the analyzer. One such polarimeter has been built and installed at KTT for spectroplarimetric observations on the Sun as part of this thesis work. The developed polarimeter consists of a zero-order quarter wave (R1), a zero-order half wave (R2) retarder at λ6300 and Polarizing Beam Displacer (PBD) as analyzer. The retarders R1 and R2 are the first and second elements of the polarimeter, as seen by the incoming light, followed

by the PBD. The PBD has an extinction ratio $< 10^{-3}$ with respect to a polarizing Glan-Thomson prism (GTP) in the wavelength range $\lambda 4000 - 7000$.

Polarimetric accuracy is one of the most important goals in modern astronomy. It is limited since most optical elements encountered by the light on its path from the source to the detector, can alter its state of polarization (for eg. telescope optics, imaging system, grating, etc). Apart from these, variation in sky transparency, image motion and blurring due to the atmosphere are a major concern in high precision ground based solar polarimetry. The effect of atmosphere, which is commonly known as seeing induced effect, can be reduced by fast modulation schemes [Stenflo and Povel, 1985]. The modulation frequencies in these schemes are generally higher than seeing fluctuations, which is $\approx$ 1 kHz [Stenflo and Povel, 1985, Lites, 1987]. Large format CCDs, which are required to cover reasonable spectral and spatial range, will pose difficulty in reading out the data at kHz speed. Stenflo and Povel [1985] demonstrated a scheme whereby rapidly modulated signal is demodulated by optical means, thereby avoiding the need to read the detectors at a rapid rate. Lites [1987] proposed a rotating waveplate modulation scheme as an alternative to minimize the seeing induced cross-talk among Stokes parameters. He has shown that faster the rotation rate of the modulator, lower the cross-talk among Stokes parameters. Seeing induced cross-talk levels of a dual beam system are factors 3-5 smaller than that of a single beam system. However, in dual beam system, the error introduced due to flat field residual is a matter of concern in high precision polarimetry. A plausible solution to the above mentioned problem can be found

by using a mixed scheme in which spatial and temporal modulations are performed (Elmore et al. [1992], Mártinez Pillet et al. [1999], Sankarasubramanian et al. [2004]). The gain table uncertainties are avoided using the beam swapping technique (Donati et al. [1990], Semel et al. [1993], Bianda et al. [1998]). Beam swapping is nothing but the interchange of orthogonal states of polarization by introducing appropriate retardance to input light at a suitable orientation of the retarders.

With the available optical components, a simple and effective way of measuring Stokes parameters is to use a half waveplate (HWP) along with PBD for linear polarization measurements and a quarter waveplate (QWP) along with PBD for circular polarization measurements as explained in Bianda et al. [1998]. This modulation scheme is based on the beam swapping technique suggested by Donati et al. [1990]. However, this way of modulation will introduce a possible differential optical aberrations between the linear and circular polarization measurements due to different optical elements encountered by the light. Using both the waveplates during all stages of measurements or using a single retarder with an appropriate retardance can avoid the differential aberrations [Lites, 1987, Elmore et al., 1992]. A modulation scheme which uses both R1 and R2 in all stages of measurements is worked out in this thesis towards the goal of achieving a better efficiency and accuracy in the polarization measurements.

2.2 Modulation

As explained in chapter 1, a single measurement is not sufficient to determine all four Stokes parameters of the incoming radiation (see Eq. 1.3). Depending on the setup, a number of measurements obtained by varying the orientation of retarders are required to determine them with the best possible efficiency and accuracy. Since at a given wavelength the retardance of the retarders is fixed, different modulations of the incoming radiation is possible only through orienting the retarders at different angles. To avoid seeing induced cross-talks among Stokes parameters Polarizing-Beam-Displacer (PBD) is used as a polarization analyzer. This implies the recording of the orthogonally polarized beams on to two different detectors or different pixels of a large detector. Gain table uncertainties will be introduced while combining the two beams. Beam swapping is a powerful technique to minimize flat field induced errors [Donati et al., 1990, Semel et al., 1993, Bianda et al., 1998]. Another important point one should be concerned is about the slow measurements. There are various reasons for slow measurement such as slower readout of CCD, slower rotation of the waveplates and etc. This means, to obtain one set of Stokes parameters the time taken are invariably longer compared to the seeing induced fluctuations and hence requires a well balanced modulation scheme. Balanced modulation scheme means the modulated intensities should be a function of all the input Stokes parameters with equal efficiency for all of them. A modulation scheme which incorporates all these features is worked out and is discussed below.

The input polarization is modulated on to intensity by using the waveplate orientations given in Table. 2.1.

Modulation stage	Orientation of QWP(R1)	Orientation of HWP(R2)
1	22.5	0
2	22.5	45
3	67.5	45
4	67.5	90
5	112.5	90
6	112.5	135
7	157.5	135
8	157.5	180

Table 2.1: Orientation of Waveplates, expressed in degrees, for different stages of modulation.

The modulated intensities $\mathbf{I}^{\pm} = (I_1^{\pm}, I_2^{\pm}, I_3^{\pm}, I_4^{\pm}, I_5^{\pm}, I_6^{\pm}, I_7^{\pm}, I_8^{\pm})^T$, where T represents transpose operator, can be written in terms of input Stokes parameters as

$$\mathbf{I}^{\pm} = g^{\pm}\mathbf{O}^{\pm}\mathbf{S}_{in}, \tag{2.1}$$

where $\pm$ indicate two orthogonally polarized beams emerging out of the polarimeter. $\mathbf{S}_{in} = [I, Q, U, V]^T$ is the input Stokes vector to the polarimeter. The matrices $\mathbf{O}^{\pm}$ are known as modulation matrices. The multiplication factor of the two orthogonally polarized beams $g^{\pm}$, known as the gain factor, is a product of transparency of the corresponding optical path and the detector gain factor. The polarimeter Mueller matrices of respective beams can be obtained by multiplying the Mueller matrices of retarders ($\mathbf{M}_{R1}$ and $\mathbf{M}_{R2}$) and PBD ($\mathbf{M}_P^{\pm}$) in the order $\mathbf{M}_P^{\pm}\mathbf{M}_{R2}\mathbf{M}_{R1}$ [1] (Stenflo

[1]See appendix A for details on the Mueller matrices

[1994], del Toro Iniesta [2003]). The modulation matrices $\mathbf{O}^{\pm}$ are constructed by arranging the first row of the analyzer matrix of the respective beam for each of the measurement steps (see del Toro Iniesta [2003]).

The theoretical modulation matrices $\mathbf{O}^{\pm}$ at the design wavelength are given by,

$$\mathbf{O}^{\pm} = 0.5 \begin{pmatrix} 1.0 & \pm 0.5 & \mp 0.5 & \pm 0.707 \\ 1.0 & \mp 0.5 & \pm 0.5 & \mp 0.707 \\ 1.0 & \mp 0.5 & \mp 0.5 & \mp 0.707 \\ 1.0 & \pm 0.5 & \pm 0.5 & \pm 0.707 \\ 1.0 & \pm 0.5 & \mp 0.5 & \mp 0.707 \\ 1.0 & \mp 0.5 & \pm 0.5 & \pm 0.707 \\ 1.0 & \mp 0.5 & \mp 0.5 & \pm 0.707 \\ 1.0 & \pm 0.5 & \pm 0.5 & \mp 0.707 \end{pmatrix}.$$

It is to be noted here that the four Stokes parameters are modulated on to intensity in all the eight stages of measurements. Also, each Stokes parameter is weighted equally in all the eight stages of measurements. Matrices $\mathbf{O}^{\pm}$ show that the alternate measurements are obtained by swapping the orthogonally polarized beams (seen as sign change in the corresponding Stokes parameters).

According to del Toro Iniesta and Collados [2000], an optimum modulation matrix

($\mathbf{O}$) should satisfy the condition that the efficiency matrix defined through

$$\mathbf{A} = \mathbf{O}^T\mathbf{O}, \tag{2.2}$$

should be diagonal. The efficiency matrices ($\mathbf{A}$) corresponding to $\mathbf{O}^{\pm}$ in Eq. 2.1 are indeed diagonal. The maximum efficiencies of the modulation scheme in measuring Stokes-I, Q, U, V are 1.0, 0.5, 0.5, 0.707, respectively, at the design wavelength. The total polarimetric efficiency is $\sqrt{0.5^2 + 0.5^2 + 0.707^2} = 0.9999$, which is close to unity as expected since the absolute values of all the elements in a given column are same (del Toro Iniesta and Collados [2000], del Toro Iniesta [2003]). The values of matrix elements $\mathbf{O}^{\pm}$ are not the same at different wavelengths because of the chromatic nature of the waveplates used in the polarimeter and hence the maximum efficiencies of modulation scheme in measuring Stokes-Q, U, V are different (Figure 2.2). However, the total polarimetric efficiency will remain close to unity at least in visible wavelength range.

For comparison, the maximum efficiencies of some of the well known polarimeters are given below: ASP-(1.0, 0.546, 0.41, 0.659), ZIMPOL-(1.0, 0.474, 0.467, 0.534), TIP-(1.0, 0.617, 0.41, 0.659), POLIS-(1.0, 0.494, 0.464, 0.496) at their respective design wavelengths. In the above examples, only TIP has a total polarimetric efficiency close to unity.

2.3 Demodulation

It is discussed in the previous section about an efficient way of modulating the input light such that the modulated intensities are functions of all the input Stokes parameters with a good efficiency. It is also important to retrieve the Stokes parameters from the modulated intensities in an equally effective way. The process of retrieving the Stokes parameters from the modulated intensities is called as demodulation. The demodulation of the input Stokes parameters from the modulated intensities presented here involve the following steps. As a first step, the signal vectors ($\mathbf{S}^{\pm}$) of the orthogonally polarized beams are constructed from the modulated intensities (Eq. 2.1) using the equation,

$$\mathbf{S}^{\pm} = \mathbf{D}\mathbf{I}^{\pm}/8. \tag{2.3}$$

Where the matrix $\mathbf{D}$ is defined as,

$$\mathbf{D} = \begin{pmatrix} 1.0 & 1.0 & 1.0 & 1.0 & 1.0 & 1.0 & 1.0 & 1.0 \\ 1.0 & -1.0 & -1.0 & 1.0 & 1.0 & -1.0 & -1.0 & 1.0 \\ -1.0 & 1.0 & -1.0 & 1.0 & -1.0 & 1.0 & -1.0 & 1.0 \\ 1.0 & -1.0 & -1.0 & 1.0 & -1.0 & 1.0 & 1.0 & -1.0 \end{pmatrix}.$$

One can see from the matrix $\mathbf{D}$ that, to derive signal vectors, all the eight stage intensity measurements are considered with equal weights. Hence the derived input Stokes parameters will be well balanced with respect to changes, if there are any, during the measurements. The derived Stokes parameters will be an average over

the time taken for the eight stages of modulation.

The second step involves combining the signal vectors of the orthogonally polarized beams after correcting for the gain factors $g^{\pm}$. Combining the two orthogonally polarized beams is essential to reduce the seeing induced spurious polarization. Gain table corrections can be done either by regular flat field procedure or normalizing the elements of signal vectors to their respective first element (i.e. $\mathbf{S}^{\pm}/S^{\pm}(0)$). Since the regular flat field procedure limits the polarimetric precision and to make use of the advantage of the beam swapping technique incorporated in the modulation scheme, second method is used to derive the combined signal vector. The components of the signal vector ($\mathbf{S}'$) of the combined beam can be written as

$$\begin{aligned} S'(1) &= S^{+}(1) + S^{-}(1) \\ S'(2) &= S^{+}(2)/S^{+}(1) - S^{-}(2)/S^{-}(1) \\ S'(3) &= S^{+}(3)/S^{+}(1) - S^{-}(3)/S^{-}(1) \\ S'(4) &= S^{+}(4)/S^{+}(1) - S^{-}(4)/S^{-}(1) \end{aligned} \tag{2.4}$$

where $S'(i)$, $i = 1, 2, 3, 4$, are the elements of $\mathbf{S}'$. The indices $i = 1, 2, 3, 4$ correspond to the Stokes parameters I, Q, U and V, respectively.

However, the flat field corrections are essential for the total intensity about which more details are given in chapter 3. With the definitions of Eq. (2.4), the signal vector of the combined beam can be written in terms of the input Stokes vector as (Stenflo [1984], Gandorfer [1999]),

$$\mathbf{S}' = \mathbf{M}\mathbf{S}'_{in}. \tag{2.5}$$

Where $\mathbf{S}'_{in} = [I, Q/I, U/I, V/I]^T$ is the input Stokes vector and $\mathbf{M}$ is a 4×4 matrix known as the response matrix of the polarimeter. The theoretical response matrix at the design wavelength is given by

$$\mathbf{M} = \begin{pmatrix} 1 & 0 & 0 & 0 \\ 0 & 0.5 & 0 & 0 \\ 0 & 0 & 0.5 & 0 \\ 0 & 0 & 0 & 0.707 \end{pmatrix}.$$

The third and final step involves obtaining the input Stokes vector ($\mathbf{S}'_{in}$) from Eq.(2.5).

2.3.1 Polarimetric Efficiency

The efficiency of the polarimeter in measuring respective Stokes parameter is defined as (Beck et al. [2005])

$$\epsilon_i = \sqrt{\sum_{j=1,4} \mathbf{M}_{ji}^2}. \tag{2.6}$$

where i = 1, 2, 3, 4 corresponds to Stokes - I, Q, U, V respectively. Since the response matrix $\mathbf{M}$ in Eq.(2.5) is diagonal, the efficiency in the Eq. (2.6) will be simplified (using Eq. 2.5) to

$$\epsilon_i = |S'(i)/S'_{in}(i)|. \tag{2.7}$$

We would like to note here that the response matrix $\mathbf{M}$ in Eq.(2.5) is diagonal at all the wavelengths considered here. However, at the wavelengths away from the design wavelength, the signals $S^{\pm}(0)$ in Eq. (2.3) are not just proportional to input Stokes-I but with a small contribution from the input Stokes-Q. If the signal vectors ($\mathbf{S}^{\pm}$) of orthogonally polarized beams are combined without normalizing to their respective Stokes-I signal then this cross-talk term will not appear in the signal vector ($\mathbf{S}'$) of the combined beam. But, the flat fielding is essential to remove the gain factors $g^{\pm}$. In this paper the signal vectors are combined in such a way that the Stokes-Q, U, V signals are normalized to Stokes-I signal in order to remove the gain factors. This results in an over estimation of efficiency ϵ_Q. This over estimation is about 1.8% at λ4500, 0.15% at λ5000, 0.65% at λ5500, 0.24% at λ5890, 0.1% at λ6563 and 0.6% at λ7000. These wavelengths are chosen because, the efficiencies are

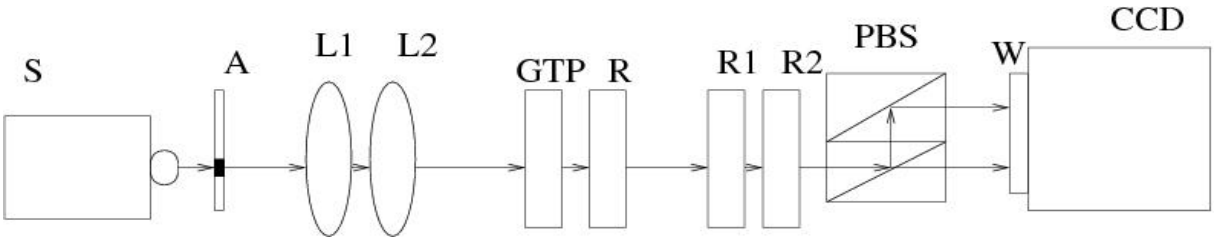

Figure 2.1: Block diagram of an experimental setup used to study the polarimetric efficiency. The symbols in the figure are S-monochromator, A-mount holding a $1mm$ square aperture, L1 and L2-lenses(f=25cm), GTP-Glan Thomson prism used to produce linear polarization, R-QWP used along with GTP to produce circular polarization, R1 and R2- Half and Quarter waveplates which forms a part of the polarimeter, PBD-polarizing beam splitter, W- CCD window.

measured at these wavelengths through an experiment presented in the next section. In regular solar observations the Stokes-Q signal is smaller than Stokes-I at least by an order of magnitude and hence the cross-talk from Q to I will be often negligible.

2.3.2 Laboratory Experiment

The efficiency of the polarimeter is different for different wavelengths due to the chromatic nature of the retarders used in the polarimeter. If the polarimeter is to be used at different wavelengths then it is important to understand its performance at the desired wavelength. The variation of the efficiency factor for different input Stokes parameters is studied by carrying out laboratory experiments.

The experimental setup is shown in Fig.2.1. The light from the monochromator was set at a desired wavelength and then passed through a 1 mm rectangular

aperture. This rectangular aperture was imaged on to a CCD detector using a two lens system with an effective focal length of 12.5 cm. The polarimeter optics were placed between the lens and the detector. The first in the light beam is the QWP (R1), followed by the HWP (R2) and the PBD. The retarders (R1 and R2) of the polarimeter were mounted on two different rotating stages whose rotational accuracy is 0.1^o. A known state of polarization was produced using the GTP and calibration retarder (CU). Stokes Q and U were produced by using only the GTP where as both GTP and CU retarder were used to produce Stokes V. The CU retarder is a zero order chromatic waveplate which acts as a quarter waveplate at $\lambda 6300$. This is the same quarter waveplate which was earlier used in the single beam polarimeter at Kodaikanal by Sankarasubramanian [2000] and the characteristics of the waveplate is presented in his thesis. The retardance of the CU retarder at other wavelengths is calculated by the well known linear relation, $\Delta\phi = k/\lambda$ (see for eg. in Hetch [2002]), where the constant k is evaluated by knowing that $\Delta\phi$ is 90^o at $\lambda = 6300$ Å. Eight measurements, for each input Stokes parameter, were performed by positioning the retarders (R1 and R2) at different angles as given in Table.2.1.

The measured data were first corrected for dark current. Then the Stokes signal vectors corresponding to the orthogonally polarized beams were obtained from the measured intensities and the matrix $\mathbf{D}$ using Eq.(2.3). Stokes-Q, U, V signals were normalized to the respective Stokes-I signal as in Eq.(2.4).

We noted in the section 2.3 that the theoretical response matrix of the polarime-

ter presented in this paper is diagonal at all the wavelengths considered. However, in practice there will be off-diagonal elements which are nothing but the cross-talk among Stokes parameters. But, in the experiment performed to study the polarimetric efficiency, the measured cross-talk terms are small. Since the cross-talk terms are small (<1%), the simplified definition of Eq.(2.7) is used to calculate the efficiency.

Plots of polarimetric efficiency in measuring Stokes Q, U and V as a function of wavelength are shown in Figure 2.2. The diamond symbols shown in the plots are the experimental values and the solid lines are theoretical curves. It is clear from the plot that the experimental values closely match the theoretical predictions. From this figure it can be concluded that Q and V are measured with better efficiencies in longer wavelength region compared to the design wavelength, where as U is measured with better efficiency at shorter wavelengths.

2.4 Summary

An eight stage modulation scheme to measure the general state of polarization is discussed in this chapter. Beam swapping technique incorporated in this scheme helps in alleviating the gain correction errors. The total polarimetric efficiency is close to unity as the Stokes parameters are weighted equally in all the stages of modulation. The final Stokes parameters are demodulated using all the stages of intensity measurements. Hence, the derived input Stokes parameters are equally

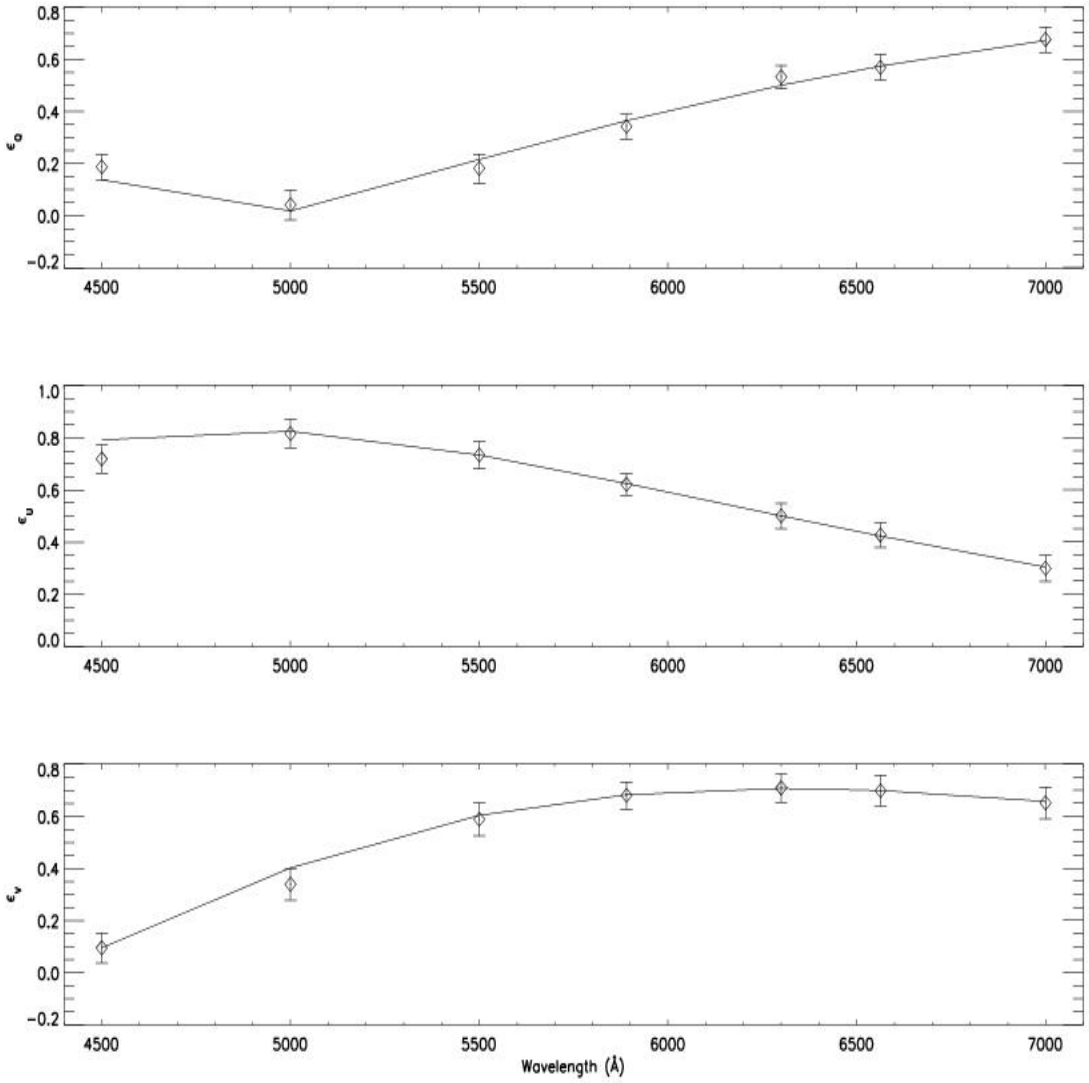

Figure 2.2: Plots of polarimetric efficiency of Stokes Q, U and V parameters as a function of wavelength. The solid curves are theoretical values where as the diamond symbols correspond to the measured values. The error bars shown in these plots are ten times the obtained noise rms values.

weighted time averaged quantities over the measurement time .

Since the retarders used in the polarimeter are chromatic, the efficiency of the polarimeter in measuring Stokes-Q, U, V is wavelength dependent. A laboratory experiment was performed to study the wavelength dependence of the polarimeter efficiency. The experimentally determined polarimetric efficiencies match well with the theoretical expectations.

The measured total polarimetric efficiency of the polarimeter installed at KTT is ≈ 0.986 at $\lambda 6563$ wavelength region which is better than some of the polarimeters such as ZIMPOL (0.72), ASP (0.88), TIP (0.92) and POLIS (0.84) at their design wavelengths.

Chapter 3

Spectropolarimeteric Observations, Data Reduction and Analysis

A dual-beam polarimeter was fabricated and installed at KTT as a backend instrument to the existing spectrograph to perform spectropolarimetric observations on the Sun. For the purpose of measuring a general polarization state of the light, the modulation/demodulation scheme discussed in the previous chapter is used. In this chapter, the spectropolarimetric observations of Sun using this polarimeter and procedures for data reduction and analyses are discussed. The Stokes inversion technique to derive velocity and magnetic field by assuming ME atmospheric model is discussed along with some of the model independent methods to estimate them. The errors involved in estimating the physical parameters from spectropolarimetric data

are discussed. This chapter also describes some of the experiments carried out to characterize the spectropolarimeter at KTT and the intercomparison of magnetic field measurements at KTT with that of space based spectropolarimetric measurements by *Hinode*/SOT.

3.1 Instrument

3.1.1 Telescope and Spectrograph Setup

The instrumental setup at KTT is shown in Figure 3.1. KTT is a 3 mirror coelostat system with the first mirror (M1) tracking the apparent position of the Sun, the second mirror (M2) reflects the light from the first mirror vertically down and the third mirror (M3) folds this vertical beam into a horizontal beam. The parallel beam from M3 is focussed on to the spectrograph slit using an achromatic lens (marked as L1 in Figure 3.1). The diameter of L1 is 38 cm and produces an f/90 beam with the image scale of 5.5″/mm (or 0.142″/pixel on the currently used charge-coupled-device marked as CCD1 in Figure 3.1 after binning 2×2 pixels). CCD1 is a 2K×2K detector with 13.5 μ square pixel. The spectrograph is a Littrow mount optical setup equipped with a grating of 600 lines/mm. The linear dispersion of the spectrograph is 5.6895 mÅ/pixel on CCD1. Further details on KTT and spectrograph setup can be found in Bappu [1967]. Recent additions such as the dual-beam polarimeter and

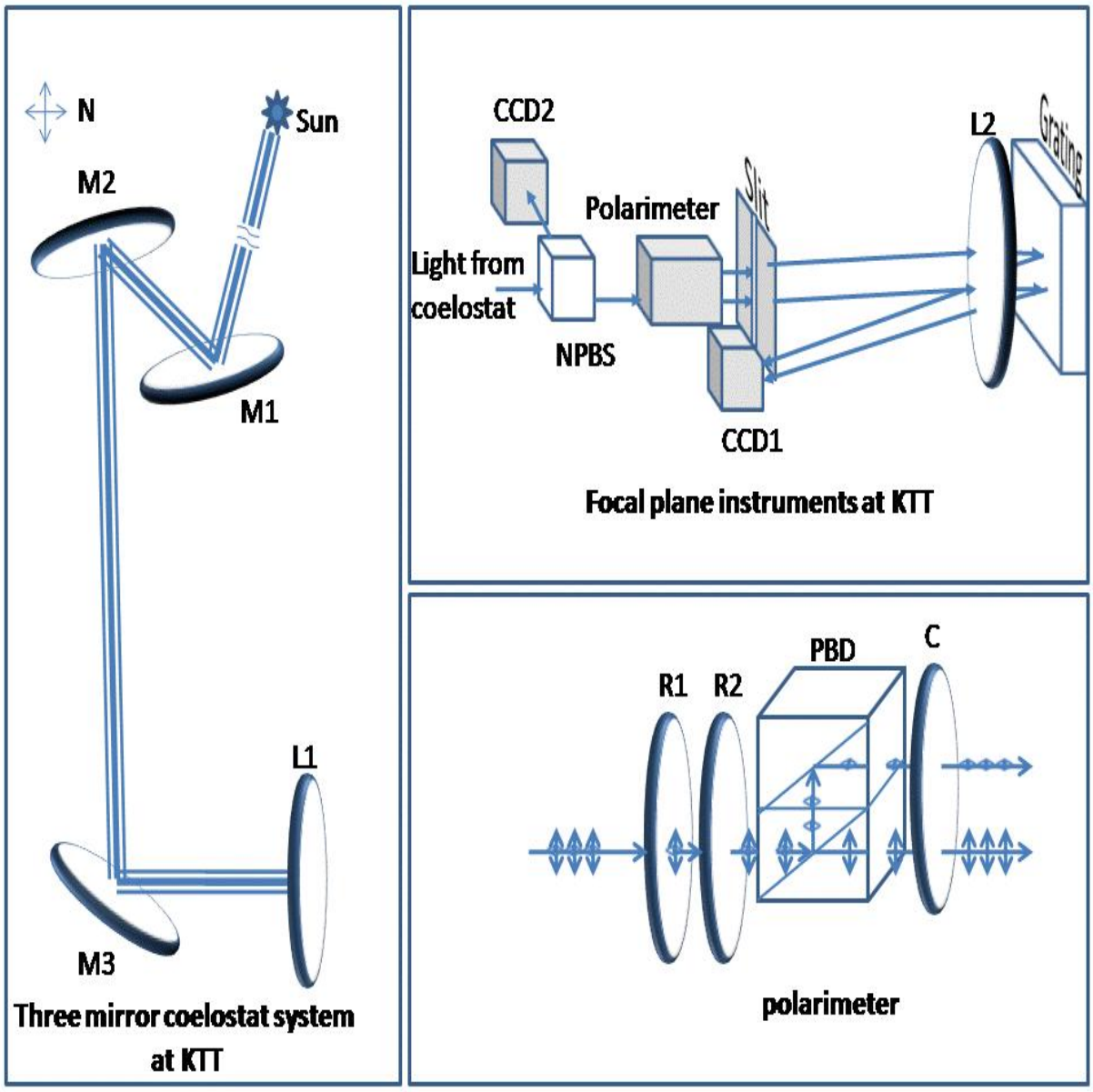

Figure 3.1: Schematic diagram of the spectropolarimetric observing setup at KTT. The terms in the diagram are L1 - objective of the telescope, L2 - acts as collimator as well as imaging lens, NPBS - Non-Polarizing Beam Splitter, CCD1 and CCD2 - charge coupled devices for recording spectrum and wide band images, respectively. The arrangement of the polarization optics is shown on the bottom right corner of this figure.

imaging a region-of-interest (ROI) are discussed in the following sections.

3.1.2 Polarimeter Setup

The polarimeter consists of a polarizing beam displacer (PBD) and two retarders (quarter wave and half waveplates at 630 nm marked as R1 and R2 in Figure 3.1, respectively). The retarders mounted on separate rotating stages are placed in front of the PBD with R1 followed by R2. The whole polarimeter setup is being placed in front of the spectrograph slit (Figure 3.1). The two beams coming out of the polarimeter are orthogonally linearly polarized with the direct beam polarized in the direction of the slit and the vertically displaced beam polarized in the perpendicular direction. The clear aperture of the PBD is 10 mm $\times$ 10 mm which restricts the field-of-view (FOV) to $55'' \times 55''$ on the Sun. A linear polarizer is placed behind the PBD with its optic axis at 45^o with respect to the spectrograph slit to compensate for the differential response of the spectrograph grating to the orthogonal states of linear polarization. The orthogonally polarized beams, after dispersion, are recorded using a CCD camera (marked as CCD1 in Figure 3.1), placed just below the spectrograph slit.

3.1.3 Imaging Setup

To perform simultaneous imaging of ROI in continuum wavelength band, a non-Polarizing beam splitter (NPBS) is used to split the beam entering the polarimeter into two. Reflected beam forms the image on a CCD (marked as CCD2 in Figure 3.1) and the transmitted beam is used for spectropolarimetric measurements. The NPBS is made of BK7 glass with a transmission-reflection ratio of 50%. The clear aperture of the beam splitter is 126″. Right now the images are taken through a broad band filter (band width of 800 Å). This imaging facility can be used with narrow band filters centered around the spectral lines originating in the chromosphere (for eg. H α or Ca II K) to help in positioning the spectrograph slit on the chromospheric structures, which can not be seen in white light images.

To identify the corresponding slit position on the image, a circular aperture was introduced in front of the NPBS. This aperture forms circular images on the slit as well as on CCD2. The position of this aperture was adjusted such that the center of the circular image passes through the slit. Hence the pixel column at the center of this circular image recorded by CCD2 would roughly correspond to the slit position. Even though this is a crude way of identifying the slit position on the image, the mislocation of the slit found to be well within the resolution element. This was confirmed by comparing the intensity variation across the raster images of spectropolatimetric observations. Since the magnification of the image by the spectrograph is almost equal to 1 and no other optics except the filters are used

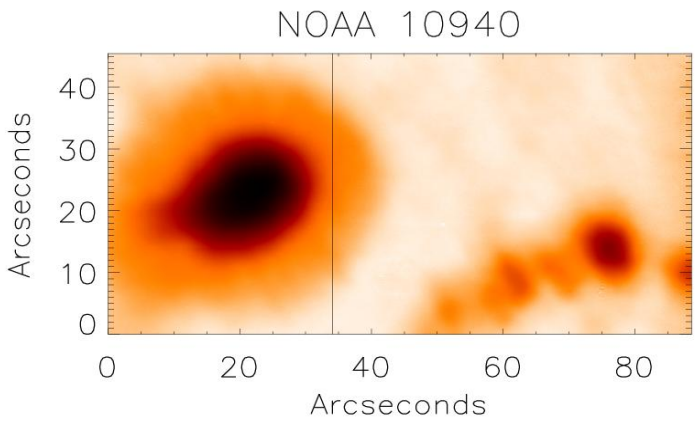

Figure 3.2: A sample image of active region NOAA 10940 obtained using the imaging facility at the focal plane of KTT with an artificial slit marked on it. This active region was observed on 1 February 2007.

for imaging, the image scales in the images and spectrum along the slit direction are same. A sample image is shown in Figure 3.2 with an artificial slit marked on it. Identification of the slit could be done in a more systematic way by having a re-imaging facility in which case a reference hair line could be placed in the input image plane of the re-imaging system and the slit location could be identified more accurately on the images. This is being planned for future observations.

There is a disadvantage with the currently used NPBS as its transmission-reflection ratio is 50% and hence the photons available for spectropolarimetry are reduced atleast by half. On the other hand, the available photons are in excess for wide band imaging. A NPBS with an appropriate transmission-reflection ratio can be selected

for future observations.

3.1.4 Scanning the ROI

Scanning the ROI on the Sun are usually done by moving the Sun's image in the east-west direction in steps of $\approx 2''$ during good/moderate seeing conditions and $\approx 5''$ during bad seeing conditions. Movement of the Sun's image is done by rotating the second mirror about east-west (for north south movement of the image) or north-south (for east-west movement of the image) direction using an electronic control system available at the observing point. The seeing conditions at Kodaikanal are moderate with seeing limited spatial resolution ranging from $2''$ to $4''$. White light images of the ROI are recorded for each stage of polarization modulation.

3.2 Data Reduction

In this section, the steps involved in spectropolarimetric data reduction are explained which include flat fielding, blend removal, correction for polarimeter and telescope responses to the input light.

3.2.1 Flat Fielding

The modulation/demodulation scheme, with the beam-swapping technique incorporated, discussed in previous chapter helps in obtaining Stokes - Q, U, V images which are free from flat field errors. However, for Stokes - I images flat field corrections are necessary. We follow the flat field procedure given by Schlichenmaier and Collados [2002] and Beck et al. [2005]. This procedure involves recording of spectral images, without changing the observing setup, by moving randomly the solar image close to disk center over the spectrograph slit during exposure. The region close to disk center which does not show any visible activities should be chosen to make sure that the spectrograph slit is uniformly illuminated. The random movement of the Sun's image smears out the solar structures and reduce the shifts in spectral lines due to granulation. Even though uniform light along the slit is obtained, the spectral features remain in the spectral images. Spectral lines are the main features that appear in the spectral images. These are removed by dividing each profile by an average profile taken along the slit. Before doing this, shifts in the spectral lines (also some times called as spectral curvature) should be corrected (Figure 3.3). If this curvature is not corrected for, difference in images will show Stokes-V like profiles. Since Stokes images are obtained using difference in images corresponding to orthogonal states of polarization, the spectral curvatures need to be taken into account.

Finding out the shifts in spectral lines and correcting for them is done as follows. In the case of dual-beam spectropolarimetry, there are two spectral images

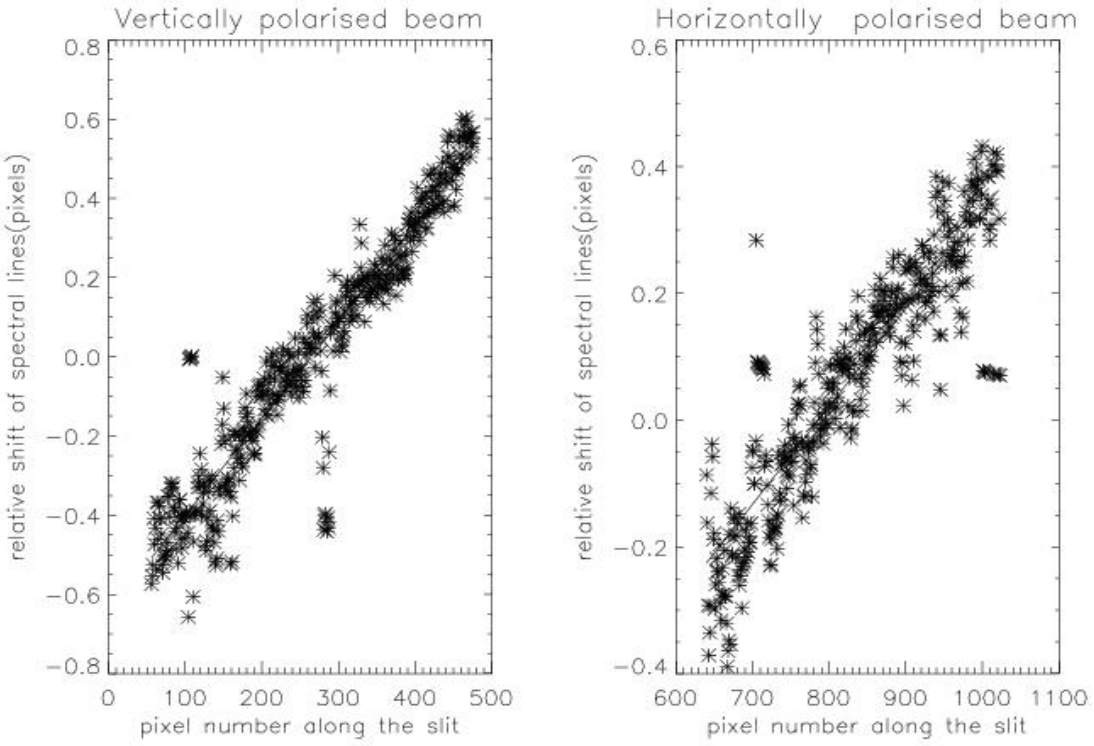

Figure 3.3: Plots of relative shifts of spectral lines with respect to a reference profile along the slit. The solid line is a polynomial fit to the measured line shifts. The points which are well away from the linear curve corresponds to dust particles.

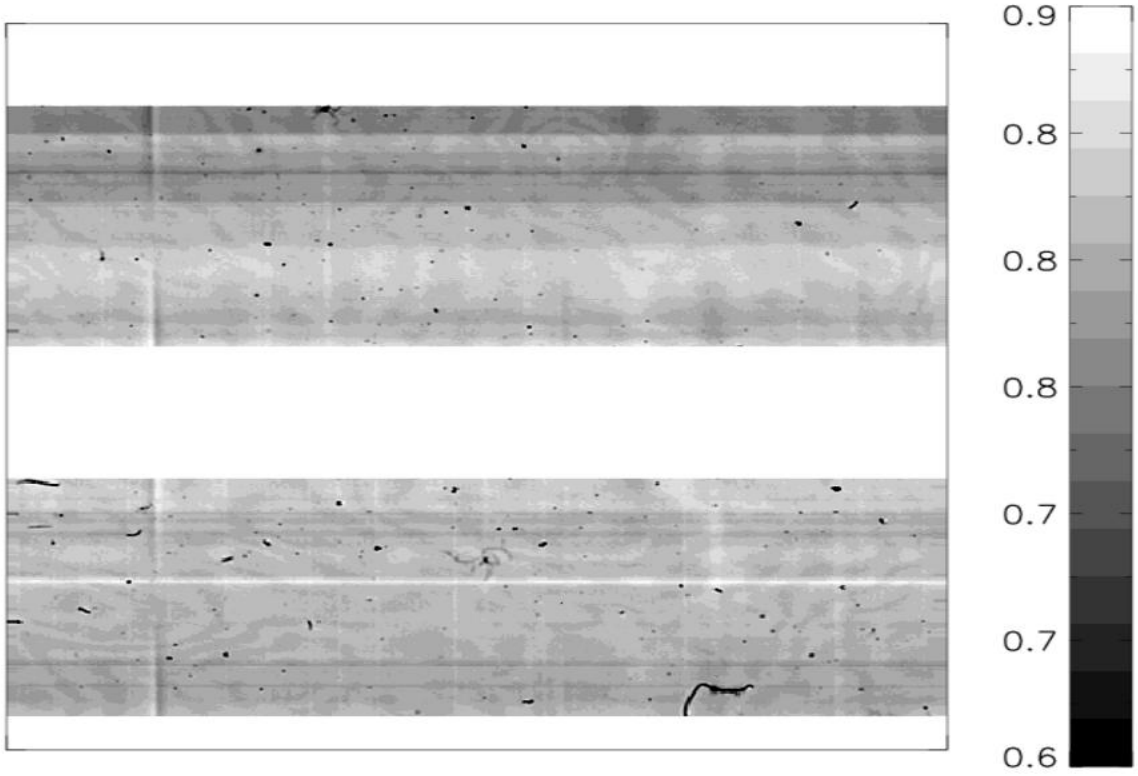

Figure 3.4: Resultant flat field frame without accounting for relative spectral line shifts along the slit for two beam spectropolarimetric observations. The dark spots are due to dust particles and the bright lines in vertical direction are due to these dust particle. The horizontal line in the bottom image is due to a cut in the slit. The two images correspond to horizontally polarized (top) and vertically polarized (bottom) beam.

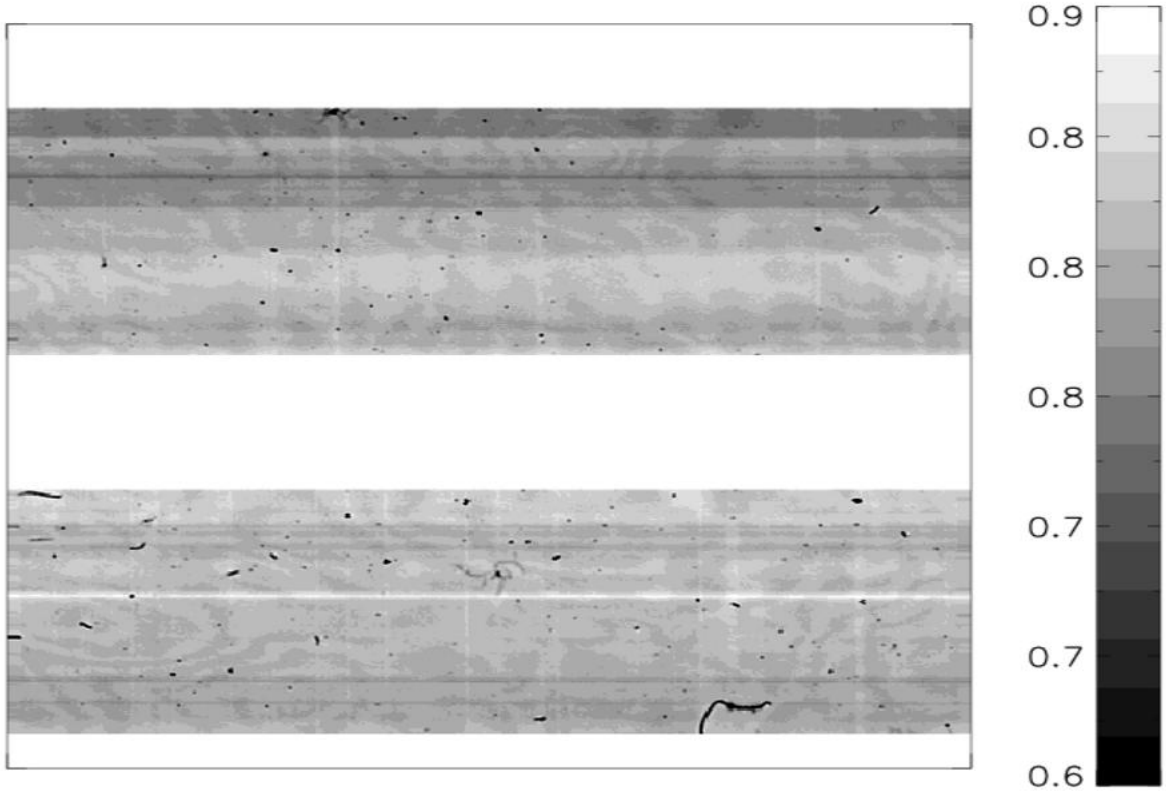

Figure 3.5: Resultant flat field frame obtained after correcting for spectral curvatures. Notice that the Stokes-V like spectral structures, seen in Figure 3.4, are not visible in this flat frame.

that correspond to vertically and horizontally polarized beams. The two beams are considered separately for finding out the spectral curvature. A reference profile is considered at the center of the chosen beam. The shifts of the other profiles with respect to the reference profile within this beam are obtained using a correlation technique. The shifted values are fitted to a polynomial of order one and these fitted values are used for aligning the spectral lines using a Fourier shift algorithm. After aligning the spectral lines, each profile is divided by the average profile taken along the slit for the chosen beam. The resultant frame is shifted back to keep the gain table factors matching with the observed frames. The final flat frame is shown in Figure 3.5. Notice in this figure that the Stokes-V like spectral features, which appear in flat frame obtained without correcting for the spectral curvature (Figure 3.4), have disappeared. The gain table difference between the two beams is corrected by using the ratio between the maximum of each beam.

The flat field procedure outlined above has advantages in removing optically induced gain table errors, polarization dependent fringes, the effects due to non uniformity of the slit and etc. But, if the dust particles are too big then the pixels in the corresponding column will be affected (which appear as vertical strips in Figure 3.5). This will not be a major concern if the dust particle does not fall on the spectral features and can be removed by carefully cleaning the CCD window.

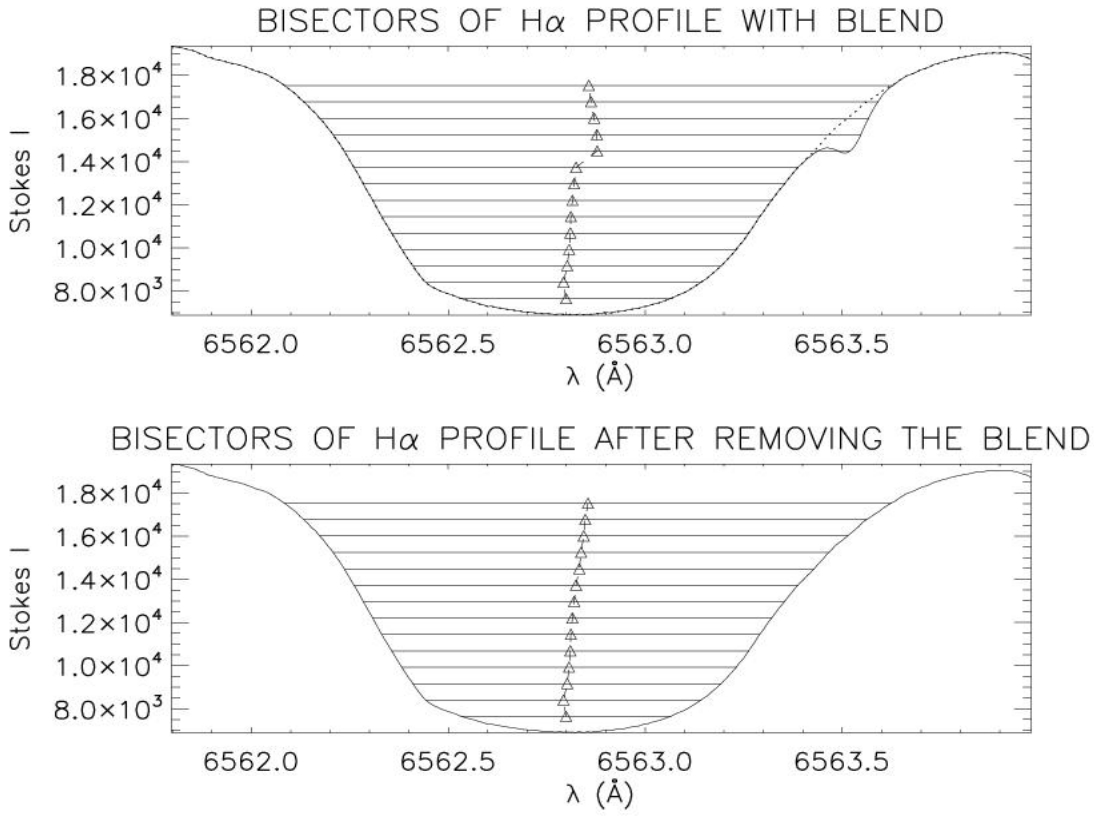

Figure 3.6: Typical H α Stokes I profile with the bisectors marked in diamond symbols with Co I blend (top) and after removing the blend (bottom). Dotted line in the top panel shows the spectral region of the profile after removing the blend.

3.2.2 Blend Removal Procedure

One of the motivations for this thesis is to study the structuring of velocity and magnetic fields from the photosphere to chromosphere. For this purpose, H α line at λ6563 and Fe I line at λ6569 are chosen which form at the chromosphere and photosphere, respectively. The reasons for choosing these lines are explained in section 1.6 of chapter 1 and also in subsequent chapters. Extraction of full information that contained in a spectral line is possible only if the full profile is available for analysis. But, the red wing of H α is blended by the Co I line at λ6563.4, which is a Zeeman sensitive line visible mostly in strong magnetic regions. We explore here a procedure to remove this blend in order to use the full H α line to derive velocity gradients over the line formation height.

Individual profiles of H α that correspond to orthogonally polarized beams in each stage of modulation are considered separately for the removal of Co I blend. A function which is a linear combination of a Gaussian and a quadratic term was fitted to the blend region of the observed H α profile. This non-linear least square fit takes into account the curvature in the intensity profile of H α line along with the Co I line profile approximated to a Gaussian. The Gaussian, constructed out of the fitted parameters, was removed from the observed profile. Then the eight intensity measurements were combined to obtain the Stokes - I, Q, U, V spectral images through the demodulation procedure explained in Nagaraju et al. [2007] (cf. chapter 2). A typical H α intensity profile before and after the blend removal is shown in

Figure 3.6 with the bisector locations marked in triangle symbols.

Even though it appears that the effect of Co I line is completely removed in the total intensity profile, the blend residuals still appear in Stokes Q, U, and V profiles (cf. Figure 4.2). This is because of the limitation of the blend removal method described above. The method approximates the blended line as a Gaussian which is easily discernible. But, this Gaussian does not represent the full profile of Co I line because of the large absorption in H α which dominates the absorption of this line on its blue wing. Hence the contribution from the bluer side of the Co I line is not completely removed in this method. These effects are clearly seen in Stokes - Q, U, & V profiles (see Figure 4.1 in chapter 4). However, the contribution from redder part of the Co I line is removed quite well through the method described here as we can see in Figure 3.6. Also it is demonstrated in later chapters of this thesis that the blend residuals do not have any effect on the velocity gradients calculated from intensity profiles of H α.

A better way to remove the blend would be to synthesize the Stokes profiles of Co I line using the atmospheric parameters obtained through Fe I (λ6569) line and remove them from the observed spectra. This method involves solving the radiative transfer equation. However in this thesis only Stokes-I profiles are considered for the velocity gradients estimation. And the restricted spectral range of H α about line center or the polarization values in the blue wing of H α are considered for the magnetic field estimation. Hence, the simple method outlined above would be

sufficient for the purpose of studying the velocity stratification in the chromosphere.

3.2.3 Polarimeter Response

The next step in data reduction is to correct for the polarimeter response. For this purpose, the polarimetric calibration data are obtained almost on daily basis during observations using a calibration unit (CU). The calibration unit consists of a linear polarizer (P_{CU}) followed by a quarter wave retarder (R_{CU}) at $\lambda 6300$. This is the same retarder used in the experiment to study the wavelength dependence of efficiency for the modulation scheme detailed in the previous chapter. The calibration data are obtained by keeping the orientation of the CU polarizer, P_{CU}, at 0^o with respect to the $+Q$ direction (along the slit direction) and varying orientations of CU retarder with respect to P_{CU}. The orientation of R_{CU} is changed from 0^o to 180^o in steps of 15^o and hence producing 13 input states of polarization. Out of 13 states of polarization, only 11 are different because the polarization states corresponding to the retarder orientation 0^o, 90^o and 180^o are essentially the same. The response matrix of the polarimeter is obtained as follows. If $\mathbf{S}^i_{ip}$ and $\mathbf{S}^i_{op}$ represent the input and output Stokes vectors of i^{th} position of R_{CU} then

$$\mathbf{S}^i_{op} = \mathbf{M}\mathbf{S}^i_{op}. \tag{3.1}$$

Matrix transpose of this equation is

$$(\mathbf{S}^i_{op})^T = (\mathbf{S}^i_{op})^T \mathbf{M}^T. \tag{3.2}$$

The input Stokes parameters and measured Stokes signals are arranged in a 13×4 matrix form to solve for the response matrix $\mathbf{M}$. If $\mathbf{S}^c_{in}$ represents the 13×4 input Stokes matrix and $\mathbf{S}^c_{op}$ represents the measured 13×4 signal matrix then Eq. 3.2 can be written as,

$$\mathbf{S}^c_{op} = \mathbf{S}^c_{in} \mathbf{M}^T. \tag{3.3}$$

The response matrix of the polarimeter setup ($\mathbf{M}$) is solved by defining $(\mathbf{S}^c_{in})^T \mathbf{S}^c_{op} = (\mathbf{S}^c_{in})^T \mathbf{S}^c_{in} \mathbf{M}^T = \mathbf{S}\mathbf{M}^T$ as (see Beck et al. [2005] for details)

$$\mathbf{M}^T = \mathbf{S}^{-1} (\mathbf{S}^c_{in})^T \mathbf{S}^c_{op}. \tag{3.4}$$

Where, $\mathbf{S} = (\mathbf{S}^c_{in})^T \mathbf{S}^c_{in}$. The structures of $\mathbf{S}^c_{in}$ and $\mathbf{S}^c_{op}$ are given in the appendix B for the sake of clarity. Individual columns of $\mathbf{M}$ give the response to a pure state I, Q, U and V.

A typical derived response matrix ($\mathbf{M}$) of the KTT polarimeter setup at the continuum wavelength near $\lambda 6563$ is

$$\begin{pmatrix} 1 & -0.0066 & 0.0384 & 0.0461 \\ 0.0048 & 0.5643 & 0.0565 & -0.0016 \\ 0.0074 & -0.0084 & 0.4173 & -0.0065 \\ -0.0053 & -0.0037 & 0.0248 & 0.6835 \end{pmatrix}.$$

The polarimetric calibration errors are calculated using the procedure given by Beck et al. [2005]. The errors are calculated from $\mathbf{B} = \mathbf{S}^{-1}(\mathbf{S}^c_{in})^T$ using the following equations.

$$\sigma_i^2 = \sum_j B_{ij}^2 \sigma_{ij}^2 = \bar{\sigma}^2 \sum_j B_{ij}^2 \tag{3.5}$$

where $i = 1, ...4$ and $j = 1, 2, ...13$ and

$$\bar{\sigma}^2 = \frac{1}{N} \sum_{cal} (\mathbf{S}^c_{op} - \mathbf{S}^c_{in}\mathbf{M}^T)^2. \tag{3.6}$$

To derive Eq. 3.5, the errors of the single measurements, σ_{ij}, are approximated by the total deviation of the fit, $\bar{\sigma}$.

Typical fit error of the second, third and fourth column of the response matrix, which are nothing but the errors in the determination of Stokes - Q, U, V, are 0.003, 0.0036 and 0.0034 respectively. The corresponding noise rms of the measurements are 0.0017, 0.0018 and 0.0023 respectively.

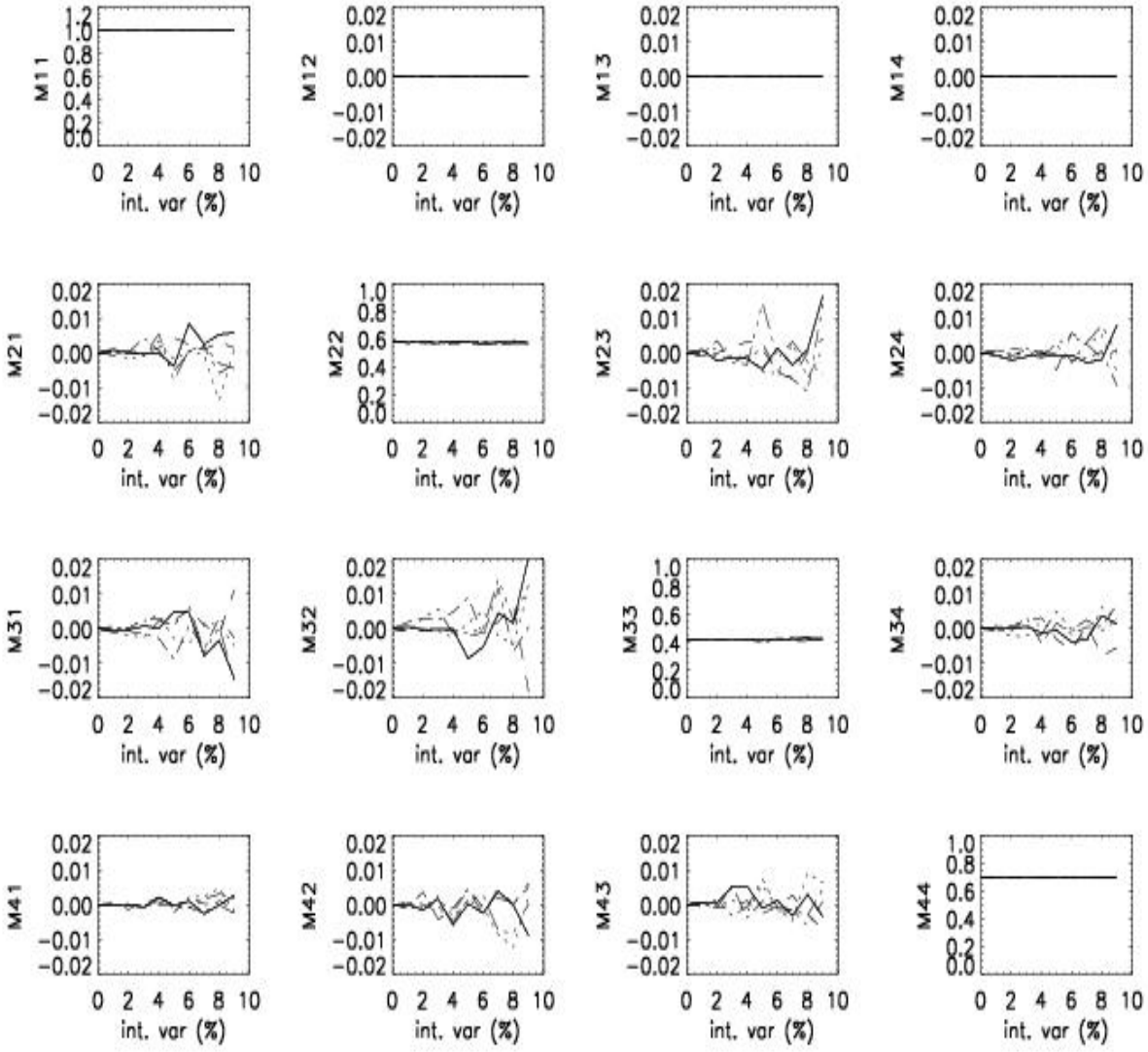

Figure 3.7: These plots show theoretical uncertainties in the calibration of the polarimeter caused due to the variation in the input intensity due to variation in the sky transparency.

It was discussed in chapter 2 that Stokes-Q, U and V are normalized to Stokes-I to alleviate gain table errors. It is assumed that the input intensity does not change during the eight stages of measurements. However, change in intensity within the eight stages of measurements will introduce uncertainties in the determination of the polarimeter response matrix. A simulation has been performed to understand the effect of telescope and the sky transparency variation on the calibration of the polarimeter.

The simulation of the calibration procedure has been performed under the variation in the sky transparency along with the telescope induced effects. To mimic the sky transparency variation, random numbers are generated with the maximum variation within a specified limit. To take into account the telescope induced effects, telescope model has been used (Balasubramaniam et al. [1985]). Plots of the response matrix elements (Eq. 3.4) of the polarimeter are shown in Figure 3.7 as a function of variation in the total intensity due to change in the sky transparency within 8-stages of measurements falling on the telescope. The solid to long dash lines correspond to the local time of observations at one hour of interval from 7am to 12 noon. It is found from this simulation that the variation of 14% in input intensity can cause 1.8% uncertainty in the elements of response matrix. The intensity variation of 14% was maximum during the polarisation calibrations presented in this thesis.

3.2.4 Correction for Telescope Induced Cross-talks

Oblique reflections of the Sun light from the coelostat mirrors of KTT modify the polarization state of input light and hence resulting in cross-talk among Stokes parameters. This is corrected using a telescope model developed by Balasubramaniam et al. [1985] and Sankarasubramanian [2000] for KTT. However, modeling of the telescope induced cross-talk in this thesis has restricted validity because of the use of standard refractive index values of the reflecting layers which may well differ from the actual values. Also, it has been shown by Sankarasubramanian et al. [1999] that for a realistic estimate of the cross-talks, oxide layer on the mirrors need to be taken into account. This requires the accurate measurement of the oxide layer thickness for which separate experimental setup is needed. Since the oxide layer thickness changes with time, measuring it often is not feasible. Hence there still remain residual cross-talks among Stokes parameters even after telescope induced cross-talks are corrected using the telescope model. The cross-talks from I to Q, U and V are removed requiring that no significant polarization signal occurs in the wavelengths corresponding to the continuum towards the redder wavelength regions of the solar spectrum (Fluri and Stenflo [1999]). After correcting for cross-talk from total intensity to polarization profiles, the cross-talks among Stokes Q, U and V are removed using a statistical method (Sanchez Almeida and Lites [1992], Schlichenmaier and Collados [2002]). This is based on the intuition that the Stokes-Q and U change sign four times along an azimuthal circle within the penumbra, while the sign of V only changes across the magnetic neutral line. Thus, except for spots very close to the

limb, a negligible correlation between linear and circular polarization is expected. Hence the cross-talk among Stokes parameters is mostly of instrumental origin. This is removed by performing a linear fit, for eg. from V to Q, as

$$Q(\lambda) = C_{VQ} V(\lambda), \tag{3.7}$$

where C_{VQ} is interpreted as a coefficient of cross-talk from V to Q. This cross-talk term is removed to get the actual Q profile as

$$Q_{\rm actual}(\lambda) = Q(\lambda) - C_{VQ} V(\lambda). \tag{3.8}$$

Similarly the cross-talks from V to U is removed. To remove cross-talk from linear to circular polarization, a linear fit $V(\lambda) = C_{QV} Q(\lambda) + C_{UV} U(\lambda)$ is performed and the actual $V(\lambda)$ is obtained through $V_{\rm actual}(\lambda) = V(\lambda) - (C_{QV} Q(\lambda) + C_{UV} U(\lambda))$. Depending on the location and region of observations the cross-talks from circular to linear polarization and linear to circular polarization dominates. The criteria to consider which one should be used is based on relative amplitudes of Stokes Q, U and V. 3.8.

Stepwise reduction of Stokes profiles is demonstrated in Figure For clarity, only the Fe I (λ6569) Stokes profiles are shown in this figure. The profiles shown in this figure correspond to a spatial location in the penumbral region of NOAA 10940 observed on 1 February 2007. The dotted lines in this figure are the observed profiles. The profiles shown in dashed lines are after correcting for polarimeter response.

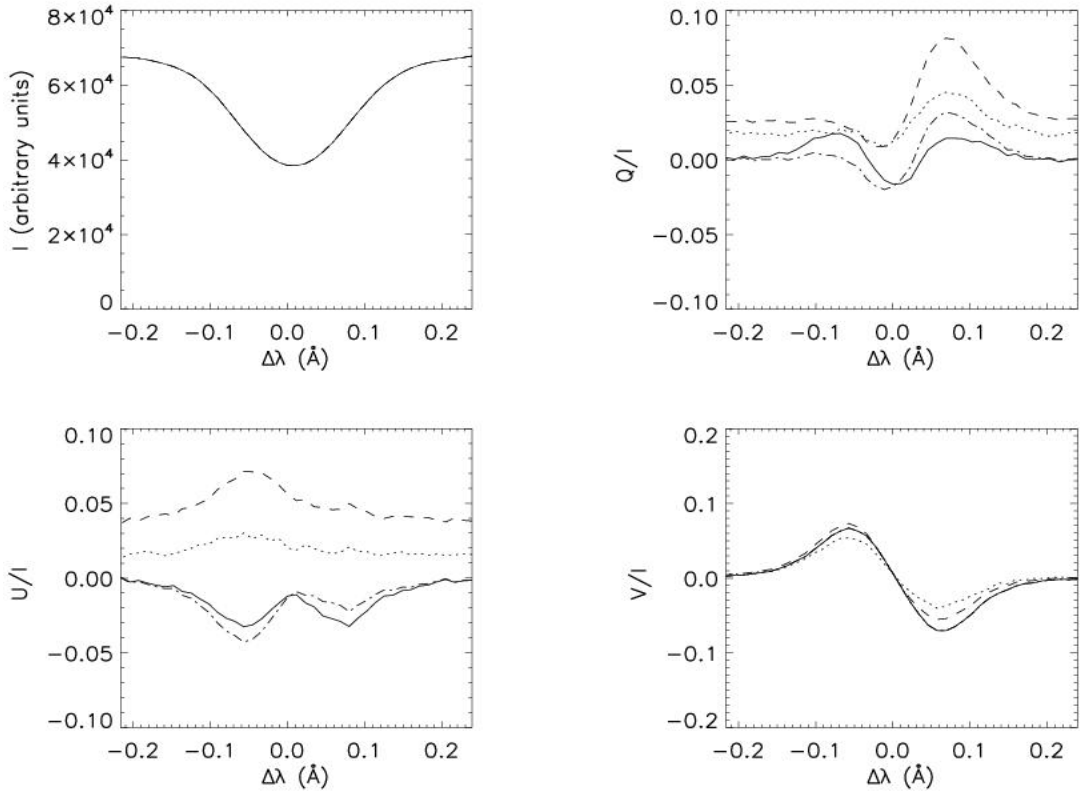

Figure 3.8: Demonstration of removal of the cross-talk among Stokes parameters. Observed Fe I (λ6569) Stokes profiles are shown as dotted curves and the dashed curves correspond to the profiles after correcting for the polarimeter response. Dash-dotted curves are the Stokes profiles after correcting for the telescope induced cross-talk using the telescope model and solid curves are the final Stokes profiles after correcting for the residual cross-talk using a statistical method. The profiles correspond to a spatial location on active region NOAA 10940 observed on 1 February 2007.

The Stokes profiles shown in dash-dotted lines are after correcting for cross-talks among them using a telescope model developed by Balasubramaniam et al. [1985] and Sankarasubramanian [2000]. The solid curves are the final calibrated profiles which are obtained after correcting for the residual cross-talks among Stokes parameters using the statistical method [Sanchez Almeida and Lites, 1992, Schlichenmaier and Collados, 2002].

3.3 Spectropolarimetric Data Analysis Techniques

In this section, spectropolarimetric data analysis procedures to derive velocity and magnetic fields are discussed.

3.3.1 LOS Velocity and Magnetic Field Through COG Method

Model independent estimation of the physical parameters is always preferred because they are less ambiguous. COG method is one such model independent method to estimate the LOS velocity and magnetic field. It was discussed in detail by Uitenbroek [2003] that the COG is an accurate method for LOS velocity measurements and is independent of spectral resolution.

This is also an accurate method to estimate the LOS magnetic field strengths if

the spectral line broadening due to Zeeman effect is smaller than the Doppler broadening. Since the Doppler broadening of the chromospheric spectral lines is orders of magnitude larger than the Zeeman broadening, this method is useful to derive LOS field strengths from chromospheric lines. However, its accuracy is limited for an arbitrarily oriented strong magnetic field (Zeeman broadening > Doppler broadening) and is not accurate method compared to inversion. But, inversion techniques are not yet developed to infer magnetic fields from H α Stokes profiles. Hence, the COG and/or WFA methods are used to derive LOS field strengths at the chromosphere. WFA method can be used to derive vector magnetic field as well.

3.3.2 LOS Velocity

The COG wavelength λ_{COG} of a line profile I is defined as the centroid of its residual intensity profile:

$$\lambda_{\rm COG} = \frac{\int \lambda(I_{\rm cont} - I)d\lambda}{\int (I_{\rm cont} - I)d\lambda}. \tag{3.9}$$

The LOS velocity with respect to the average quiet Sun reference ($\lambda_{\rm ref}$) is defined as

$$v_{\rm LOS} = \frac{c(\lambda_{\rm COG} - \lambda_{\rm ref})}{\lambda_{\rm ref}}, \tag{3.10}$$

where c is the speed of the light.

3.3.3 LOS Magnetic Field

For the COG method, the LOS field strength is given by ([Rees and Semel, 1979, Cauzzi et al., 1993, Uitenbroek, 2003, Balasubramaniam et al., 2004])

$$B_{\rm LOS} = \frac{(\lambda_+ - \lambda_-)/2}{4.667 \times 10^{-13} \lambda_0^2 g_L}, \tag{3.11}$$

where λ_0 is the central wavelength of the line in Å, g_L is the Landé-g factor of the line, and $\lambda_\pm$ are the COG wavelengths of the positive and negative circularly polarized components respectively. The COG components are calculated as

$$\lambda_\pm = \frac{\int [I_{\rm cont} - (I \pm V)] \lambda d\lambda}{\int I_{\rm cont} - (I \pm V) d\lambda} \tag{3.12}$$

where $I_{\rm cont}$ is the local continuum intensity. The integration is over the spectral range of a given spectral line.

3.3.4 LOS Velocity Gradients Through Line Bisector Method

Stokes profile asymmetries are known to be caused by the velocity and magnetic field gradients in the line formation region [Illing et al., 1975, Grigorev and Katz, 1975]. Model independent estimation of velocity gradients is possible through bisector technique applied to Stokes- I (e.g., Balasubramaniam et al. [1997]) and Stokes-V (e.g., Sankarasubramanian and Rimmele [2002]) profiles. This method involves finding the

bisector at equal intensity levels within the spectral line from line core to wing. See Figure 3.6 for a demonstration of finding the bisectors at equal intensity levels of H α line. The triangular symbols in this figure represent the bisector locations. If the spectral line is symmetric then these bisectors lie on a vertical line passing through line core, otherwise their locations will be shifted depending on the line asymmetry.

To derive velocity gradients at the photosphere and chromosphere, the Stokes I profiles of Fe I and H α are considered separately for bisector analysis. Bisectors are obtained at 9 equal intensity levels between line core and the wing for Fe I and 14 equal intensity levels between line core and wing for H α, respectively. Out of 9 bisectors of Fe I line only 7 are considered, namely, the bisectors between second and eighth counting from the line core. Similarly for H α the bisectors between second and thirteenth are considered totalling 12 bisectors. The bisectors very close to line core and wing are not considered because of the lower signal-to-noise ratio and to avoid the influence of the continuum respectively. For the Fe I line, the wavelength position of the second bisector which corresponds to higher atmospheric layer was subtracted from the seventh bisector which corresponds to lower atmospheric layer. Similarly for H α, the wavelength position of the second bisector was subtracted from the thirteenth bisector. The wavelength differences ($\Delta\lambda$ s) thus obtained are converted into velocities - which would then represent the velocity difference between the lower and higher atmospheric layers - using the following relation,

$$\Delta V_{bs} = \frac{c\Delta\lambda}{\lambda_0}. \tag{3.13}$$

Where λ_0 is the rest wavelength of the spectral line under consideration. The velocity difference defined in Eq. (3.13) represents the velocity gradient over the line formation height.

The errors in estimating the velocity differences are mainly due to the errors involved in finding the wavelength shifts. The maximum error in estimating the velocity gradients is about 0.09 km s^{-1}.

3.3.5 Stokes Inversion Using Milne-Eddington Atmospheric Model

The photospheric vector magnetic fields are obtained by inverting the Fe I (λ6569) Stokes profiles using the community inversion codes of High Altitude Observatory, Boulder, USA, viz., ASP and MELANIE [1]. ASP stands for Advanced Stokes Polarimeter, a spectropolarimeter operating at the National Solar Observatory, Sunspot, New Mexico, USA. The Stokes inversion code, ASP, is hardwired to use the spectropolarimetric data obtained by ASP instrument. This code was modified to invert the spectropolarimetric data from Kodaikanal. To double check, the results returned by ASP inversion are compared with MELANIE as ASP inversions are usually carried out for Fe I line pairs at λ6300 where as for KTT data the inversion needed is for Fe I line at λ6569. Milne-Eddington Line Analysis using a Numerical Inversion

[1] http://www.hao.ucar.edu/public/research/cic/index.html

Engine (MELANIE) code is more user friendly and easy to use but initialization is not automatic.

Both ASP and MELANIE perform a non-linear least-square fitting of the observed Stokes profiles under Local-Thermodynamic-Equilibrium (LTE) condition by assuming Milne-Eddington (ME) atmosphere. Typical observed and fitted Stokes profiles are shown in Figure 3.9. The plus signs represent the observed data points and solid lines represent fitted profiles. ME model assumes plane parallel atmosphere and the source function is a linear function of optical depth. It is also assumed that the velocity and magnetic fields are constant over the line formation height. Inversion codes return magnetic field strength, inclination angle with respect to LOS, azimuth, line strength, damping parameter, LOS velocity, source function and its gradient with optical depth, macroturbulence and fraction of stray light/fill factor of the non-magnetic component.

The maximum error in estimating the magnetic field strength is ≈ 50 G, the field inclination is about 5^o and its azimuth is 6^o. Other physical parameters returned by the MELANIE are not used in the current work and hence are not discussed here.

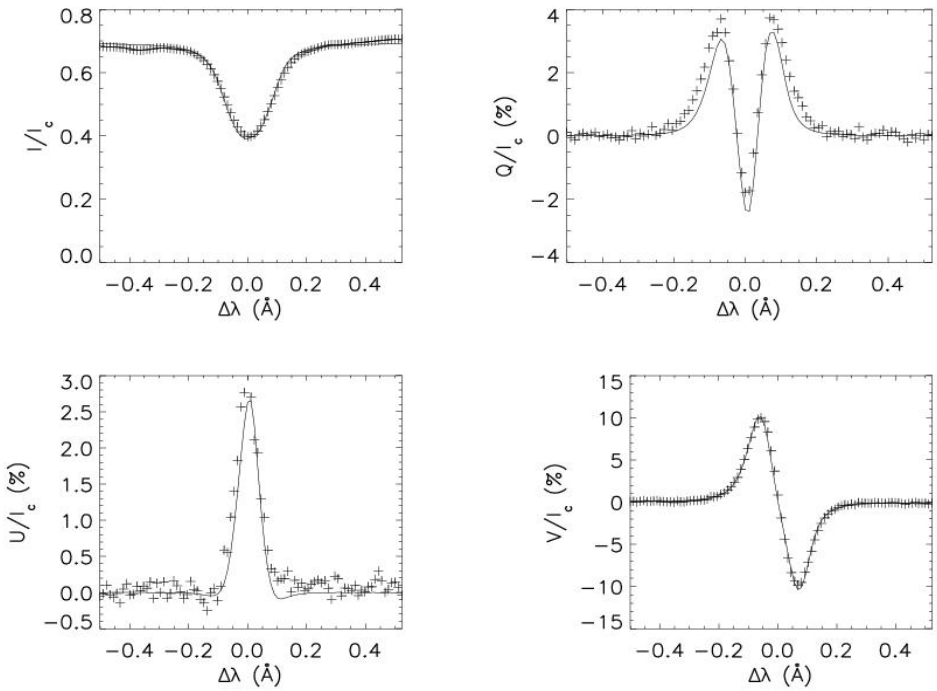

Figure 3.9: Typical observed (plus symbols) and fitted (solid lines) Stokes profiles of Fe I line at λ6569. The profiles are fitted using the inversion code ASP with ME atmospheric model under the assumption of LTE (see text for details). The profiles correspond to a spatial location close to umbral region of NOAA 10940 observed on 1st of February 2007.

3.3.6 Vector Magnetic Field at Chromosphere Through WFA

The chromospheric vector magnetic fields are derived using classical weak-field-approximation (Landi degl'Innocenti and Landi degl'Innocenti [1973], Jefferies et al. [1989], Jefferies and Mickey [1991]) applied to the Stokes profiles of H α. The parallel (along LOS) and perpendicular components of the field were calculated using the formulae, with γ representing the field inclination with respect to the LOS,

$$Bcos\gamma = -wV/(dI/d\lambda), \tag{3.14}$$

$$Bsin\gamma = 2w\sqrt{\frac{\Delta\lambda}{3}\frac{\sqrt{Q^2+U^2}}{dI/d\lambda}} \tag{3.15}$$

where $w = 1/4.67 \times 10^{-13}\lambda^2 g_{eff}$ with λ, the line center wavelength, expressed in Å, g_{eff} is the effective Landé-g factor of the atomic transition under consideration and $\Delta\lambda$ is the wavelength shift from the line center at which the magnetic field is calculated. The field azimuth (χ) is calculated through

$$tan2\chi = \frac{U}{Q}. \tag{3.16}$$

The value '3' appears in Eq. 3.15 is an approximation to the ratio H''/H', the second and first derivatives of the Voigt function with respect to wavelength (see Eq. 10 in Jefferies and Mickey [1991]). The errors in estimating the field strength are < 389G for LOS field strength and < 285 G for vertical field strength. These errors are obtained by converting polarization measurement errors by estimating the error

propagation through Taylor expansion technique (Bevington and Robinson [2003]).

3.3.7 Stokes V Area and Amplitude Asymmetry

Often it is required to verify the consistency of physical quantities inferred from the observations. For instance, the velocity gradients estimated using the bisector technique at the chromosphere from H α intensity profiles need verification because of a blend in its red wing by Co I line (see section 3.2.2), though this was removed from intensity profiles. Since, amplitude and area asymmetries of Stokes V profiles can be caused by the gradients in the velocity and magnetic fields (see for eg. Sanchez Almeida and Lites [1992], Sankarasubramanian and Rimmele [2002]), it is useful to study them atleast for qualitative comparison because, quantitative estimation of the field gradients from them is not understood yet.

If a_r and a_b represent the amplitudes of red and blue wings of Stokes V respectively then the amplitude asymmetry is defined as,

$$\delta a = \frac{|a_b| - |a_r|}{|a_b| + |a_r|}. \tag{3.17}$$

Similarly, area asymmetry is defined through

$$\delta A = \frac{|A_b| - |A_r|}{|A_b| + |A_r|}, \tag{3.18}$$

with $|A_b|$ and $|A_r|$ representing the absolute area of the blue and the red lobes, respectively.

The area asymmetry is not considered in this thesis due to the difficulty in estimating it for the H α in the presence of Co I line blend residuals even after removing it from the intensity profile. One can consider the area asymmetries observed for Fe I line to study the gradients at the photosphere but, our focus is to compare the simultaneous observations at the photosphere and chromosphere.

3.4 Characterization of Spectropolarimeter

As part of characterizing the spectropolarimeter, a few experiments have been carried out. The measurement of spectral resolution has been carried out using a He-Ne laser source. In another experiment, noise in the polarization data has been studied in order to determine the precision of the polarization measurements. Further, the magnetic field measurements are compared with that of space based observations by *Hinode*/SOT.

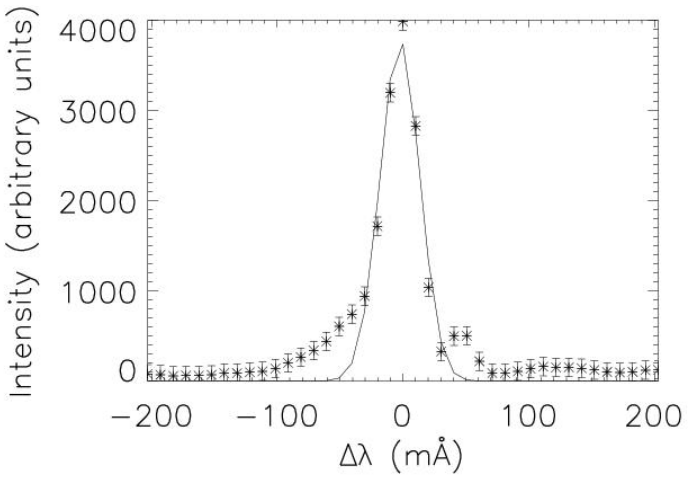

Figure 3.10: A sample laser profile recorded in the second order of spectrum for the slit width of 50μ. A Gaussian profile fit is over plotted on it (solid line). The error bars shown in the plot are the photon noise associated with the intensity measurements.

3.4.1 Spectral Resolution

The spectral resolution of the spectrograph setup is limited mainly by the diffraction grating and the width of the entrance slit. Detector also can play a role depending on the size of the detection elements and the linear dispersion of the spectrograph setup. If the width of the entrance slit is larger than certain value then it will degrade the spectral as well as spatial resolution. The observer can record the spectrum with resolution close to the resolution limit of the grating by choosing the slit width lesser than certain value. Apart from the spectral and spatial resolution, the light level is also important to achieve good signal-to-noise ratio. As we decrease the slit width the amount of light will also decrease considerably. Hence one should choose an

optimum width for the entrance slit in such a way that, it should allow maximum intensity without affecting the spectral and spatial resolution. The physical width of the entrance slit of the spectrograph must have a value s or less in order not to degrade the spectral resolution, where

$$s = \frac{\lambda f}{N d cos\theta}. \tag{3.19}$$

Where, $\lambda-$the wavelength of the radiation, $f-$the focal length of the collimating lens, $N-$ the total number of grooves on the grating, $d-$the grating constant (number of grooves per unit length) and $\theta-$ the angle of diffraction. To identify an optimum slit width and study the spectral resolution of the spectrograph setup at KTT, an experiment was performed using He-Ne laser source. This source produces a spectral line at $\lambda 6328$ with spectral width of ≈ 20 mÅ.

A parallel beam of He-Ne laser was passed through the objective (marked as L1 in Figure 3.1) of the KTT so that the laser beam be focussed on to the spectrograph slit. For a given spectral order, the laser profiles were recorded by varying the slit width from $30-150\mu$ in steps of 10μ. The observed laser profiles were fitted using a Gaussian function. A sample observed profile with the fitted Gaussian profile overplotted on it is shown in Figure 3.10. The Full Width at Half Maximum (FWHM) of the laser profiles were calculated using the standard formula

$$FWHM = 2(\sqrt{2ln2})\sigma, \tag{3.20}$$

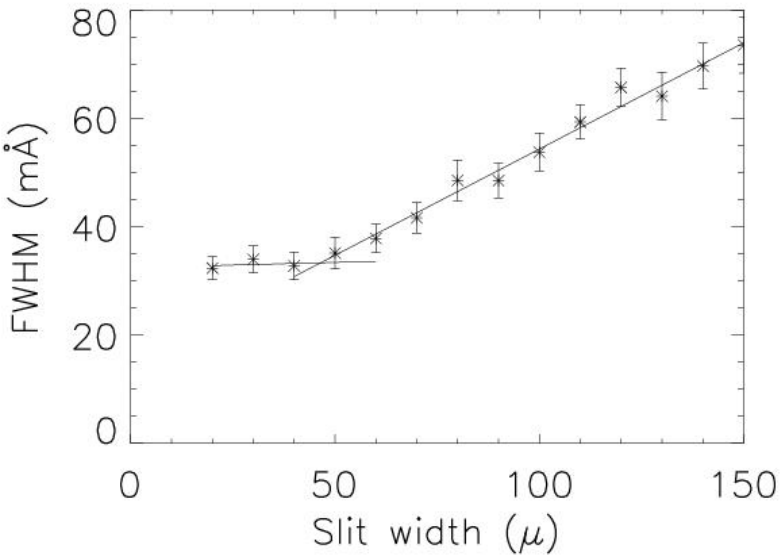

Figure 3.11: Plot of FWHM of He-Ne laser profile (star symbol) as a function of the slit width. The error bars are 3 times the fit error of the FWHM when Gaussian is fitted to the observed profile. The solid lines are the linear fit to the FWHM values fitted separately for the set of values which are almost constant with respect to the slit width and the other set of FWHM values which increase monotonically with the slit width.

where σ is the width of the Gaussian function.

The plot of FWHM v/s the slit width is shown in Figure 3.11. The solid lines in this figure are the linear fit to the FWHM values fitted separately for the set of values which are almost constant with respect to the slit width and the other set of FWHM values which increase monotonically with the slit width. The error bars are 3 times the fit error of the FWHM obtained through Gaussian fit of the profiles.

As one can notice in Figure 3.11 that the FWHM does not change upto the slit width value of $\approx 48\ \mu$ after which it increases monotonically. Hence the optimum slit width for the Kodaikanal spectrograph setup is 48 μ and the corresponding spectral resolution is 32.47 mÅ in the second order of spectrum. For the same slit width, theoretically expected resolution is 35 mÅ. The discrepancy between the measured and theoretical resolutions may be caused due to various reasons. Note that the instrument profile is assumed to be a Gaussian where as the observed profiles differ from ideal Gaussian shape (see Figure 3.10). A systematic inaccuracy in the measured slit width may also contribute to the discrepancy between the experimental and theoretical spectral resolution.

3.4.2 Measurement Noise

Random variation of the measurements is generally known as the noise. In particular the photon noise inherent to the photon flux measurement is generally known as Poisson noise, the readout noise of electronic detector (usually CCD), and noise in the polarization produced due to seeing fluctuations are possible sources of noise in measurements. Usually, modern CCDs produce very little readout noise and seeing induced fluctuations are reduced by using the simultaneously recorded orthogonally polarized beams to form the Stokes parameters. The photon noise can be reduced by recording more number of photons for e.g., by increasing the exposure time. Hence it is important to verify whether the noise in the polarization measurement is limited by the photon noise or due to any other systematic noise. If it is limited by photon noise, then one can perform high precision polarimetry by recording more number of photons, usually through longer integration time for a give optical setup.

A simple experiment was performed in order to determine noise in the measurement of the Stokes parameters and to study its behavior as a function of exposure time. For a given exposure time, set of eight spectral images were recorded by orienting the polarimeter retarders at the angles required for eight stage modulation scheme. These eight intensity measurements were combined according to the demodulation scheme explained in chapter 2 to form Stokes spectral images. The above procedure was repeated for different exposure times varying from 200 to 2400 ms in steps of 200 ms. The standard deviations of Stokes parameters (σ_I, σ_Q, σ_U, and σ_V)

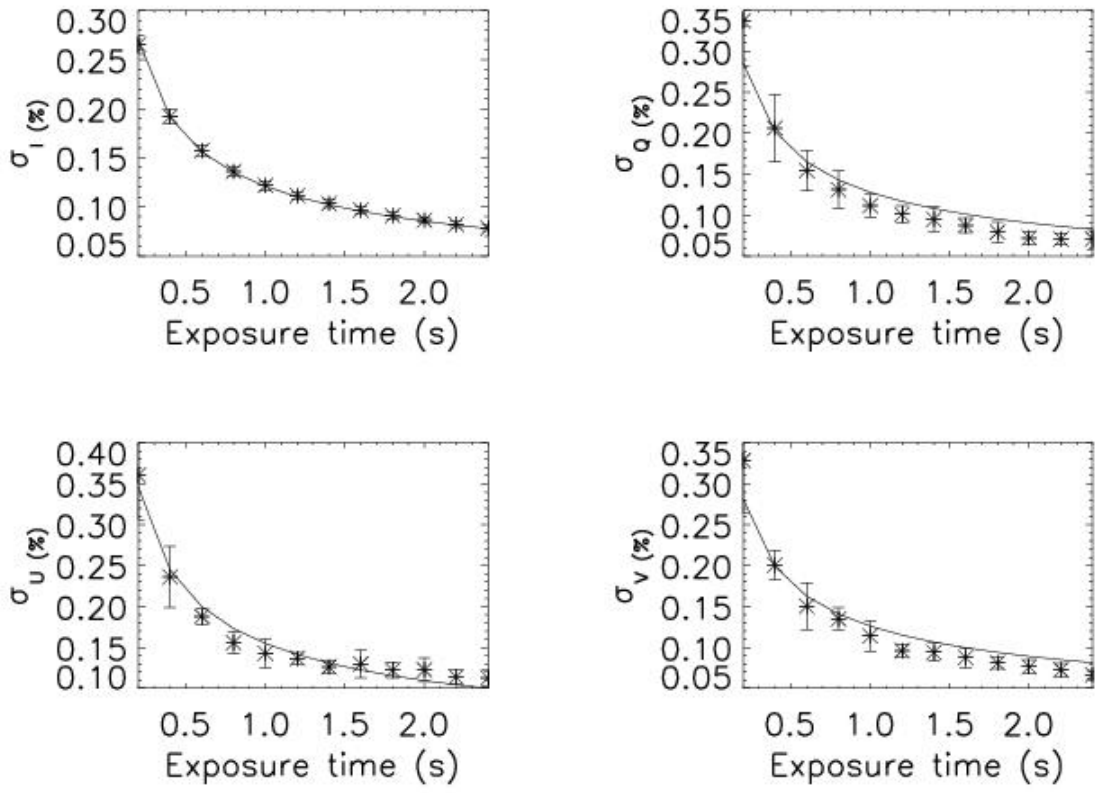

Figure 3.12: Plots of rms noise of Stokes parameters (σ_I, σ_Q, σ_U, and σ_V) as a function of exposure time. Error bars are 2 times the rms variation of σ_I, σ_Q, σ_U, and σ_V are calculated at different wavelength points around λ6563.

were calculated over 256 pixels at different wavelength points in the corresponding Stokes images. σ_I, σ_Q, σ_U, and σ_V represent the noise in the corresponding Stokes parameters. A plot of σ's as a function of exposure time is shown in Figure 3.12 for the Stokes parameters I, Q, U, and V. The error bars are 2 times the rms values of σ's calculated at different wavelengths around λ6563. Note that σs follow closely the Poissonian statistics (solid lines in the plots) implying that the polarization measurements are photon noise limited and hence better sensitivity in the measurement of the Stokes parameters can be achieved by increasing the exposure time. For the exposure time of 2400 ms it was found that the polarimetric precision is better than 0.1%. To conclude, the noise in the polarimeter is limited by the photon noise.

3.4.3 Comparison of Vector Magnetic Field of an Active Region Measured at KTT With That of *Hinode*/SOT

The Solar Optical Telescope (SOT) onboard *Hinode* [Kosugi et al., 2007] carries out the spectroplarimetric observations in Fe I line pairs around λ6300. The spatial and spectral resolutions of SOT are 0.312″ and 21.5 mÅ respectively. *Hinode* carries out the solar observations almost uninterruptedly. The data observed by *Hinode* are available in public domain which can be downloaded. This easy availability of the data provides an opportunity for us to compare the magnetic field measurements carried out at KTT with that of *Hinode*.

Spectropolarimetric data by *Hinode* were subjected to standard reduction procedure (eg. SP_PREP, available through SolarSoft IDL data analysis package). The magnetic field information was derived using the inversion technique discussed in section 3.3.5.

To compare the vector magnetic field measurements at KTT and *Hinode*/SOT at the photosphere, spectropolarimetric observations of an active region are analyzed. The active region considered was NOAA 10940 located close to disk center. The observations of the sunspot at KTT considered in this paper are about 5 and half hours ahead of *Hinode*/SOT observations (cf. Figure 3.2). Vector magnetic fields at the photosphere are obtained by inverting the Stokes profiles of Fe I line at λ6569 for KTT data and Fe I line pair at λ6300 for *Hinode*/SOT data under Milne-Eddington atmospheric model using the HAO inversion code.

For the comparison of the magnetic field measured by these two observations, the image scales are matched using the respective plate scales of the imaging system. Further, the *Hinode*/SOT observations are smoothed by 16×16 pixels (equivalent of $5.12'' \times 5.12''$) to match the seeing degradation at the KTT. Which implies that the effective spatial resolution at KTT for spectropolarimetric observations for this active region is (viz. NOAA 10940) $5.12''$. The scatter plot of field strengths obtained from KTT and *Hinode* are shown in Figure 3.13. The solid line in the plot is the linear fit to the data points and the slope of this linear fit is 1.009. This implies that the magnetic field strengths measured at KTT matches very well with that of

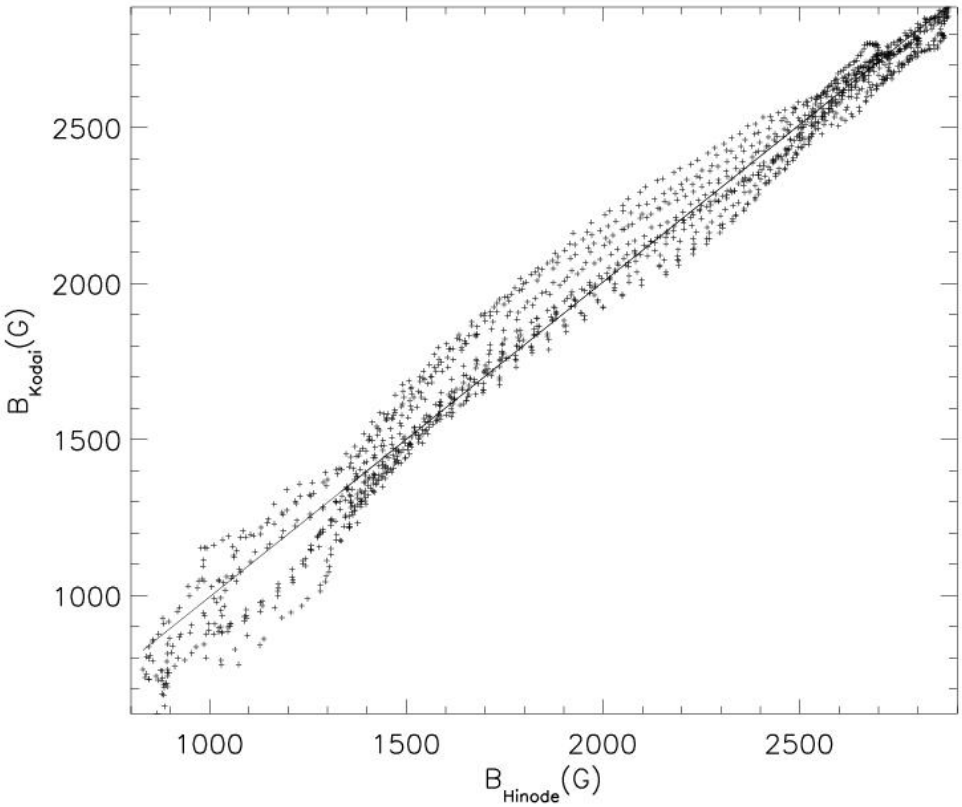

Figure 3.13: Scatter plot of magnetic field strength measured at KTT and by *Hinode*/SOT. The sunspot considered for comparison was NOAA 10940 which was located close to disk center during observations. For the sake of brevity the error bars are not plotted. However, the errors in estimating the magnetic field are less than 50 G.

Hinode/SOT. The scatter in the plot is due to the lack of exact one-to-one spatial correspondence between the two observations.

3.5 Summary

This chapter described in detail the observational setup at KTT along with the procedures of data reduction and analysis. The observing setup includes simultaneous imaging of the ROI and the spectropolarimetry. The polarimetric calibration procedure is discussed in detail along with its accuracy in measuring Stokes parameters. The accuracy in measuring Stokes-Q, U and V are 0.003, 0.0036 and 0.0034, respectively. The cross-talks among Stokes parameters due to the oblique reflections of the light from the coelostat are corrected using the combination of telescope model developed by Balasubramaniam et al. [1985], Sankarasubramanian [2000] and statistical method described in Sanchez Almeida and Lites [1992], Schlichenmaier and Collados [2002]. Spectropolarimetric data analysis procedures such as COG and bisector technique for deriving velocity and its gradients, respectively, are discussed. The inversion techniques and WFA for deriving vector magnetic fields at the photosphere and chromosphere using the Stokes profiles of Fe I λ6569 and H α, respectively, are discussed. This chapter also described the experiment to characterize the spectropolarimeter at KTT. It was found through slit optimization experiment that the optimum slit width for KTT spectrograph setup is 48 μ and the corresponding spectral resolution is 32.47 mÅ. The experiment to study the polarization sensitivity

dependence on the photon noise confirms that the sensitivity in polarization can be achieved better than 0.01% for an exposure time of 2.4 secs. Finally, the comparison of magnetic field measurements at KTT with that of *Hinode* are discussed. The field strengths obtained from KTT data matches very well with those obtained by *Hinode* data after a spatial smearing of the later data by $5.12'' \times 5.12''$.

Chapter 4

Magnetic Field Topology Above the Active Regions

It was reported earlier by Balasubramaniam et al. [2004] & Hanaoka [2005] that the LOS field strengths obtained through H α observations are anomalously weak in the umbral chromosphere. Balasubramaniam et al. [2004] have analyzed the simultaneous spectropolarimetric observations in H α and Fe I line at λ6301.5 and Hanaoka [2005] compared the LOS field strengths obtained from H α magnetograms with that of *SOHO*/MDI[1]. Gosain and Prasad Choudhary [2003] have also reported systematic weakening of the LOS field strengths derived from Mg I λ5173/5184 lines in comparison with that of Fe I λ6301.5/6302.5 lines. In their case, the LOS field

[1]see Appendix C for more details

strengths measured by Mg I lines agree with the potential field extrapolation of the photospheric LOS magnetic field in weak field regime. In strong field regime there is a systematic shift toward lower values but still linear.

Various possibilities have been discussed by Balasubramaniam et al. [2004] & Hanaoka [2005] about the weaker chromospheric fields observed in umbra. Hanaoka [2005] have discussed the possibility of scattered light and/or peculiarity of the atmosphere (radiative transfer effects) for a decrease in the polarization signal which in turn cause the underestimation of the magnetic field strength. Balasubramaniam et al. [2004] have suggested that the strongest fields measured at the photosphere diverge spatially and more quickly than the weak fields when they propagate upward.

It is important to note that the observations mentioned above have compared only the LOS field strengths at the photosphere and chromosphere. The quicker weakening of the LOS field strengths in the umbra can be caused either due to the actual weakening of the field strengths or due to the quicker bending of the fields as they propagate from the photosphere to chromosphere. It is important to clarify this issue for understanding the stratification of the magnetic field in the solar atmosphere. This requires inference of vector magnetic field.

Another major difficulty in interpreting the H α observations is the ambiguity in its height of formation. Studies based on the response functions by Socas-Navarro and Uitenbroek [2004] show that H α is sensitive mostly to chromospheric magnetic

field in the umbral model, while in the quiet sun model it shows sensitivity to both photospheric and chromospheric magnetic field. Since the magnetic field at the photosphere is in general large, the magnetic field inferred through H α observations in quiet sun regions will be mostly photospheric. For the same reason, if H α were to show the sensitivity to magnetic field in the penumbral model similar to that of quiet sun model, then the field strengths inferred through this line will be larger in the penumbral region compared to umbral region.

To overcome these ambiguities, a lot more effort is needed both from theoretical and observational side. From theoretical side, more forward modeling is needed which will include the comparison of H α line formation at different regions of the Sun with different field configurations. Also, the response of H α line to various physical parameters needs to be studied to use it to its full potential. As part of this thesis work, we explore how effectively the H α line can be used as a diagnostic to understand the chromospheric dynamics through spectropolarimetric observations complimented by a Zeeman sensitive Fe I line at λ6569 which can be recorded simultaneously with H α on the CCD available at KTT. As noted earlier, Fe I originates from the photosphere.

Spectropolarimetric observations of several active regions have been carried out at KTT using the polarimeter described in the previous chapters. We present in this chapter the magnetic structure above three active regions from the photosphere to chromosphere. The wavelength region chosen for spectropolarimetric observations

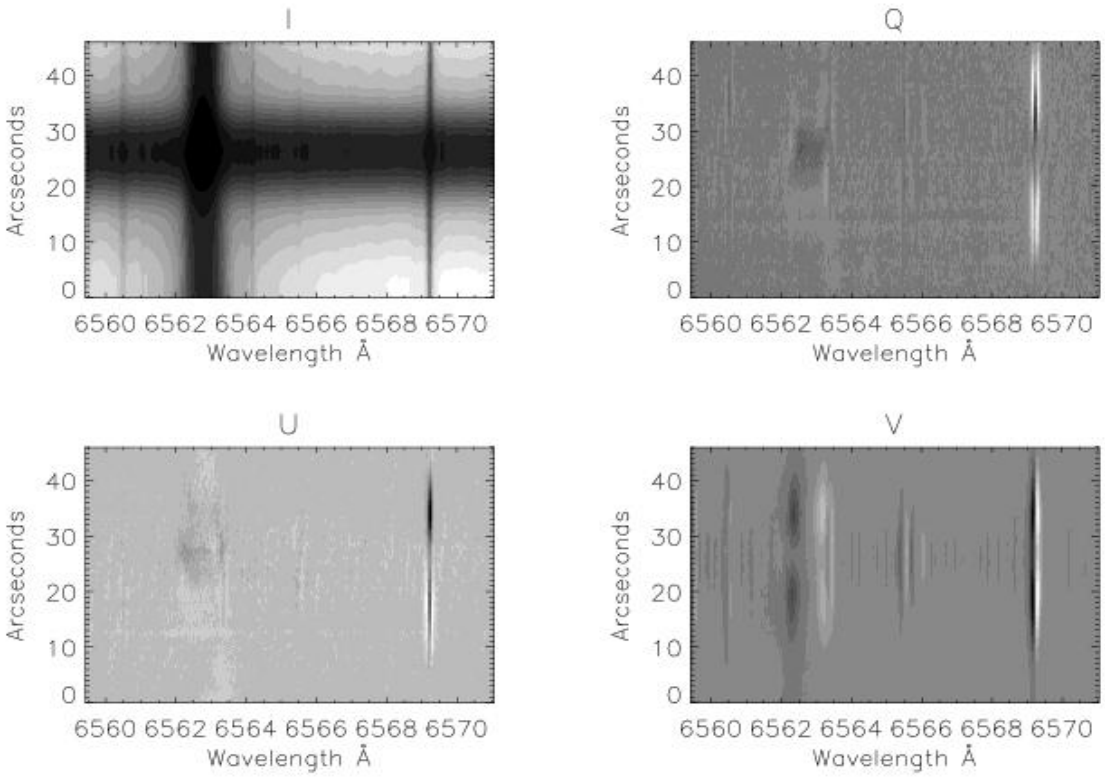

Figure 4.1: Typical Stokes images for a slit position close to central umbra of the active region NOAA 10940. Dark horizontal band in the Stokes-I image corresponds to the umbral region. Notice that H α Stokes-Q & U are stronger in the umbral region compared to penumbral region while they exhibit exactly opposite behaviour in Fe I spectral range.

includes H α and Fe I at λ6569. These lines are useful in studying the dynamic coupling between the photosphere and chromosphere as H α (λ6563) forms at the chromosphere [Vernazza et al., 1981, Rutten, 2007] and Fe I line (λ6569) originates at the photosphere. Both these lines are Zeeman sensitive with effective Landé-g factor of 1.048 [Casini and Landi degl'Innocenti, 1994] and 1.4 [Kobanov et al., 2003], respectively and hence are useful to study the magnetic structure from the photosphere to chromosphere, apart from other physical parameters. Typical Stokes images observed around H α wavelength close to umbral region of a sunspot (NOAA 10940) are shown in Figure 4.1.

The photospheric magnetic fields are obtained by inverting the Stokes profiles of Fe I line using the standard inversion techniques discussed in chapter 3. But, the difficulty is how to reliably convert H α polarization signal into magnetic field. This is because inversion of H α Stokes profiles in the magnetized medium is not yet established. One of the reasons cited in the literature is the complexity in its height sensitivity to different physical parameters [Socas-Navarro and Uitenbroek, 2004]. On a positive note, Socas-Navarro and Uitenbroek [2004] have shown that H α Stokes-V/I profiles can be used to infer chromospheric LOS field strengths under weak-field-approximation (WFA) above the umbra. We took a step further to derive vector magnetic field above the active regions under WFA applied to Stokes profiles of H α. This was inspired by the fact that the variation of Stokes parameters as a function of wavelength within H α spectral range is typical of a Zeeman sensitive line with a reasonable signal (some places in the umbral region, the amplitudes of

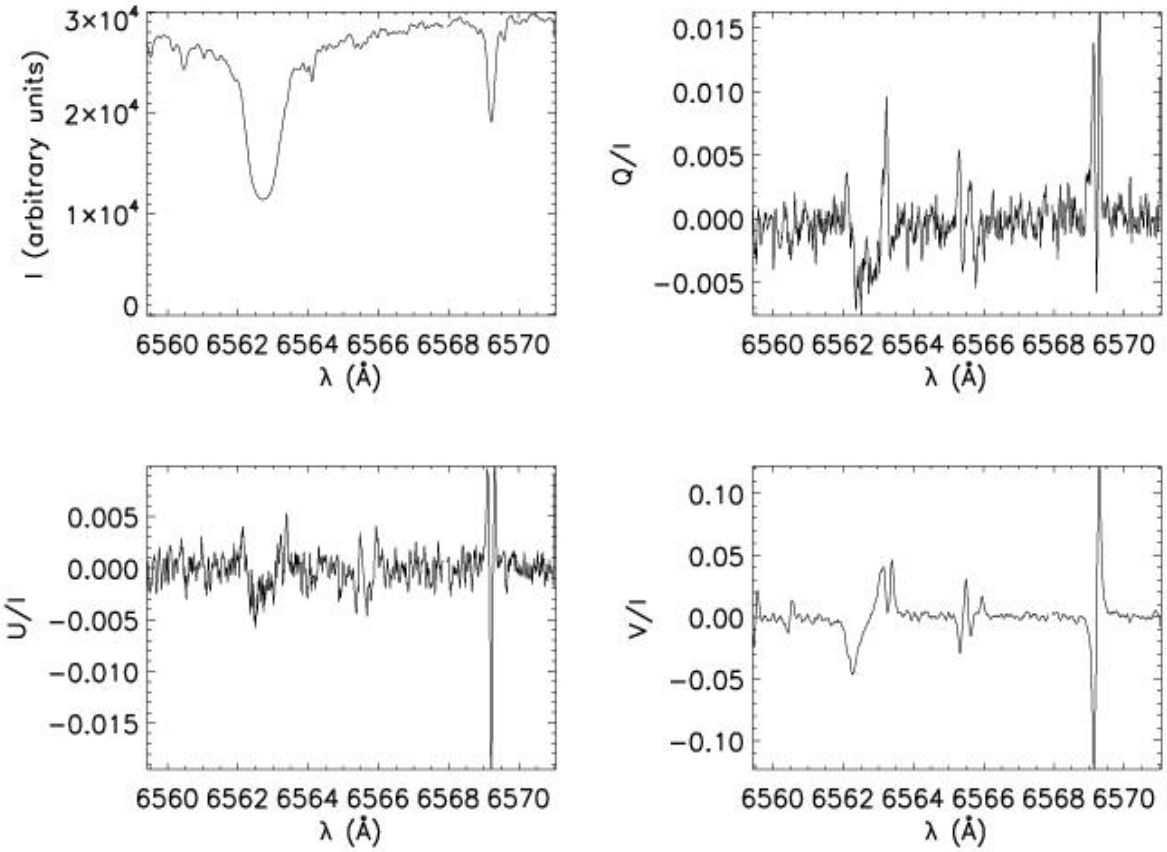

Figure 4.2: Typical Stokes profiles around H α obtained in the umbral region of active region NOAA 10940.

Stokes-Q, U are close to 1.5% with respect to local continuum). Figure 4.2 shows the Stokes profiles around H α spectral region. Notice from this figure that the H α Stokes profiles are similar to those of Fe I line, of course, with smaller amplitudes. More striking difference is that red wing of H α is intruded by a Zeeman sensitive Co I line at λ6563.4 [Moore et al., 1966] where as Fe I line is free from blending of any other line.

We discuss in this chapter the magnetic structure above three active regions viz. NOAA 10875 (AR1) , 10940 (AR2) and 10941 (AR3) observed on 28 April 2006, 1 and 4 February 2007, respectively. All these three active regions exhibit different magnetic field distribution at the photosphere. AR3 is a relatively simple, round and isolated sunspot. AR2 comprises of a sunspot which is also a simple and round but, surrounded by opposite polarity activities. AR1 exhibit a next level of complication with 3-4 umbrae within a single penumbra but, with same polarity. In other words, the umbra of this sunspot possess 3-4 light bridges as revealed by high resolution observations with partially covered penumbra. Hence, the field topologies in the higher layers above these active regions are expected to be different from each other. This provides an opportunity to validate the vector magnetic field derived from H α Stokes profiles through inter-comparison of the field structure in the chromosphere above these active regions. Further, the vector magnetic field inferred through H α Stokes profiles are discussed in conjunction with the X-ray and extreme ultra-violet (EUV) intensity structures observed by *Hinode*/XRT and *SOHO*/EIT, respectively.

4.1 Magnetic Field Topology Above AR3

We discuss the magnetic structure above the active regions in an increasing order of complexity. First, we discuss the more simple active region, AR3, an isolated sunspot (Figure 4.3). The heliographic co-ordinates of this sunspot during the observations were 7^o south and 5.5^o west. Details on the observational setup, data reduction and

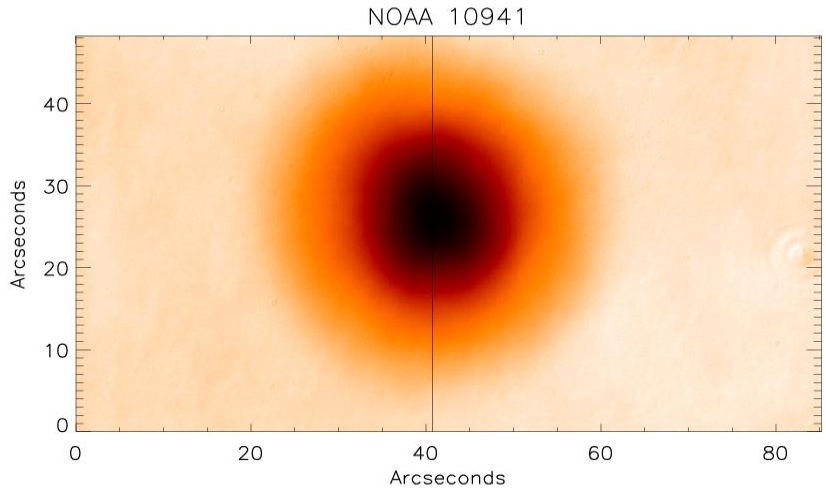

Figure 4.3: White light image of active region NOAA 10941. The origin of the axes in this image is arbitrary on the Sun.

analysis of the spectropolarimetric data can be found in chapter 3.

4.1.1 Photosphere

Variation of the magnetic field strength and its inclination is consistent with the well known magnetic field distribution at the photosphere, meaning, the field strength decreases uniformly in the radial direction from the center of the umbra towards the periphery of a visible sunspot (see a review by Solanki [2003]) and field inclination increases gradually along the radius of the sunspot. Plots of magnetic field strengths and inclinations along the slit, marked as vertical dark line in Figure 4.3, are shown

in Figure 4.4. The vertical lines in this figure correspond to the darkest spatial point along this radial cut. It is a well observed fact that the darkest region in the sunspot possess strongest field strength of the region. Indeed the field strength is strongest at this spatial location. This figure also confirms the earlier statement of decrease in field strength and increase in field inclination with radial distance from the umbra. But, the field strengths seem to increase in the region outside the sunspot close to quiet sun which however has large errors. Notice the smooth variation of field strengths and inclinations across the sunspot. The magnetic fields are oriented away from the LOS (usually known as negative polarity) as the field inclinations near central umbral region are close to 180^o. For the sake of comparing with other sunspots studied in this chapter which show opposite polarity to this sunspot, the inclination values were subtracted from 180^o.

4.1.2 Chromosphere

For comparison, the field strengths and inclinations inferred (using WFA) from H α Stokes profiles plotted across the sunspot are shown in Figure 4.5 for the same slit position as that in Figure 4.4. The field strength and inclination variations across the sunspot are similar to that of what is observed at the photosphere. However, they are less smooth.

Scatter plots of chromospheric and photospheric field strengths are shown in Fig-

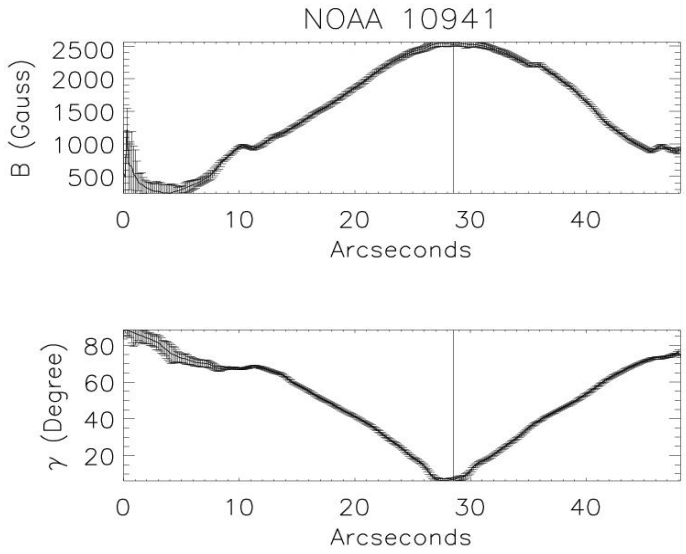

Figure 4.4: Plots of photospheric magnetic field strengths (top panel) and its LOS inclinations across the sunspot NOAA 10941. The radial slice considered is shown as dark vertical line on the sunspot image in Figure 4.3. The vertical lines drawn in this figure represent the darkest spatial point (which also correspond to the strongest field strength) along this radial cut.

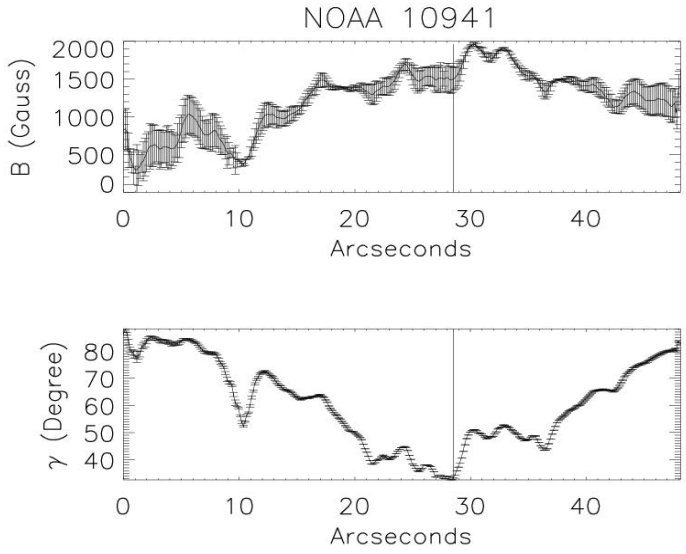

Figure 4.5: Same as Figure 4.4 but, values correspond to the chromosphere.

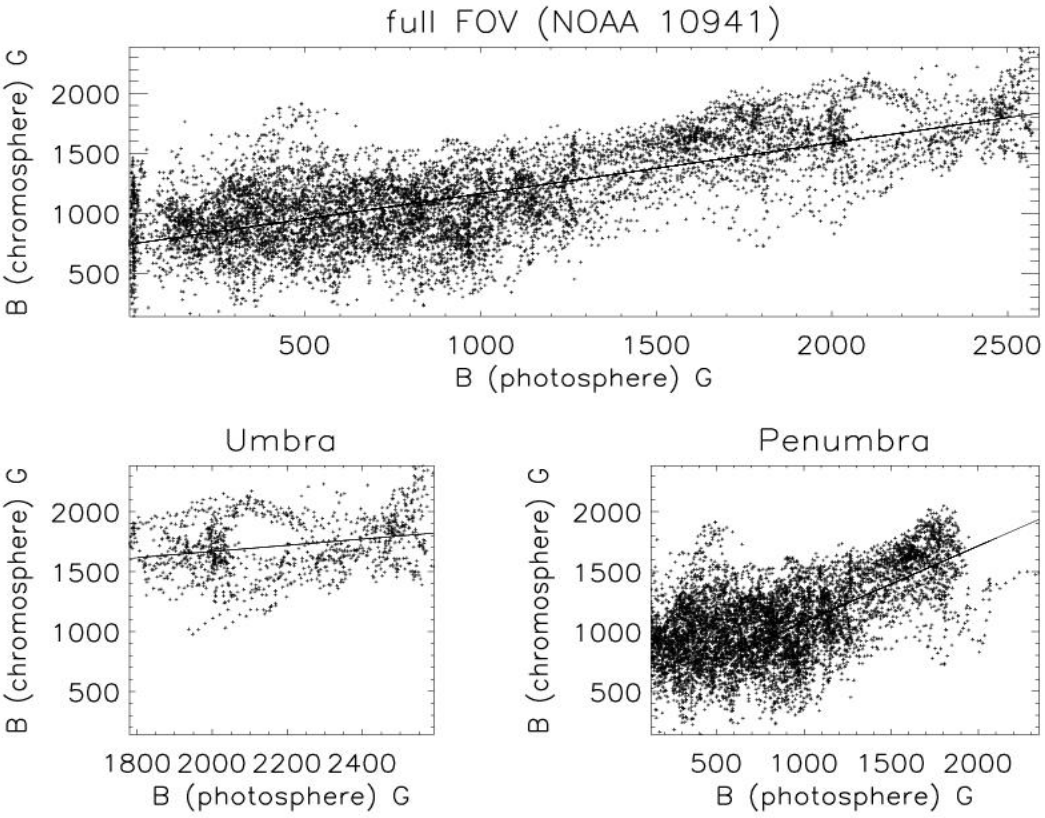

Figure 4.6: Plots of the chromospheric magnetic field strengths v/s the photospheric magnetic field strengths for AR3.Top panel is for the total FOV, bottom left panel is for the umbral region and right panel is for the penumbral region. Straight lines are the linear fit to the data points.

ure 4.6. These plots indicate that the magnetic field strengths at the chromosphere are weaker in general compared to their photospheric counterparts above this active region. The slope of the linear fit between the photospheric and chromospheric field strengths is 0.42 when all the data points are considered with an intercept of 740 G.

The scatter plot of chromospheric and photospheric umbral field strengths is shown on the bottom left panel of Figure 4.6. The linear fit for these data points results in a slope of 0.26 and the intercept is 1147 G. This figure indicates that the variation in chromospheric field strength above the umbra is more homogeneous compared to the photosphere. This homogeneity is also reflected in the plot of chromospheric and photospheric LOS field inclination angles shown on the bottom left panel of Figure 4.7 which shows smaller variation of the chromospheric umbral field inclination compared to their photospheric counterparts. The fields at the chromosphere are more horizontal as the field inclinations are larger compared to their photospheric counterparts. We noted earlier that the field strengths at the photosphere gradually decrease with sunspot radius and the field inclinations gradually increase.

The ratio of chromospheric to photospheric field strengths averaged over umbral region is 0.8 implying that chromospheric field strengths are weaker compared to their photospheric counterparts. Larger inclination and weaker field strengths of the chromospheric fields can be caused due to the divergence of the magnetic field with height. This is a natural consequence of fanning out of magnetic fields as

they propagate from high plasma β (ratio of gas to magnetic pressure) region, the photosphere, to low plasma β region, the chromosphere and corona [Gary, 2001]. The X-ray images of this active region also give a clue on the divergence of the magnetic field. A sample X-ray image of AR3 observed by *Hinode*/XRT [2] is shown in Figure 4.8. The contours overplotted in this figure are from the G-band observation of the same active region, observed simultaneously by *Hinode*/SOT. The plate scale of G-band image was matched with that of X-ray image plate scale before it was aligned with the later. If one assumes that the intensity structures observed in X-ray trace the magnetic fields, this figure clearly shows that AR3 harbour open magnetic field structures. That means the magnetic fields expand above this active region as they propagate upward and extend into interplanetary space, which is a typical case for an isolated sunspot.

The slope value of the linear fit between the penumbral chromospheric fields to the penumbral photospheric fields is 0.635 which is considerably larger compared to that of umbral region which is 0.26. This implies that the spatial variation in the penumbral chromospheric fields is larger compared to the chromospheric umbral fields. However the intercept of the linear fit is at 442 G which is a much smaller value than that of 1147 G obtained for the umbral field strengths. The ratio of the chromospheric to photospheric field strengths averaged over the penumbral region is 1.05. This implies that the chromospheric field strengths over the penumbral region are comparable to that of photospheric field strengths. This may be either

[2] see Appendix C for more details on *Hinode*/XRT

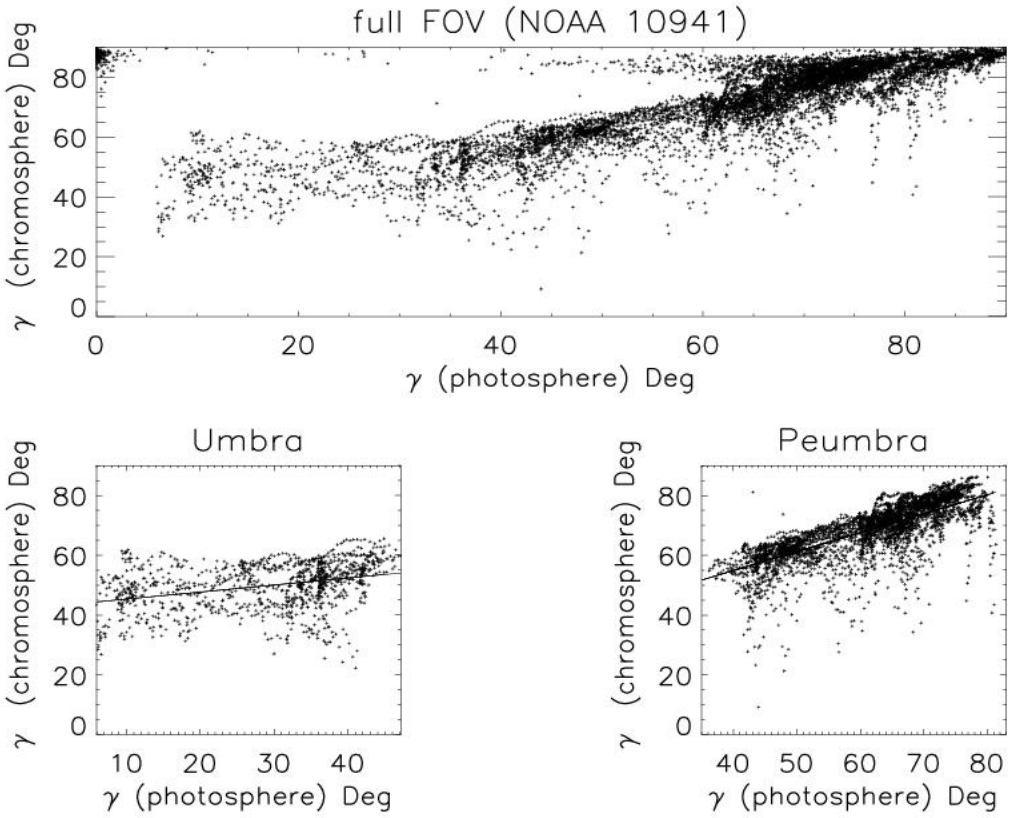

Figure 4.7: Scatter plot of the field inclinations at the chromosphere with respect to the field inclinations at the photosphere for AR3. Top panel is for the total FOV, bottom left panel is for the umbral region and bottom right panel is for the penumbral region. Straight lines are the linear fit to the data points.

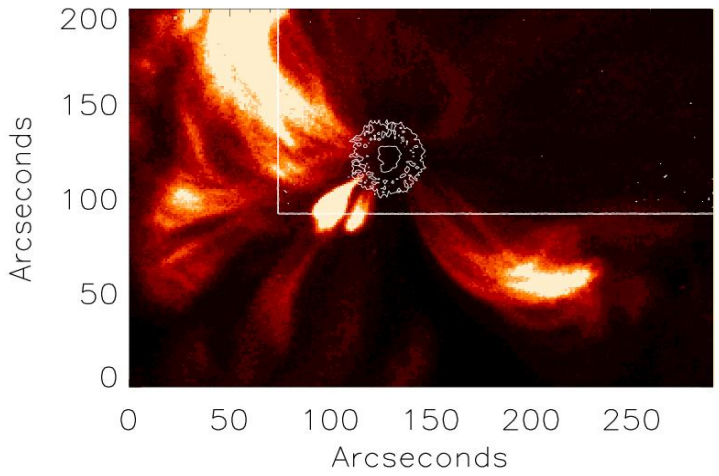

Figure 4.8: X-ray images of active region NOAA 10941 observed by *Hinode*/XRT on 4th February, 2007. The contours shown in this figure are the locations of the same active region at the photosphere observed in G-band wavelength by *Hinode*/SOT.

due to slower divergence of the penumbral fields compared to umbral fields or due to substantial contribution of the umbral fields which diverge with height and fill the region above the penumbra at the chromosphere or due to both. It is important to note that the identification of regions into umbra and penumbra are based on the intensity structures observed at the photosphere. A given magnetic region at the photosphere will be bigger in area at the higher heights because of the divergence of magnetic fields, clearly seen by the intensity images taken near the core of H α or X-ray images such as shown in Figure 4.8. Another important point to note here is the the larger inclinations of penumbral fields at the photosphere. The high spatial resolution observations have revealed that penumbra consists of bright and dark filaments whose field inclinations differ by 30 to 40^o with the dark filaments

inclined at larger angles compared to brighter filaments (see a recent review by Weiss [2006]). Hence, the probability of dark filaments reaching the heights of chromosphere and corona is less compared to the brighter filaments. Also, the field strengths of bright filaments are stronger compared to darker filaments [Langhans et al., 2005, Bellot Rubio et al., 2005]. However, because of their larger inclinations relative to umbral fields they can extend much beyond the visible sunspot at higher layers of the atmosphere and lie below the umbral fields, at least in the vicinity of sunspot. The penumbral fields that have reached chromospheric heights show larger inclinations as seen in Figure 4.7. This figure shows one-to-one correspondence between the penumbral field inclinations at the photosphere and chromosphere. This may not mean that, at a given location, the same field lines are observed at both the heights. Therefore, we believe that the intensity structures above AR3 observed in X-rays substantially contain umbral magnetic fields which expand as they propagate from photosphere to corona. Also, the field strengths inferred from H α in the penumbra have considerable contribution from the umbral fields. This may be the reason why the ratio of chromospheric to photospheric field strengths is larger in the penumbral region compared to umbral region.

4.2 Magnetic Field Topology Above AR2

The heliographic co-ordinates of AR2 during the observations were 4^o south and 10.5^o west. The seeing conditions were the best for this sunspot among the sunspots

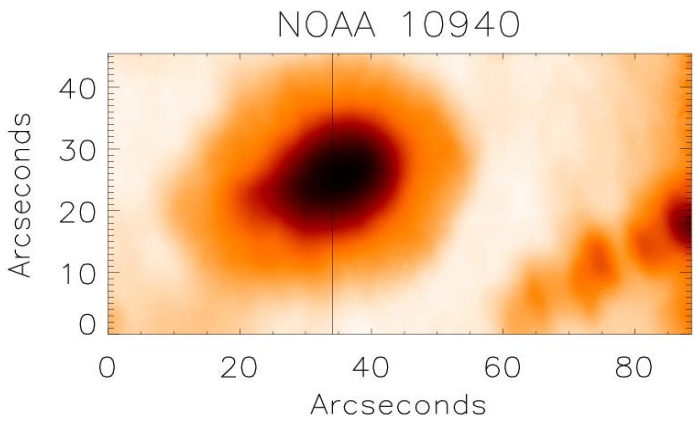

Figure 4.9: Broad band image of the active region NOAA 10940.

observations discussed in this thesis. However, as it was seen in chapter 3, the effective seeing limited spatial resolution is $\approx 5.5''$ for this sunspot which is considered to be low compared to the spatial resolution achieved world wide using modern techniques such as adaptive optics.

4.2.1 Photosphere

As noted earlier, this sunspot is also a relatively simple one but, surrounded by opposite polarity activity as seen in the bottom right corner of AR2 image shown in Figure 4.9. The nearby activity is quite strong reaching a field strength of 2300 G at the photosphere. In comparison, the main sunspot exhibit maximum field strength

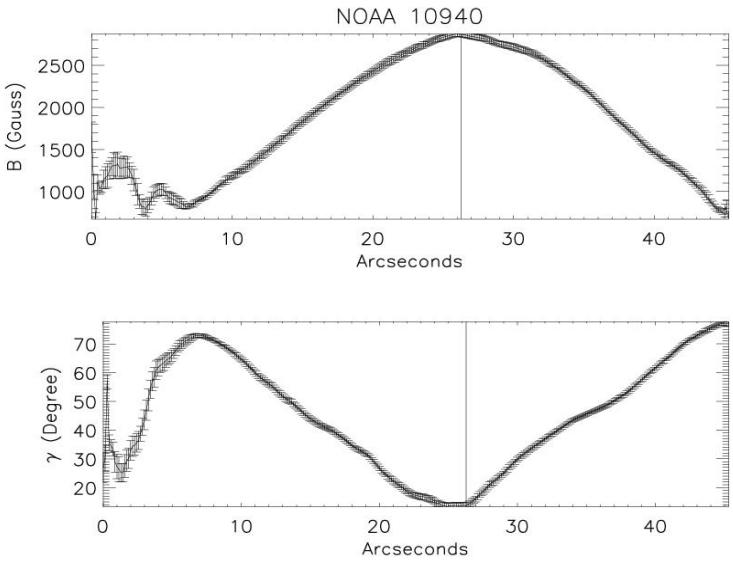

Figure 4.10: Plots of photospheric magnetic field strengths (top panel) and its LOS inclinations across the sunspot NOAA 10940. The radial slice considered is shown as dark vertical line on the sunspot image in Figure 4.9. The vertical lines drawn in this figure represent the darkest spatial point along this radial cut.

of 2900 G at the same height, for the spatial resolution of KTT observations. Also, at this height the field inclinations in the center of the umbra are close to 0^o and that of nearby activity are close to 160^o. This sunspot also exhibit field distribution typical of any other sunspot at the photosphere [Solanki, 2003]. A typical variation of field strengths and inclinations across this sunspot is shown in top and bottom panels of Figure 4.10, respectively. The vertical lines in these plots correspond to the darkest spatial location along the radial cut considered. These plots also include the quiet sun region in which the field distribution deviates considerably from that of sunspot. The radial cut considered to obtain this figure is marked as a dark vertical line on an image of this sunspot shown in Figure 4.9.

4.2.2 Chromosphere

Plots of chromospheric magnetic field strengths and its inclinations along the same radial slice are shown in Figure 4.11. Notice the striking difference in the variation of field strengths as well as the field inclinations in comparison with that of photospheric field distribution. The field strengths as well as the inclinations are larger in the umbral region. The inclinations of chromospheric umbral fields are comparable to that of penumbral field inclinations. In contrast to the chromospheric field distribution observed above AR3, there is a sharp variation of field strengths and field inclinations in the umbral region compared to the penumbral and quiet sun regions. These plots indicate that the magnetic field is more homogeneous above the

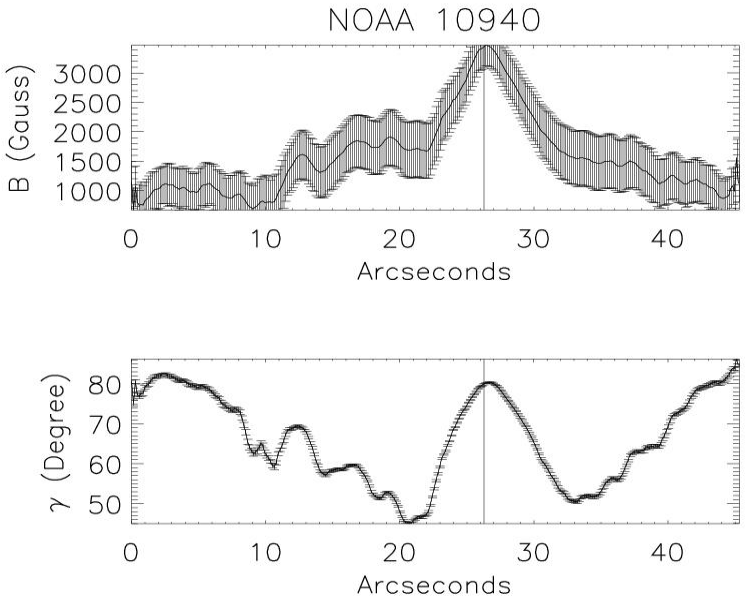

Figure 4.11: Same as Figure 4.10 but, for the chromospheric field strengths and inclinations.

penumbra and beyond.

Scatter plots of photospheric and chromospheric field strengths are shown in Figure 4.12. Top panel in this figure is for the total FOV, bottom left and right panels are for umbral and penumbral regions, respectively. This figure indicates that, in the strong field regions like umbra, the chromospheric field variation is much sharper than in the weaker field regions such as penumbra and quiet sun. In other words, the field is more homogeneous in the chromospheric penumbra than in the umbra which is exactly opposite to what was observed for AR3 (Figure 4.6). This is reflected in the slope of the linear fit between the chromospheric and photospheric umbral field strengths for this active region which is 1.8 and is very large compared

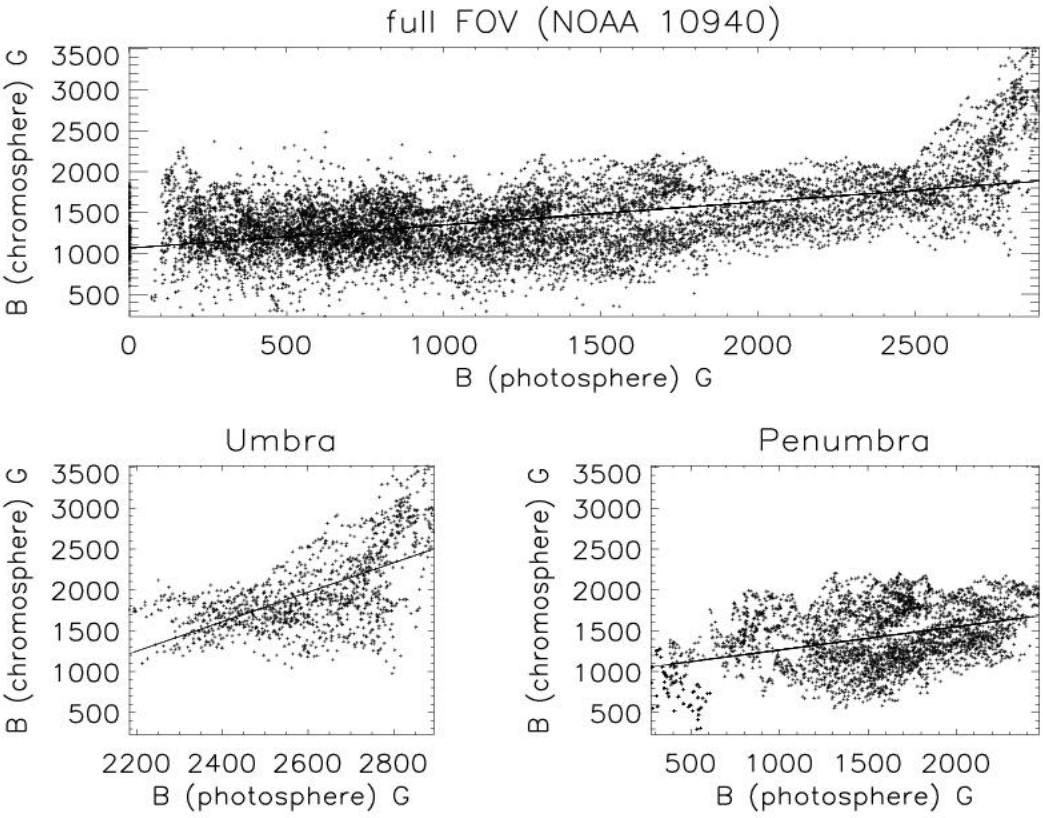

Figure 4.12: Same as Figure 4.6 but, for the active region NOAA 10940 (AR2).

to that of penumbral fields which is only 0.285. This implies that the chromospheric penumbral fields are more homogeneous than the chromospheric umbral fields.

The ratio of chromospheric to photospheric field strengths averaged over umbral and penumbral regions are 0.76 and 1.05, respectively. It is interesting to note that the ratio for penumbral fields is same as that of what was observed for AR3 and for umbral fields it is very close (for AR3 the ratio observed was 0.8). Even though, overall ratio of field strengths in the umbral region indicate that the field strengths in the umbral chromosphere are weaker compared to their photospheric counterparts, at the central umbra the field strengths are larger compared to the corresponding field strengths at the photosphere (bottom left panel of Figure 4.12). This higher field strengths in the central umbral chromosphere indicate larger concentration of magnetic fields in this region. Also, the chromospheric field inclinations in the central umbra are larger compared to their photospheric counter parts and their values are comparable to that of penumbral fields. This suggests that the fields in the central umbra have not spread out much, rather they are concentrated in a small region and are bent horizontally. Further, there is an evidence of these magnetic fields connecting to the nearby activity in X-ray images observed by *Hinode*/XRT. A sample X-ray image is shown in Figure 4.14 with the contour plots of G-band image of the same sunspot overplotted on it. The X-ray image shown in the bottom panel of this figure is same as that of the image shown in the top panel but with artificially enhancing the X-ray intensities in the umbral region to bring out the X-ray structures (seen as a rectangular box with the diagonal corners at (150,0) and

(200,50)). This picture represents a typical dipole sunspot region with magnetic field connecting from one region to another. In this active region, one polarity (positive) region is a single fully developed sunspot where as the other polarity (negative) region is fragmented smaller activities with and without partially/fully developed penumbra. As one moves from the central umbra, the magnetic fields become more vertical with sharp decrease in their strengths (see Figure 4.11). This indicate the arcade structures for the magnetic field above this spot which is clearly seen in the bottom panel of Figure 4.14. For comparison we recall that the field structure above AR3 resembles more of fountain like structure. Simultaneous imaging in H α will give much clearer picture about the structuring of the magnetic field, which is yet to be achieved at KTT. Also, the coarser step sizes used for scanning the sunspot ($\approx 2''$) does not allow us to recognize the fine structures that could have been seen otherwise. However, the X-ray images of the same active region clearly show closed loop structures connecting the main sunspot and the nearby activity (Figure 4.14).

The scatter plot between the chromospheric and photospheric penumbral field strengths shown in the bottom right panel of Figure 4.12 suggest that the fields are more homogeneous in the penumbral chromosphere than in the umbral chromosphere. The magnetic structure in the penumbral region above this active region is similar to that of AR3 but, more homogeneous.

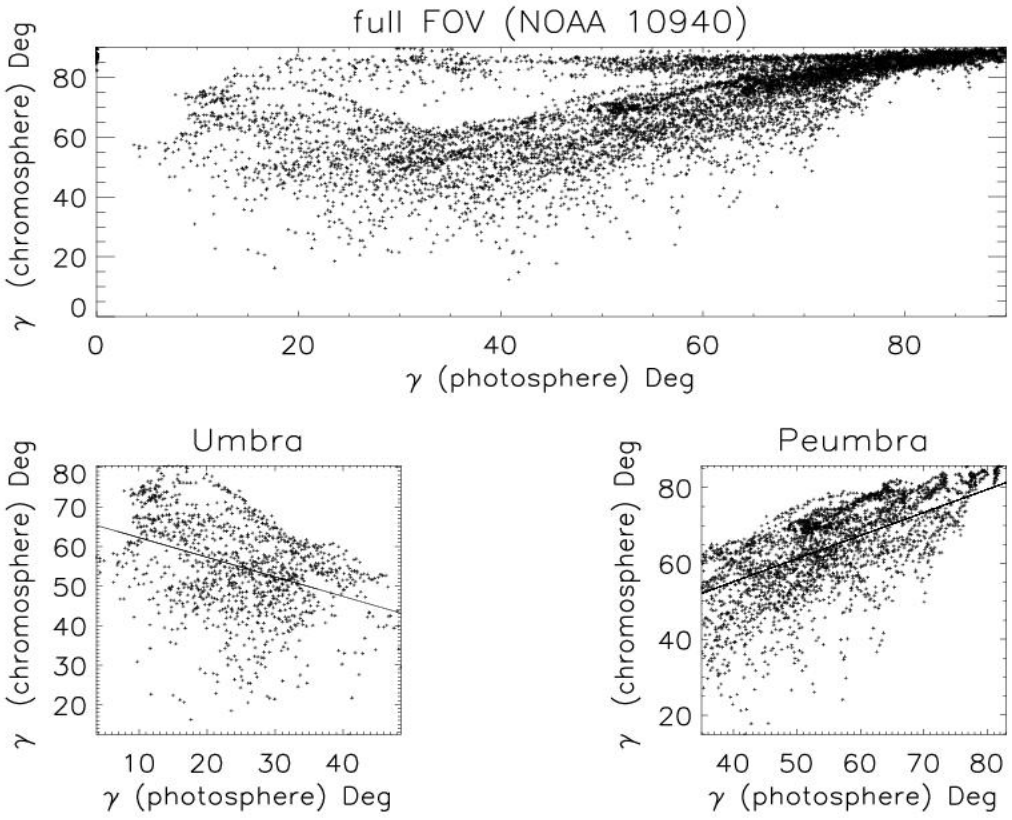

Figure 4.13: Same as Figure 4.7 but, for the active region NOAA 10940 (AR2).

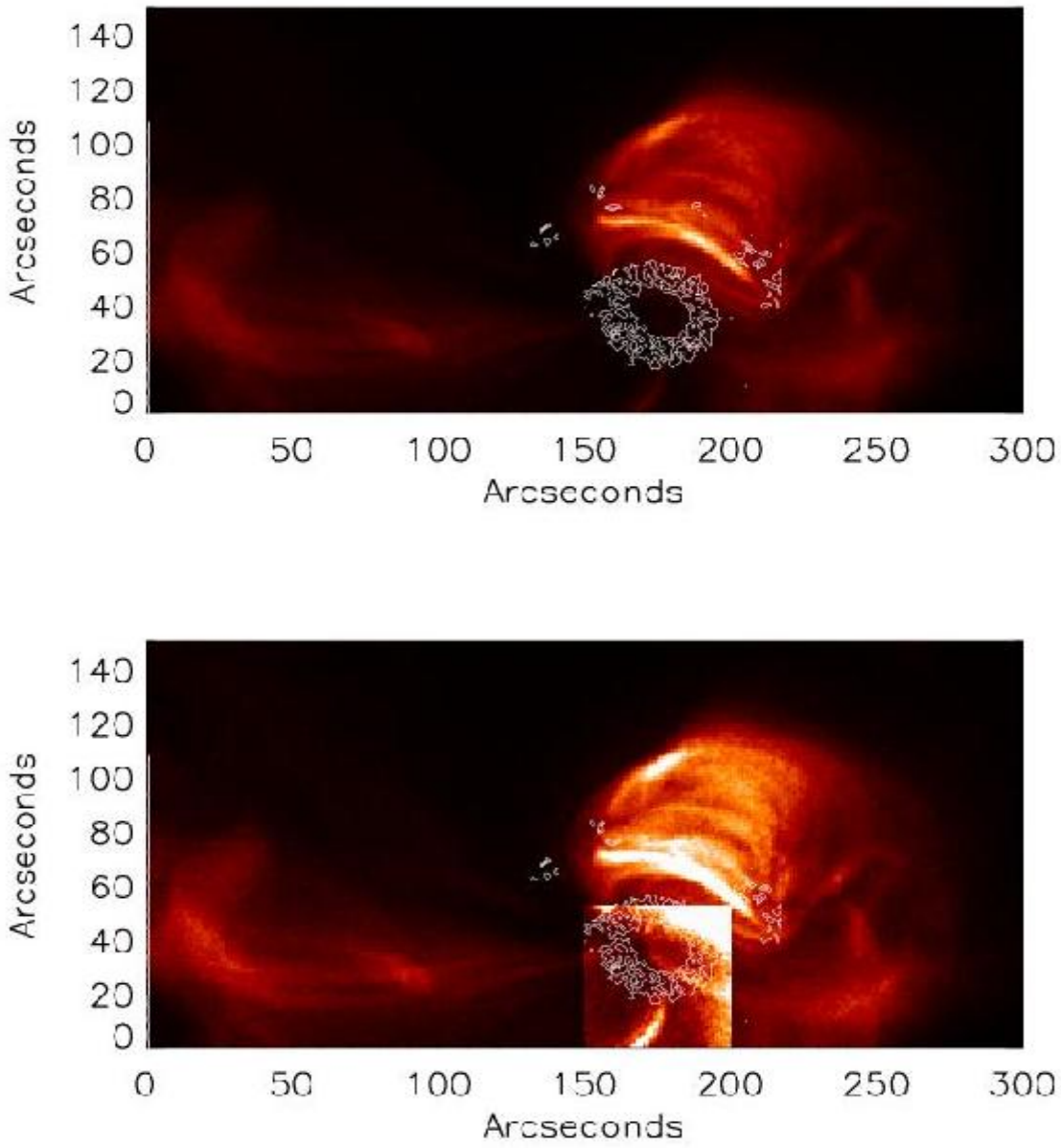

Figure 4.14: X-ray images of active region NOAA 10940 observed by *Hinode*/XRT on 1st February, 2007. The contours shown in these figures are the locations of the active regions at the photosphere observed in G-band wavelength by *Hinode*/SOT. The image shown in the bottom panel is same as that of what is shown in the top panel but, with artificially enhanced intensities over a rectangular box around the umbra to bring out the fine structures at this region.

4.3 Magnetic Field Topology Above AR1

This active region is slightly more complicated compared to the regions discussed in the previous sections. High resolution images of this active region revealed that this sunspot comprises of quite a number of light bridges which break the umbral region into several umbrae. Even the moderate resolution image obtained by *SOHO*/MDI shown in Figure 4.15 reveals four clearly visible umbrae within a single penumbra. Also the penumbral distribution is quite random. The heliographic coordinates of this sunspot were 11^o south and 18^o west during the observations.

The following discussions on the magnetic structure above this active region are based on the LOS field strengths due to the non-availability of the chromospheric vector magnetic field. This is because, H α Stokes-Q & U profiles are hardly discernible in this active region. In the following section, possible causes for this weak signals in Stokes-Q & U are discussed. The LOS field strengths are derived using COG method discussed in chapter 3. There is no inconsistency between the methods, WFA, used in the case of AR2 & AR3, and COG used for AR1, as LOS field strengths obtained through these two methods are not different from each other (see for details a comparison of these two methods in a paper by Cauzzi et al. [1993]).

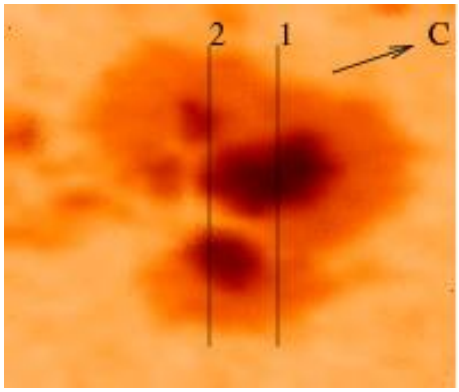

Figure 4.15: White light image of active region NOAA 10875 observed by *SOHO*/MDI on 28 April 2006. The arrow on the sunspot image indicates the disk center direction.

4.3.1 Comparison of Photospheric and Chromospheric LOS Magnetic Fields

Plots of LOS field strengths across two radial slices (marked as 1 & 2 on the sunspot image in Figure 4.15) are shown in Figure 4.16. The dotted lines in this figure correspond to the chromospheric field strengths and dashed lines to the photospheric field strengths. From these plots it is clear that, stronger the LOS field at the photosphere weaker the LOS field at the chromosphere. This implies the quicker weakening of the umbral fields compared to the penumbral fields. The scatter plot of LOS chromospheric and photospheric field strengths shown in Figure 4.17 clearly indicates the quicker weakening of the stronger fields. Similar kind of observations were reported earlier by Balasubramaniam et al. [2004] using simultaneous observations in H α and Fe I line at λ6301.5 and Hanaoka [2005] who compared the LOS field measured in H α with the magnetograms of *SOHO*/MDI. It may appear natural to interpret this

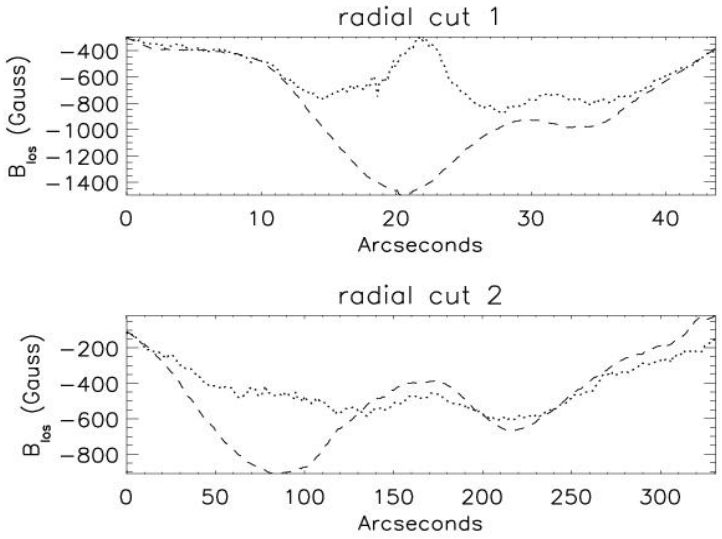

Figure 4.16: Plots of LOS magnetic field strengths at the photosphere (dashed lines) and the chromosphere (dotted lines) along two radial slices of the sunspot NOAA 10875. For reference, these two radial cuts are marked on the *SOHO*/MDI intensitygram shown in Figure 4.15.

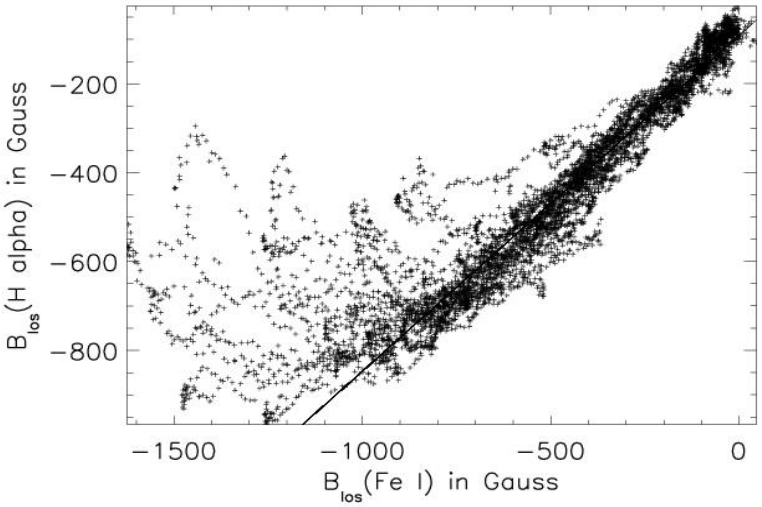

Figure 4.17: Scatter plot of photospheric and chromospheric LOS magnetic field derived using COG method applied to Fe I (λ6569) and H_α respectively. Solid line is a linear fit to the field strengths correspond to the penumbral region.

weaker LOS field strengths in the umbral chromosphere as due to larger inclination of the field lines at these heights similar to what is observed for AR2 (cf. Figure 4.13). The scatter plot of the LOS field strengths at the photosphere and chromosphere above the active region AR2 shown in Figure 4.18 also show similar kind of behaviour for the umbral chromospheric fields. But, the weaker or almost nill signal in H α Stokes-Q & U profiles in this active region would prevent us from interpreting the weaker LOS field strengths observed are due to larger field inclinations. This could have been caused by the actual weakening of the magnetic field strength itself. This is possible if the umbral fields diverge faster than the penumbral fields. This is a feasible scenario as the umbral fields spread out with height typical of isolated sunspots, similar to what is observed for AR3. However, it is not as obvious as seen in the X-ray images of AR3 which clearly indicate the fanning out of magnetic fields in the corona. The *SOHO*/EIT [3] images of this active region (Figure 4.19) show highly complicated structures in the higher layers. The *Hinode* was not launched at the time of this sunspot observations and hence we have used EUV images obtained by *SOHO*/EIT to understand the structuring of the magnetic field above AR1. Further, the stratification of the magnetic field above this active region are discussed in conjunction with the observed velocity structure in the next chapter (section 5.1).

[3] see Appendix C for more details

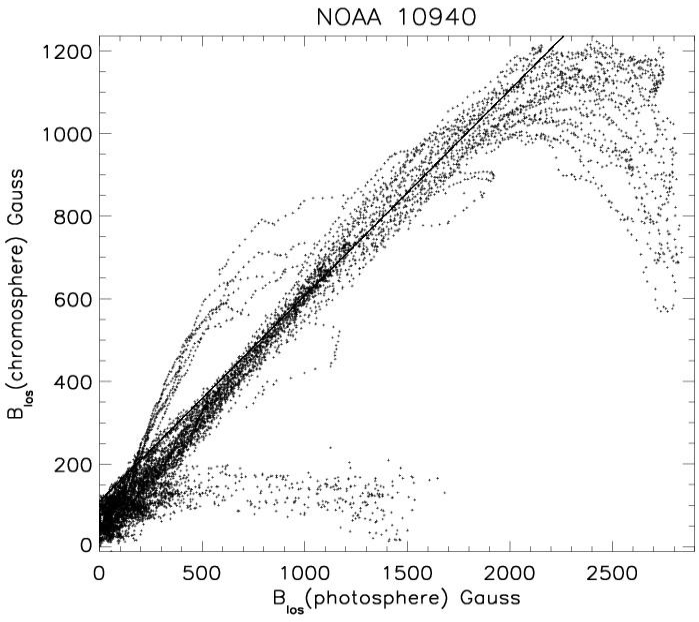

Figure 4.18: Scatter plot LOS magnetic field strengths at the photosphere and chromosphere for the active region NOAA 10940.

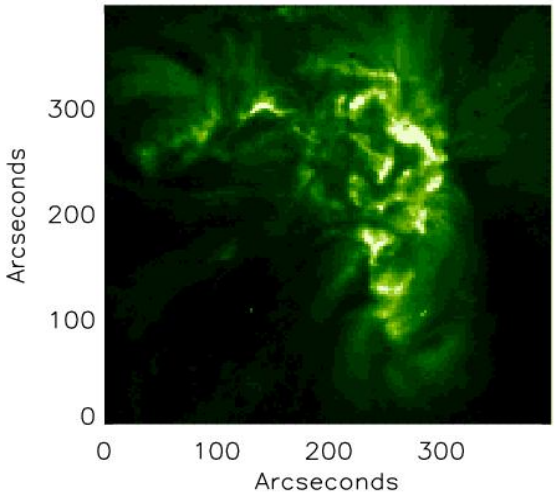

Figure 4.19: *SOHO*/EIT image of NOAA 10875.

4.4 Summary

We discussed in this chapter the stratification of the magnetic field above three active regions viz. NOAA 10875 (AR1), NOAA 10940 (AR2) and NOAA 10941 (AR3). For this purpose the spectropolarimetric data of these active regions obtained around H α spectral range are analyzed. The vector magnetic fields at the photosphere are obtained by inverting the Fe I Stokes profiles by assuming Milne-Eddington atmosphere under LTE conditions. At the chromosphere they are derived using WFA method applied to H α Stokes profiles. The structuring of the magnetic field above the active regions AR2 and AR3 are consistent with the X-ray structures observed in corona. The magnetic field topology above AR3 resembles fountain like structure which is typical of an isolated sunspot. On the other hand AR2 exhibit closed loop structures with one of their foot points located in the main sunspot and another in the nearby opposite polarity activity. For AR1, it was observed that the LOS field strengths weaken much faster in the umbral chromosphere than in the penumbral chromosphere. This can be caused either due to the quicker weakening of the overall magnetic field strength in the umbral region compared to penumbral region or due to the quicker bending of the umbral fields. Absence of discernible H α Stokes-Q and U in the umbral region suggest that the field inclinations are smaller. Hence, the quicker weakening of the LOS field strengths in the umbral chromosphere may be due to the actual weakening of the total field strengths. This is possible if the umbral fields diverge faster compared to penumbral fields. However, it is not apparent in the EUV images of this active region. EUV images show more complicated structure

above this sunspot. More details on the magnetic structure above AR1 are discussed from the point of view of the velocity stratification.

Chapter 5

Velocity Stratification from Photosphere to Chromosphere Above Active Regions

One of the most conspicuous properties of sunspots is the Evershed flow discovered in 1908 by Evershed using a spectrograph at Kodaikanal [Evershed, 1909], which has been denying a consistent explanation inspite of a considerable amount of research devoted to explaining it (cf. chapter 1). Evershed effect is a radial outflow of the material in the penumbral region at the photosphere and radial inflow at the chromosphere. After geometrical considerations, the Evershed velocities are known to be directed almost parallel to the solar surface and increase outward across the

penumbra to end abruptly at the visible limit of the spot. This abrupt disappearance already noted by Evershed at the time has posed a serious problem of mass conservation. In recent years evidence has accumulated that vertical return flow components are also indirectly identified which potentially solve the problem of mass conservation of the Evershed flow [Rimmele, 1995, Westendorp Plaza et al., 1997, Schlichenmaier and Schmidt, 2000, Schmidt and Schlichenmaier, 2000, Westendorp Plaza et al., 2001a,b, del Toro Iniesta et al., 2001, Bellot Rubio et al., 2003, Tritschler et al., 2004, Schlichenmaier et al., 2004, Bellot Rubio et al., 2006, Jurčák and Bellot Rubio, 2008, Beck, 2008]. In particular, downflows in deep photospheric layers of the outer penumbra have been detected, which at least qualitatively explain the abrupt stop of the Evershed flow at the outer penumbral boundary. However, whether these downflows are the return Evershed flows or not is yet to be verified. Nevertheless, at the chromosphere the velocity is maximum at the outer boundary of the penumbra and decreases rapidly with the distance away from the outer penumbral boundary (for eg. Georgakilas et al. [2003]).

There seems to be a correlation between the magnetic field and the Evershed flow. High resolution observations have revealed that the Evershed flows are confined to darker filaments of the penumbra (see a recent review by Weiss [2006]). These dark filaments exhibit systematically weaker field strengths than the surrounding medium [Bellot Rubio et al., 2005]. These intricate observational details are yet to find satisfactory explanation [Weiss, 2006]. The point to note here is that the plasma motion and magnetic field are intimately connected in the solar atmosphere and

influence one another. Hence, in the wake of difficulties in interpreting the magnetic field measurements in the higher layers, study of plasma motion along with the magnetic field will help in interpreting the observations (see for eg. Nagaraju et al. [2008a]). In this chapter we explore the possibility of using velocity measurements to understand the magnetic field or vice versa inferred through H α spectropolarimetry. The active regions considered in this chapter are the same as those in the previous chapter viz., NOAA 10875 (AR1), NOAA 10940 (AR2) and NOAA 10941 (AR3) and in which the magnetic field stratification is discussed.

5.1 Velocity Stratification Above AR1

5.1.1 Velocity

Velocities are estimated using the COG method described in chapter 3. The velocities thus obtained are more or less consistent with the well known Evershed flows [Evershed, 1909] at the photosphere and inverse Evershed flows at the chromosphere. Velocity maps of this active region at the photosphere and chromosphere are shown in Figure 5.1 on left and right panels, respectively. The COG wavelength positions of the Stokes-I profiles of central umbral region are considered as reference for calculating the Doppler shifts. The color bars above each map gives the correspondence between the colors and the magnitude of the LOS velocities. The

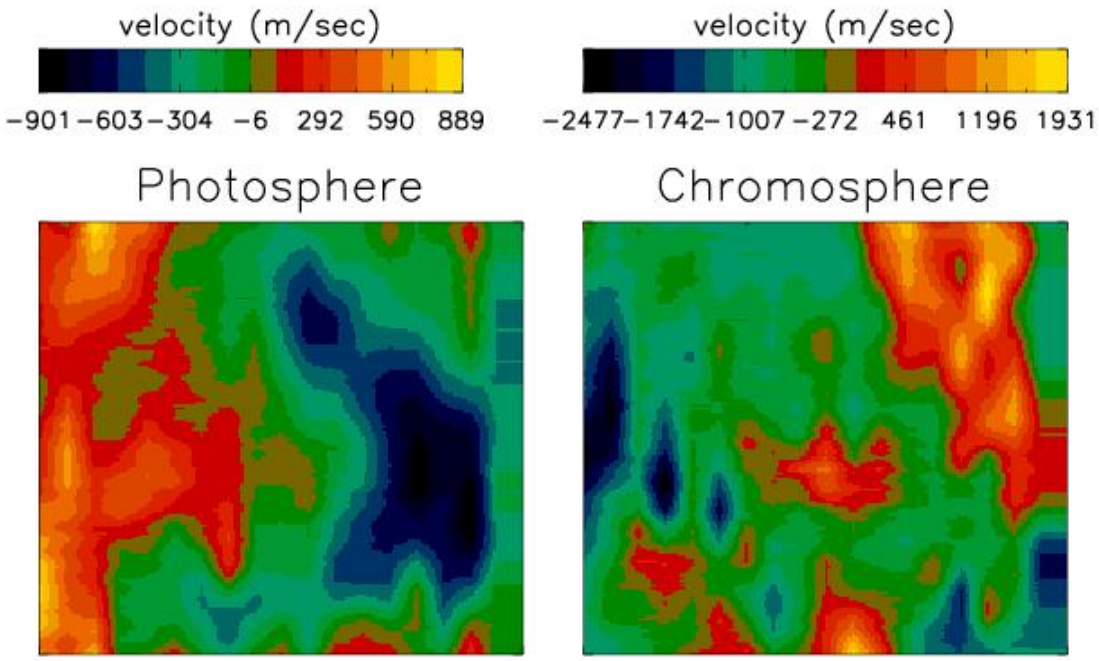

Figure 5.1: Velocity maps of active region NOAA 10875 at the photosphere (left panel) and chromosphere. The color bars on top of each map indicate the magnitude of LOS velocities in m/sec. Negative values correspond to the flows towards the observer and positive values correspond to the flows away from the observer.

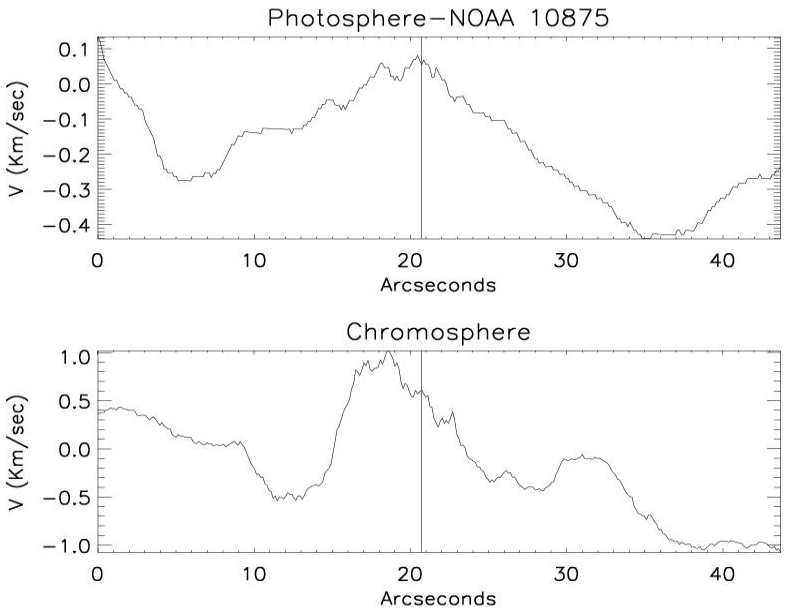

Figure 5.2: Variation of velocity across the sunspot (NOAA 10940) along the vertical line marked as 1 on the *SOHO*/MDI image shown in Figure 4.15.

negative LOS velocities correspond to the flows towards the observer and positive LOS velocities correspond to the flows away from the observer. Notice in this figure that the major portion of the center side penumbra shows upflows and limb side penumbra shows downflows at the photosphere consistent with the Evershed effect (Figure 4.15). On the other hand, at the chromosphere, the center side and limb side penumbra harbour downflows and upflows respectively which is consistent with the inverse Evershed effect. However, at few locations, photospheric and chromospheric flows in the same direction are also observed. For one-to-one comparison of the photospheric and chromospheric LOS velocity variation across the sunspot, plots of velocities along the radial cut 1 shown in Figure 4.15 at the photosphere (top panel) and chromosphere (bottom panel) are shown in Figure 5.2. This plot

shows that the flows at the photospheric and chromospheric heights are not always in the opposite direction, for this spot, even though major portion of the sunspot exhibit Evershed and inverse Evershed flows at the photosphere and chromosphere, respectively. The LOS velocity increases towards the periphery of the sunspot at both the heights in confirmation with the earlier observations which is well known since the time of discovery of the Evershed effect (see a review by Solanki [2003]).

5.1.2 Velocity Gradients

The bisector technique discussed in chapter 3 has been used to derive the velocity gradients in the solar atmosphere. The velocity difference defined in Eq. 3.13 can be considered as velocity gradient over the line formation height for the respective spectral line. For bisector analysis, the Fe I line at λ6569 and H α are separately considered. The velocity gradients obtained through bisector technique applied to Fe I line represent velocity gradients at the photosphere and from H α we get the velocity gradients at the chromosphere. The plots of photospheric velocity gradients as a function of photospheric magnetic field strengths are shown in Figure 5.3. Top panel in this figure is for all the points over the total FOV, where as the bottom left and right panels are for the umbral and penumbral regions of AR1, respectively. Note from this figure that the large number of points in the umbra have smaller velocity gradients than the penumbra. This is expected because, the magnetic fields are more or less vertical with respect to the surface normal with lesser gradient compared to

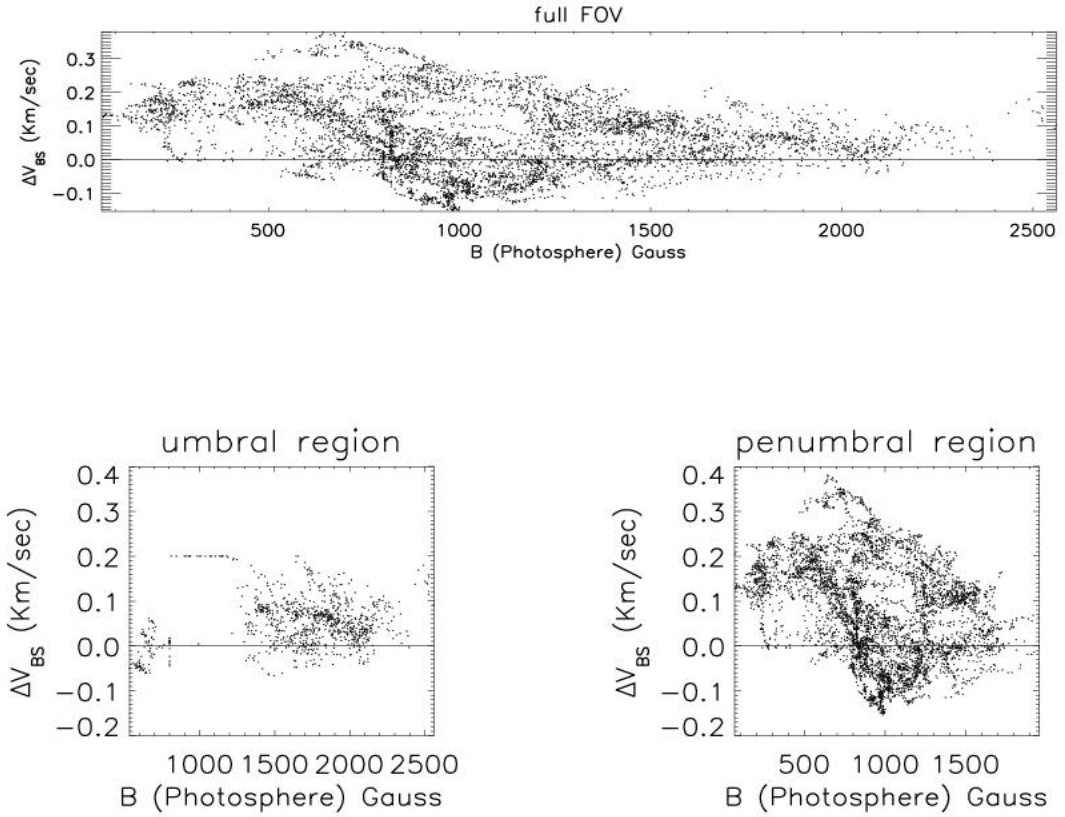

Figure 5.3: Plots of velocity gradients at the photosphere v/s the magnetic field strengths at the same height.

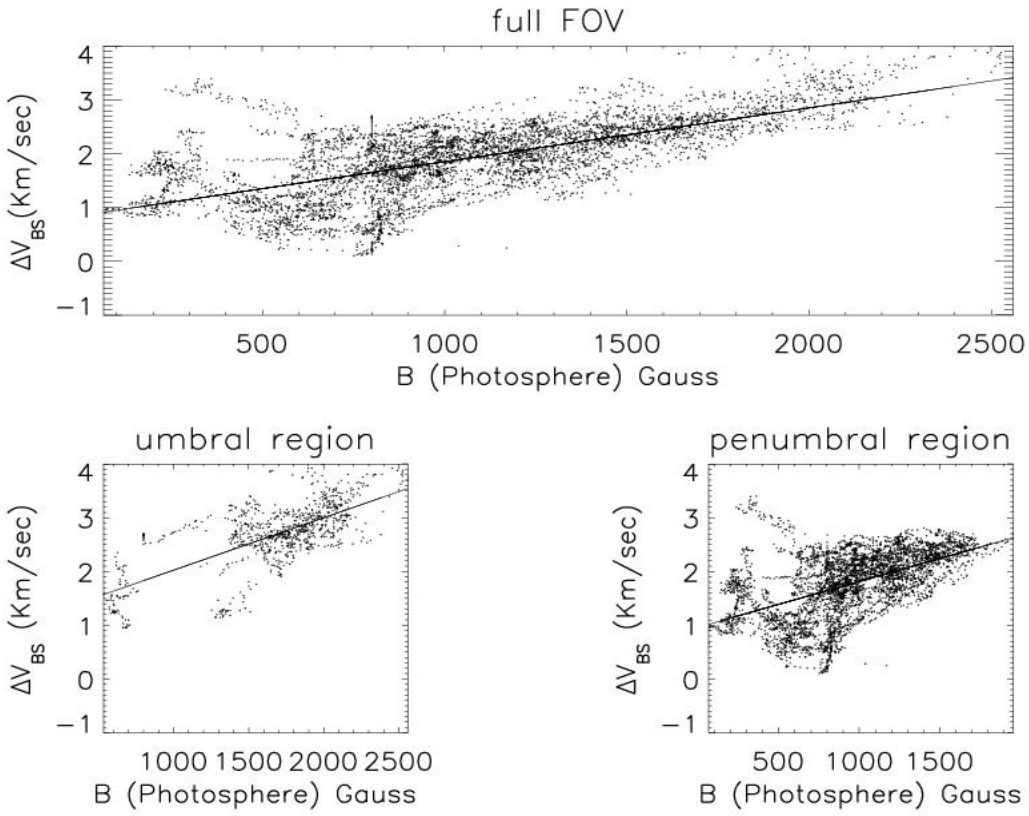

Figure 5.4: Plots of velocity gradients at chromosphere derived using H α with the bisectors considered for the full line profile v/s the total field strengths (photospheric). Solid lines are the linear fit to the data points.

the highly structured penumbra. The velocity gradients at the field strengths in the range 500-1500 G shown in Figure 5.3, representing the penumbral region, are 2-3 fold larger compared to the other regions of the sunspot. Closer investigation of bisector velocity differences of Fe I line show the flow pattern consistent with the Evershed flow at the photosphere. That means, both line core and wing bisectors in limb side penumbra show redshifts with respect to central umbra and in disk center side penumbra they show blueshifts.

Figure 5.4 shows the plots of chromospheric velocity gradients v/s the photospheric magnetic field strengths. Top panel in this figure is for the total FOV and bottom left panel for umbral region and bottom right panel for penumbral region. Notice the increase in bisector velocity gradient inferred from H α profiles with increase in the photospheric magnetic field strength. To check the consistency of the variation, plots of velocity gradients along two radial slices of sunspot (marked as 1 and 2 in Figure 4.15) are shown in Figure 5.5. This figure also show that the larger velocity gradients at the chromosphere are located at the places where strong photospheric fields are observed. Top panels in Figure 5.5 show the plots of photospheric field strengths along the radial cut 1 (top left) and the radial cut 2 (top right). The corresponding plots of velocity gradients are shown in the bottom panels. Except at few locations (mostly in the limb side penumbra such as shown in the bottom right panel of Figure 5.4) which show less variation in the values of velocity gradients inspite of a variation in the photospheric field strengths (which is evident also in Figure 5.4), in most of the places the velocity gradients are larger where the photospheric

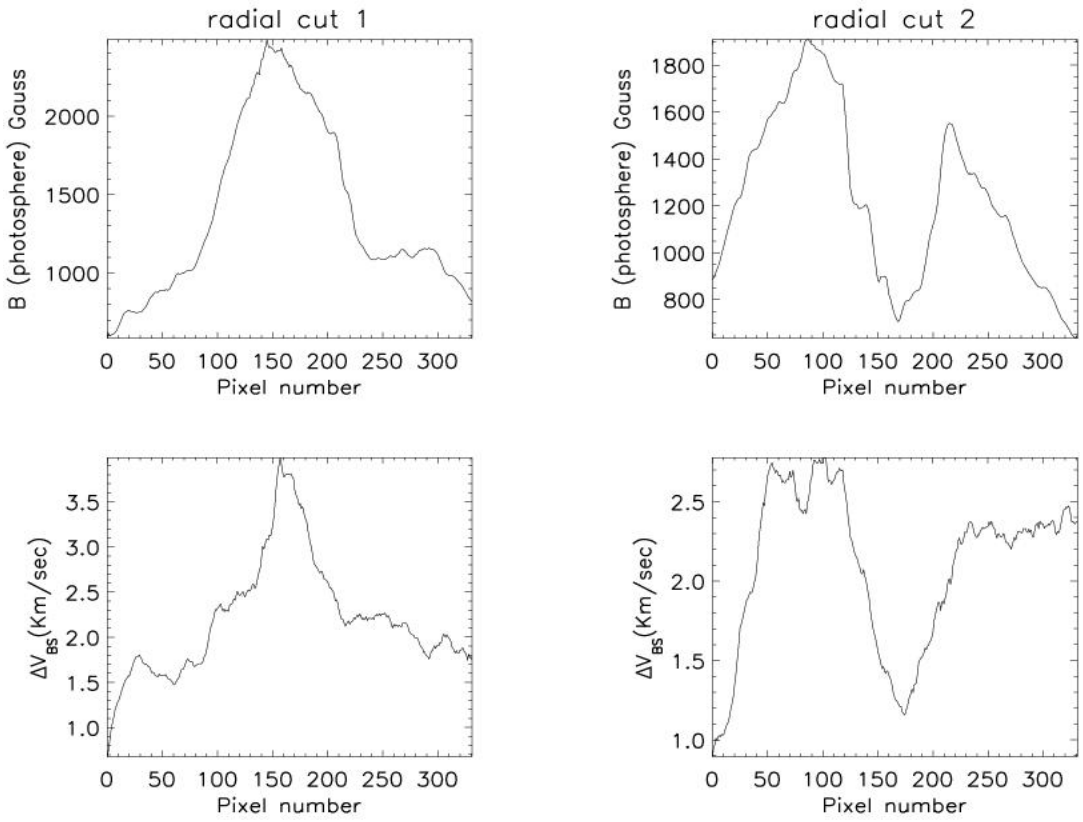

Figure 5.5: The top panels in this figure show the plots of magnetic field strength at the photosphere along two radial slices of the sunspot. The radial slices are same as those shown in Figure 4.15. The corresponding plots of velocity gradients at the chromosphere are shown in the bottom panels.

magnetic field strengths are larger.

Closer examination of the bisector wavelength positions of H α Stokes-I profiles in different regions of the sunspot with respect to the reference wavelength chosen at the central umbral region reveals the following results (see figure 5.6).

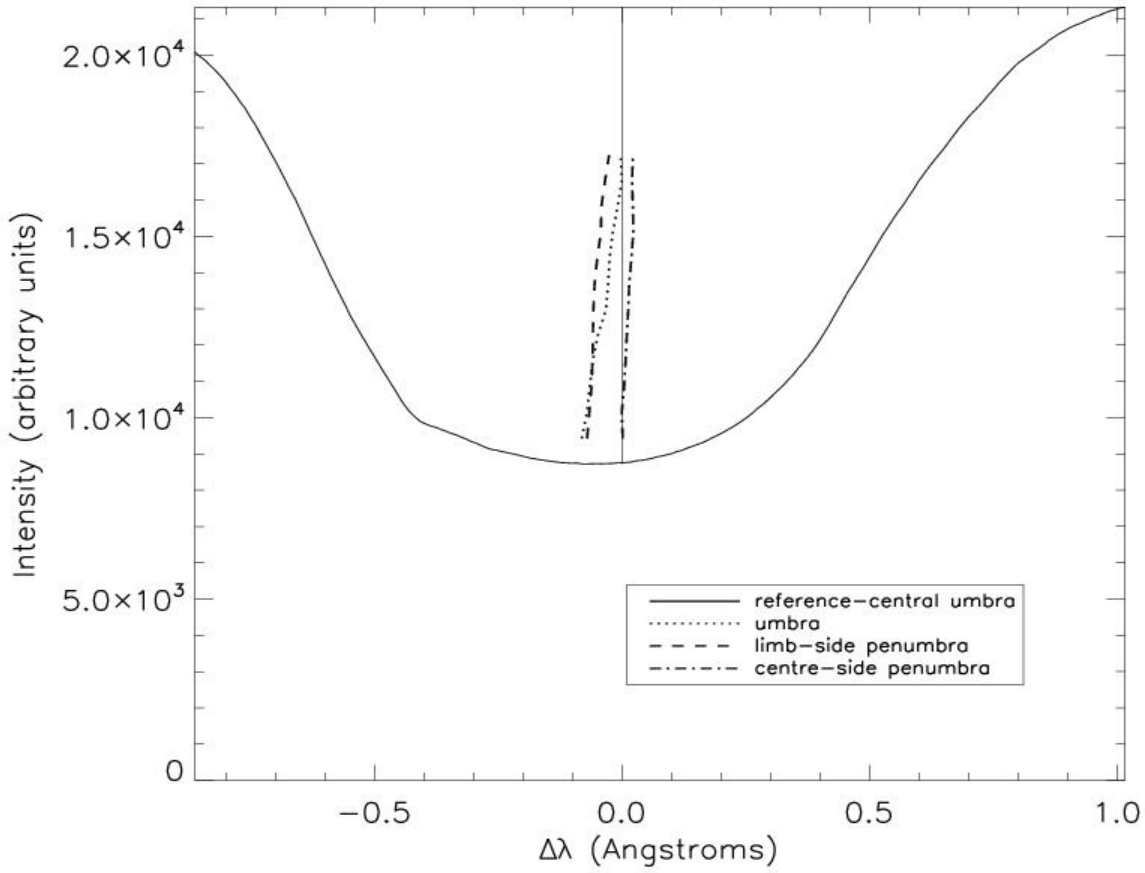

Figure 5.6: Representative bisectors of H α line profiles corresponding to different regions of the sunspot, plotted on an average quiet Sun profile. The solid line represents the reference wavelength (which is a COG wavelength position of the central umbral region). The dotted line represents the bisectors location typical of umbral profiles, the dashed line represents the limb side penumbra, and the dash-dotted line represents the center side penumbra.

- In the limb side penumbra both line core and wing bisectors show blue shifts with respect to central umbra. The shifts in the line core bisectors are large compared to the line wing bisectors indicating the net upflow.

- In the umbral region also both line core and wing bisectors show blue shift with respect to the reference wavelength. The shifts in the line core side bisectors for the umbra are almost comparable to that of the limb side penumbra. However, the shifts in the wing bisectors for the umbra are much smaller with respect to that of the limb side penumbra. This would indicate again the net upflows but with larger velocity gradients.

- In the center side penumbra the line wing bisectors show redshift in most of the places with respect to the quiet Sun. At few locations they show a small blue shift or no shift. The line core side bisectors show slight blue shift with respect to the quiet Sun reference wavelength position.

It is found through these analyses that the velocity gradients are larger in the umbra at the chromospheric heights compared to the penumbra (see Figure 5.4). This is exactly in contrast with the flow pattern observed at the photosphere (Figure 5.3). The analysis of bisector velocity differences also indicate accelerated upflows in the umbral region.

There is a little concern due to the residuals present after the Co I line blend from Hα is removed. To make sure that there are no artifacts introduced due to

the residuals, the bisector velocity differences calculated by considering the spectral region around the line core which is not affected by the blend are shown in Figure 5.7 as a function of photospheric field strength. This figure also shows the trend that the velocity gradients increase with increase in photospheric magnetic field strength confirming the observations made with the blend removed intensity profiles. As expected, the gradients are smaller due to the smaller spectral range considered in this case.

To summarize, wavelength shifts analysis of Stokes-I bisectors show that the velocity gradients are larger in the umbral region than in the penumbral region at the chromospheric heights. Most importantly, accelerated upflows are observed in the umbral region. In other words, LOS velocity increases upward more rapidly in the umbral region than in the penumbral region at the chromosphere.

It may appear obvious that the larger velocity gradients in the umbral chromosphere are caused due to the larger magnetic field gradients at these heights as it was seen in Figure 4.16. For this sunspot, the observed LOS field strengths decrease more rapidly above the umbral region than in the penumbral region. But, the question was whether the rapid decrease in LOS field strengths above the umbra is due to the actual weakening of the field strengths or due to the quicker bending of the umbral fields. The absence of discernible signal in H α Stokes-Q and U itself is an indication that, field inclinations are smaller. The magnetic stratification for this spot is unlike what is observed above the active region NOAA 10940 which also shows a similar

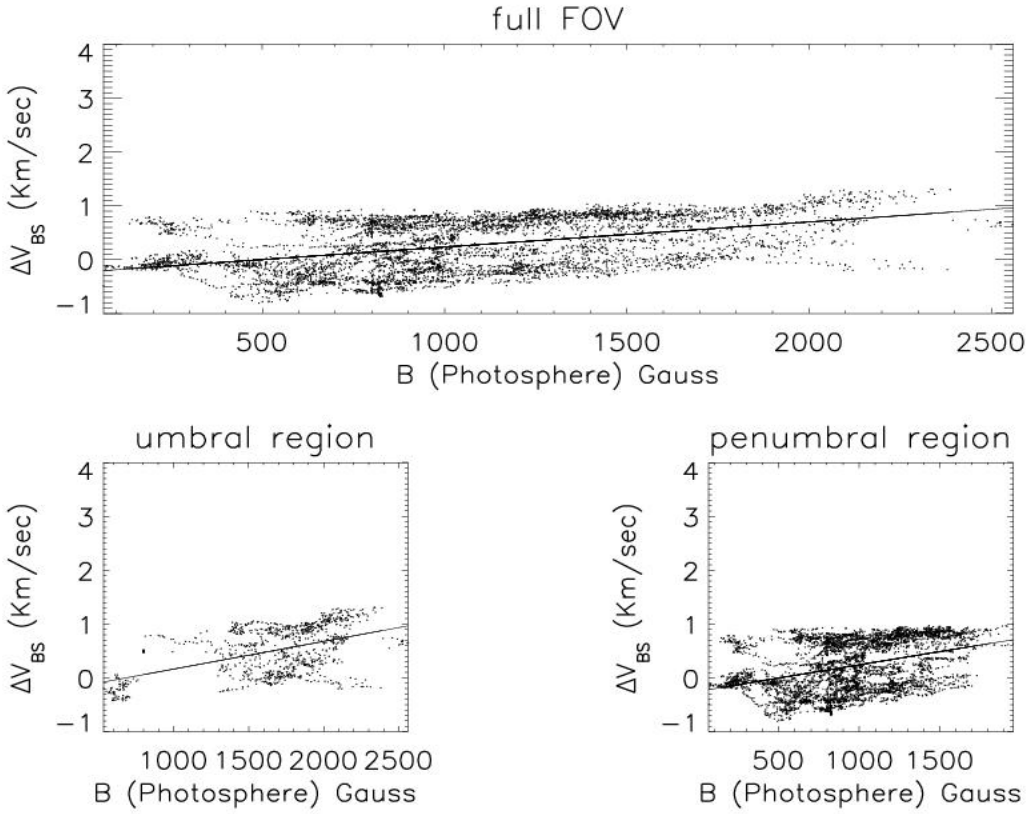

Figure 5.7: Same as Figure 5.4 but with the limited spectral range about the line core considered for calculating velocity gradients to avoid the influence of blending due to Co I line. The axes scales are kept same as Figure 5.4 to indicate that the velocity gradients are smaller compared to the case when the full Stokes-I profile is considered.

kind of behaviour in terms of LOS field strengths (Figure 4.18). But, a good linear polarization is observed in H α above this active region indicating that the field inclinations are larger (cf. Figure 4.13). Earlier observations by Gosain and Prasad Choudhary [2003] have also indicated the weakening of the LOS field strengths which is larger for stronger fields. In their observations quicker weakening of the stronger fields is not apparent, probably, because of the lines (Mg I b1 and b2 at λ5173 and λ5184) used to infer chromospheric magnetic field originate at the lower chromosphere. Balasubramaniam et al. [2004], based on simultaneous spectropolarimetric observations in H α and Fe I lines around λ6300, and Hanaoka [2005], comparing H α magnetograms with that of *SOHO*/MDI, have also reported the quicker weakening of the LOS field strengths. In all these works there was a doubt casted about the reality of such smaller LOS field strengths above the umbral chromosphere. They have proposed various possibilities which can cause this quicker weakening of the umbral fields. We have shown here that the observed weaker LOS field strengths in the umbral chromosphere are real, based on the studies of velocity gradients (see also Nagaraju et al. [2008a]). As it was seen, the velocity increases upward more rapidly above the umbra than in penumbra. This can be caused due to the quicker weakening of the field strength because the chromospheric plasma becomes less and less inhibited by the magnetic field implying the upflows with larger amplitude consistent with the velocity stratification discussed above. Hence, we believe that the quicker weakening of the LOS field strengths above this spot is due to the actual weakening of the total field strength. Weaker field strengths and smaller inclinations above the umbral region may imply that the stronger fields diverge faster as suggested by

Balasubramaniam et al. [2004].

The situation in penumbra is much more complicated even though the field strengths are comparable above this region and exhibit smaller velocity gradients. As discussed in chapter 4, only a small fraction of the penumbral field lines reach the height of chromosphere because of their larger inclinations at the photosphere. Then, in such a case the field gradients above the penumbra is expected to be more, and hence the velocity gradients. But, the bisector analysis shows that the velocity gradients are smaller in the penumbral chromosphere. The good correlation of field strengths at the photosphere and chromosphere can be due to the contribution of umbral fields to the observed penumbral fields, and hence the field strengths are comparable otherwise, it should have been much weaker because of the larger inclinations. But, the smaller velocity gradients observed in the penumbral chromosphere poses a difficulty in its explanation. It is obvious that H α will not be sampling the same field lines at all the heights over which it is formed. If H α samples those layers which have similar velocities then one can expect smaller velocity gradients above the penumbra. Many more studies are needed in order to understand the structuring of the plasma flow in the penumbral region.

5.1.3 Stokes V Amplitude Asymmetry

Observed area and amplitude asymmetries of Stokes profiles have been interpreted as due to the gradients in the physical parameters such as magnetic and velocity fields [Grigorjev and Katz, 1972, Illing et al., 1975]. Hence the analysis of Stokes-V amplitude asymmetry will help in verifying the interpretation of the results from bisector analysis of Stokes-I profiles in the previous section. From the close examination of Stokes V profiles of H α we found that the Co I line has not intruded up to the extent that the amplitudes are affected. Hence the results presented from H α based on amplitude asymmetry are reliable.

From Figure 5.8 it is clear that the amplitude asymmetry of Fe I line tends toward zero with increase in photospheric magnetic field strength. This means, at the photospheric heights the gradients are smaller in umbra which corresponds to the region of strong fields. In contrast amplitude asymmetry observed in H α tend to increase with photospheric field strength as shown in the Figure 5.9. This may imply that the velocity and magnetic field gradients are larger in the umbral chromosphere compared to umbral photosphere.

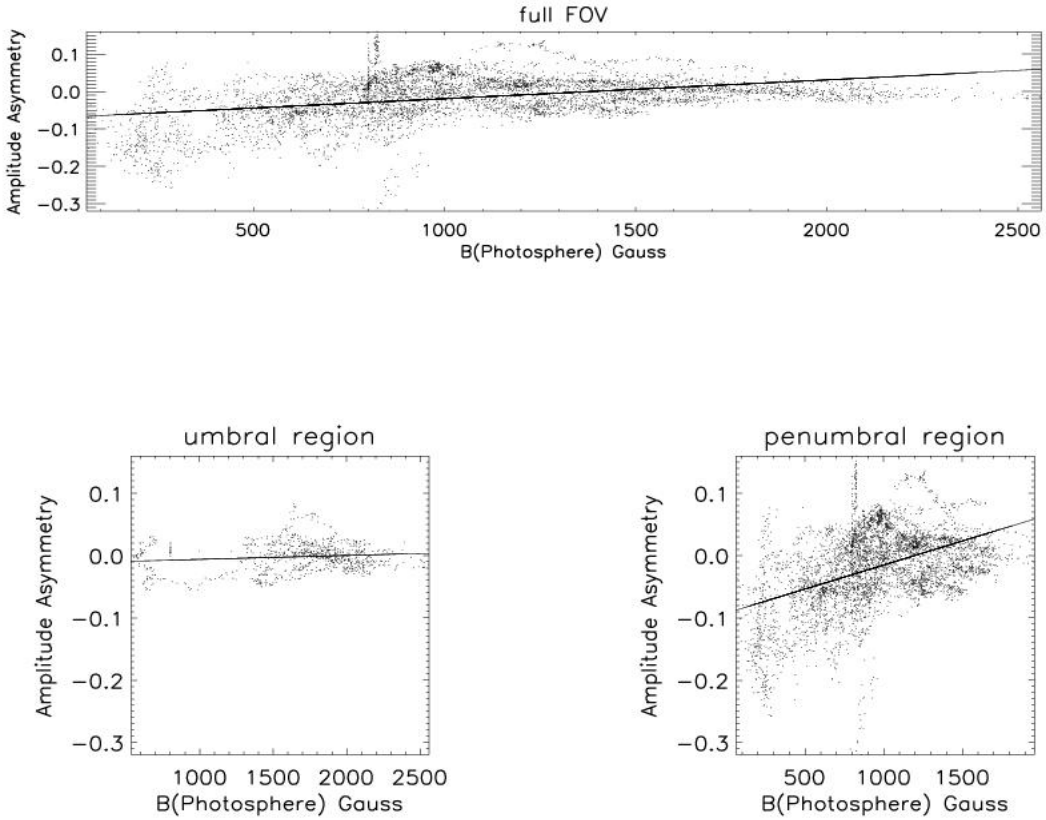

Figure 5.8: Plots of amplitude asymmetry of Stokes V profiles of Fe I line v/s the total field strengths (photospheric). The solid lines are the linear fits to the data points.

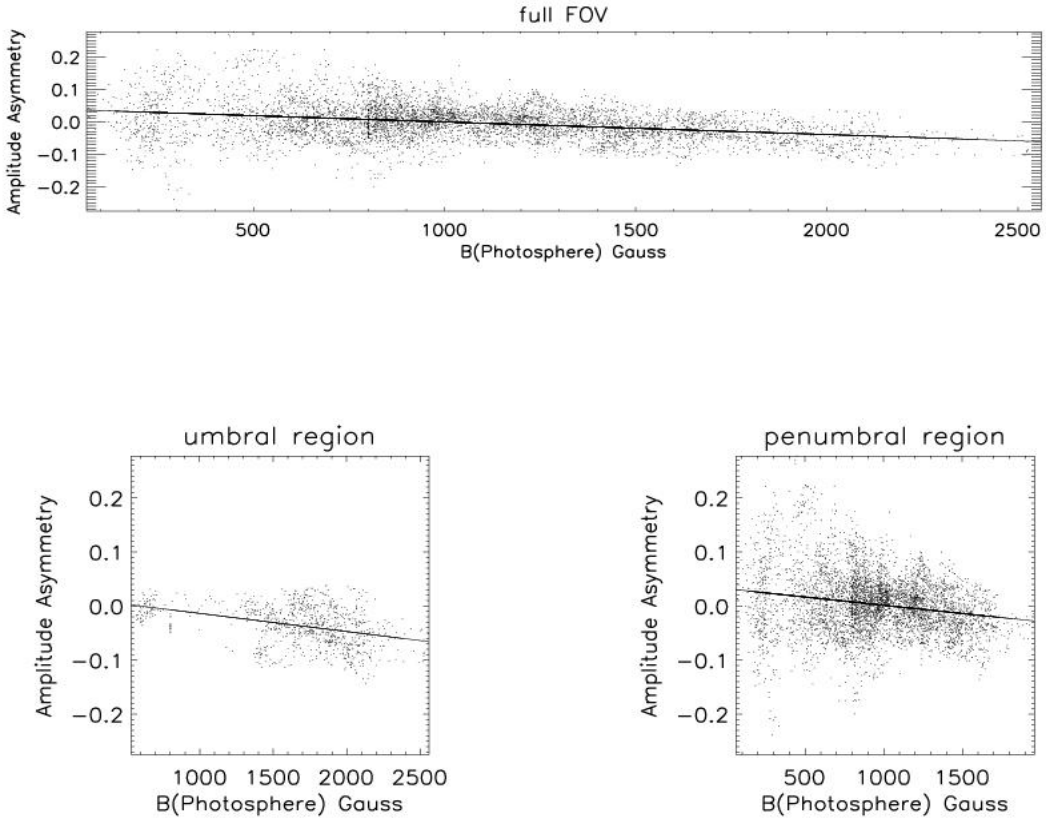

Figure 5.9: Plots of amplitude asymmetry of Stokes V profiles of H α line v/s the total field strength (photospheric). The solid lines are the linear fits to the data points.

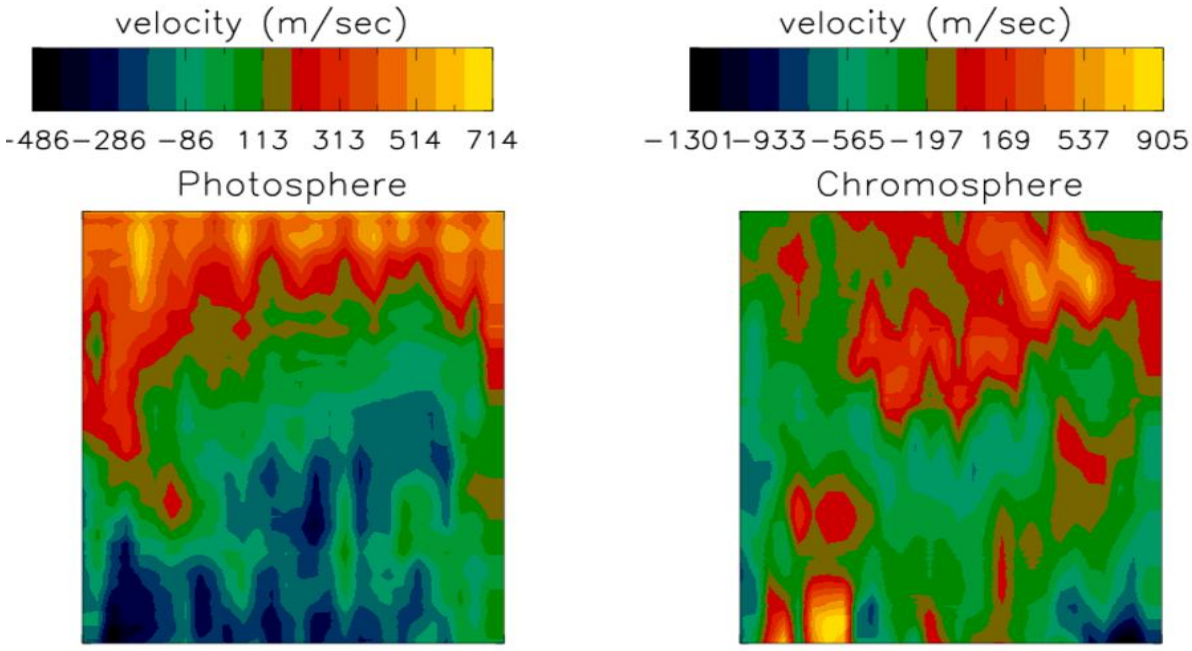

Figure 5.10: Velocity maps of active region NOAA 10940 at the photosphere (left panel) and chromosphere. The color bars on top of each map indicate the magnitude of LOS velocities in ms^{-1}. Negative values correspond to the flows towards the observer and positive values correspond to the flows away from the observer.

5.2 Velocity Structure Above AR2

5.2.1 Photosphere

Maps of velocities at the photosphere and chromosphere obtained using the shifts in the COG wavelength positions of Fe I and H α, respectively, with respect to the central umbra above the active region NOAA 10940 (AR2) are shown in Figure 5.10. The color bars shown above each map give information on the magnitude of the LOS

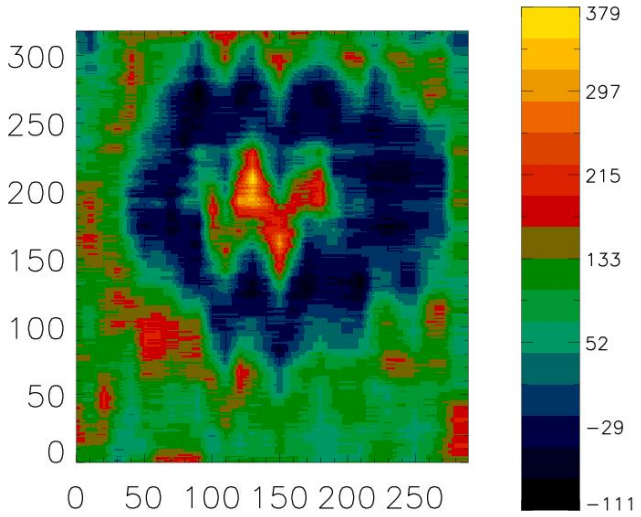

Figure 5.11: Map of photospheric velocity gradient above the active region NOAA 10940.

velocity. The positive values correspond to the flows away from the observer and the negative values correspond to the flows towards the observer. The velocity map at the photosphere shows the flow pattern consistent with the regular Evershed flow, meaning, the disk center side penumbra exhibit the flows towards the observer and the limb side penumbra exhibit flows away from the observer. Also, in confirmation with the earlier observations, the LOS velocity increases towards the edge of the sunspot. The velocity properties at chromosphere are discussed in the following section.

The velocity stratification at the photosphere above this active region is studied using bisector technique applied to Stokes-I profiles of Fe I (λ6569) discussed in

chapter 3. Bisectors are obtained at 9 equal intensity levels between line core and wing. The difference obtained by subtracting the velocity correspond to second bisector (higher height) from that of seventh bisector (lower height) is taken as representative of velocity gradient over the formation height of Fe I line. As before, the numbering of bisector is done by counting them from line core towards wing. A map of this velocity gradient is shown in Figure 5.11. One of the most striking features of this map is the blue strip around the umbra, the center of which is located close to the mid penumbra. As indicated in the color bar placed by the side of this map, blue color represents nagative velocity gradients, meaning, shift in the line wing bisector is more towards bluer side of the spectrum than the line core bisector. Closer examination of shifts in bisectors revealed that, both line core and wing bisectors of Fe I in disk center side penumbra show blue shift with respect to the central umbra while they exhibit red shift in limb side penumbra. This is consistent with the Evershed flow as center side penumbra show net upflow and limb side penumbra show net downflow [Balasubramaniam et al., 1997]. But, the reason for the appearance of larger negative velocity gradients observed close to central penumbra is yet to be explored. Similar kind of pattern are seen in the velocity gradient maps of AR1 and AR2 as well. Infact, AR2 observed by *Hinode*/SOT also show a strip of negative velocity gradients which are obtained through bisector analysis of Fe I at λ6301.5. The *Hinode*/SOT observations were smoothed spatially by $5.12'' \times 5.12''$ to match the spatial resolution to that of KTT observations. Further, the velocity map constructed out of average bisector shifts from line core to wing relative to central umbra shows the flow pattern consistent with that of COG velocity map (cf. Figure 5.10).

Another clearly noticeable point in Figure 5.11 is the larger velocity gradients in the umbral region. This may be an artifact introduced due to the Zeeman splitting. In the umbral region, the field strengths are larger and hence are the spectral lines splitting. If the the spectral lines are fully split due to the Zeeman effect, then the applicability of the bisector technique to intensity profiles is limited.

5.2.2 Chromosphere

The chromospheric COG velocity map shown on the right panel of Figure 5.10 above this active region does not exhibit the flow pattern which is consistent with the inverse Evershed flow. It is more structured with blue- and red-shifts distributed in a complicated way. The reference chosen for calculating the velocities will play a role in interpreting the line shifts as blue- or redshifts. Similar to AR1, the COG wavelength position of Stokes-I profiles averaged over small region around the central umbra is taken as the reference. However, if the flows are the signatures of inverse Evershed flow then one is expected to see a particular flow pattern. As noted above, there is no systematic flow pattern observed above this active region. It was seen in chapter 4 that this sunspot is surrounded by opposite polarity activities and so the structuring of the magnetic field above this active region is complicated. Also, this sunspot was located close to disk center and COG velocities represent only the LOS component of the velocity vector. However, as the inverse Evershed flows are more or less horizontal (for eg. see Georgakilas and Christopoulou [2003]) and hence may

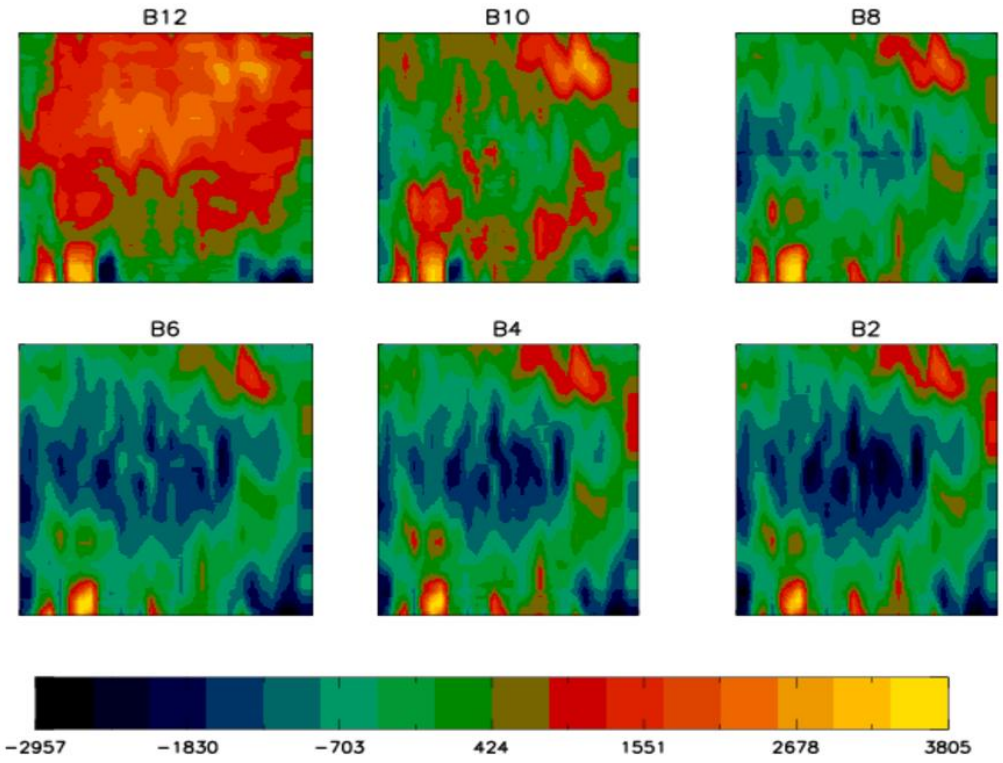

Figure 5.12: Velocity maps at the chromosphere obtained by finding the shifts in bisector positions with respect to the central umbra at different intensity levels of H α. The map B12, represents the velocity map corresponding to the bisector close to line wing and B2 corresponds to the bisector close to line core. Other maps viz., B10, B8, B6 and B4 corresponds to the bisector in between line wing and core.

not show up for this spot. These, probably, are the reasons why the inverse Evershed flow pattern is not apparent in the COG velocity map.

To understand further the structuring of plasma flow above this active region, bisector technique has been applied to H α Stokes-I profiles. Bisectors are obtained at 14 equal intensity levels between line core and wing. The velocities are obtained by finding the shifts in bisectors with respect to the mean bisectors of few profiles close to central umbral region. The mean is over all the bisectors from line core to wing and over the region close to central umbra. The chromospheric velocity maps corresponding to bisectors at different intensity levels of H α are shown in Figure 5.12. The map B2 correspond to the bisector close to line core (higher layer) and B12 correspond to the bisector close to line wing (lower layer) and other figures correspond to bisectors between the line wing and core. Notice the marked difference of velocity pattern at the lower to higher layers, changing from flows away from the observer at the lower heights to flows in the direction of LOS at higher heights with respect to central umbra with increasing amplitude. In other words, these maps indicate accelerated upflows with increase in their amplitudes towards the stronger field region with a reversal in the flow direction at the lower heights.

The scatter plot of the difference in velocities of wing and core bisectors, which represent the velocity gradient over the line formation height, v/s the photospheric field strengths are shown in Figure 5.13. This figure clearly indicate that the chromospheric velocity gradients increase monotonically towards the center of the umbra.

In other words, stronger the field strengths at the photosphere, larger the velocity gradients at the chromosphere. As it was seen in the previous chapter that, for this active region, larger field gradients above the umbra are observed in terms of field inclinations. Hence there is a possibility that the larger velocity gradients above the umbra are caused due to the larger gradients in the field inclinations. However, similar kind of velocity gradients were observed for AR1 in which case it was interpreted as due to rapid decrease in the umbral field strengths because of the presence of accelerated upflows above the umbral region. We encounter difficulty in the similar kind of interpretation as the central umbral field strengths above this active region vary slowly with height compared to penumbra but, there is an indication of accelerated upflows above this active region (cf. previous paragraph). However, to conclude, the flows are upflows or downflows, proper reference is important, which is difficult to find for H α. To understand these structuring of velocity and magnetic fields, the spectropolarimetric observations of H α have to be inverted under realistic model atmosphere such as done by Socas-Navarro [2005]. In his work, Socas-Navarro [2005] has inverted Stokes profiles of Ca II triplet at λ8542 by taking into account the gradients in the physical parameters which include velocity and magnetic fields along with the NLTE effects.

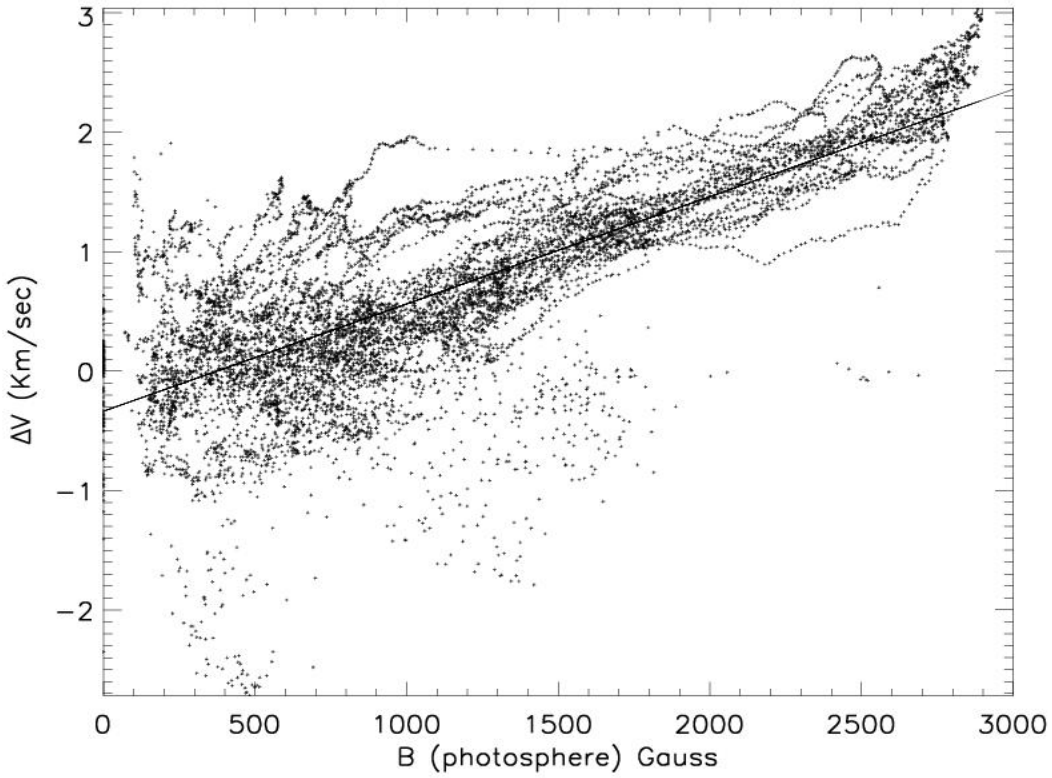

Figure 5.13: Plots of velocity gradients at the chromosphere with respect to the photospheric magnetic field strengths.

5.2.3 Stokes V Amplitude Asymmetry

Scatter plots of Stokes-V amplitude asymmetries and photospheric field strengths are shown in Figure 5.14 observed at the photosphere for AR2. Top panel in this figure is for the full FOV, bottom left and right panels are for umbral and penumbral regions. At the photosphere, amplitude asymmetries are smaller in the umbral region compared to penumbral region. In other words, the asymmetries tend to zero gradually towards the stronger field regions. This is similar to what was observed for AR1 (cf. Figure 5.8). One of the differences we see between these two active regions is that, for AR1, large number of points have negative amplitude asymmetries while for AR2, the points with positive amplitude asymmetries are larger. Similar kind of trend is observed for AR3 also in which large number of points exhibit negative amplitude asymmetry. Note that, AR1 and AR3 exhibit negative polarity magnetic field (field direction away from the LOS) while AR2 exhibit positive polarity magnetic field. This may imply that the sign of amplitude asymmetry depends on the polarity of the magnetic field. This may give a useful hint on the stratification of the magnetic vector in the solar atmosphere. However, at this point we restrain from further interpretation as it is important to make sure that there are no systematic effects from the instrument.

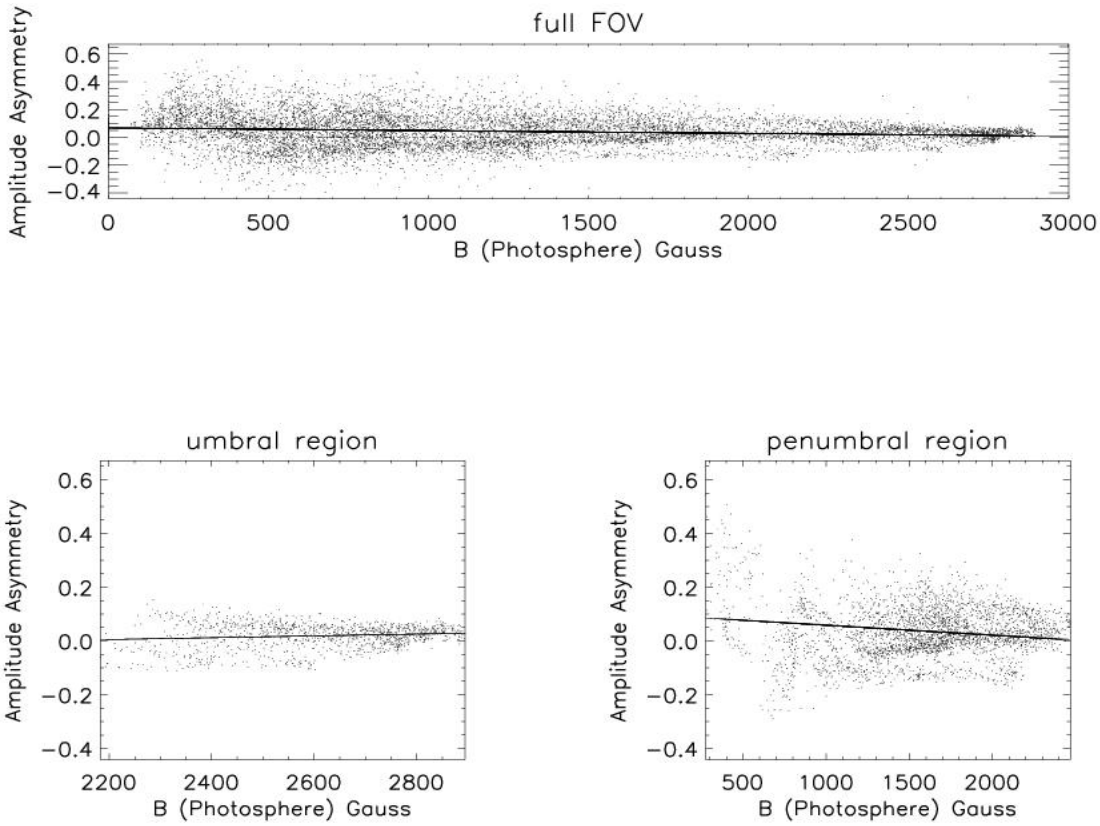

Figure 5.14: Plots of Stokes V amplitude asymmetry at the photosphere with respect to the photospheric magnetic field strengths.

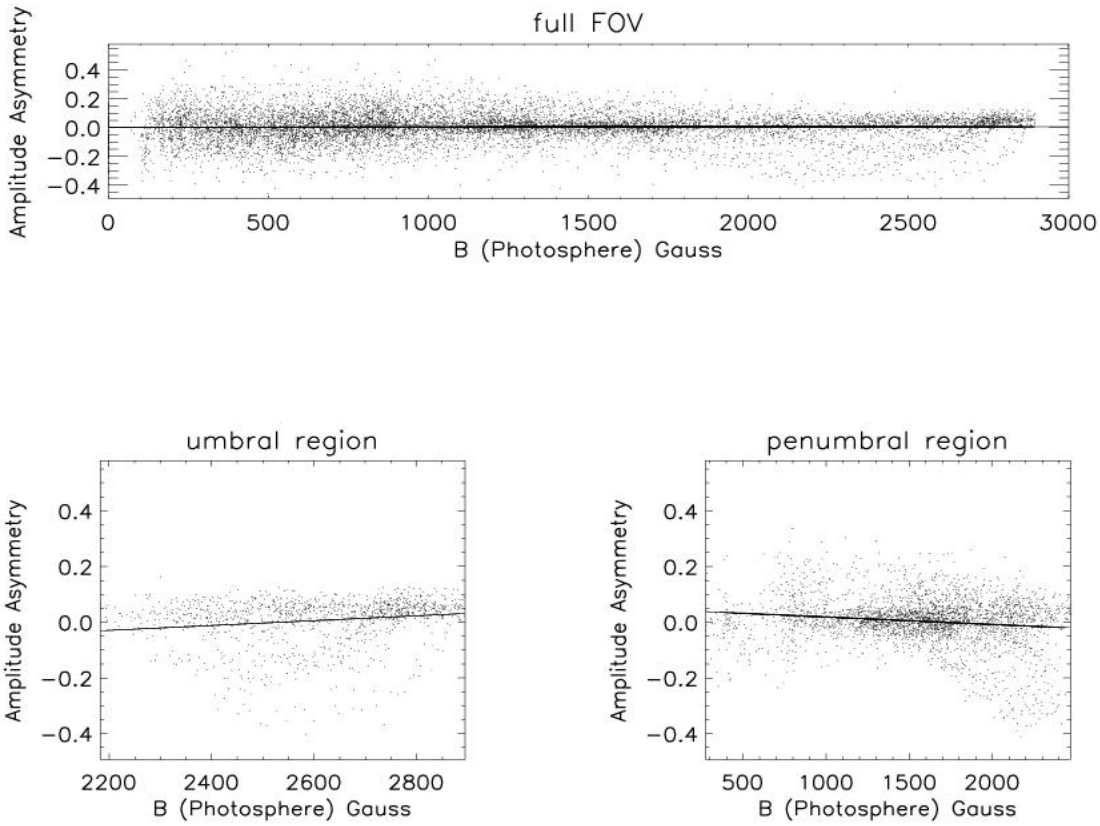

Figure 5.15: Plots of Stokes V amplitude asymmetry at the chromosphere with respect to the photospheric magnetic field strengths.

5.3 Velocity Structure Above AR3

At the photosphere, this sunspot exhibit COG velocity pattern consistent with the Evershed flow, meaning, disk center penumbra exhibit flows towards the observer and limb side penumbra exhibit flows away from the observer. Also, the velocity gradient map is similar to what was observed for AR2 (Figure 5.11). At the chromosphere, the velocities obtained through COG method do not show distribution consistent with the inverse Evershed flow similar to what was observed for AR2. But, the velocity maps correspond to bisectors at different intensity levels of H α line profile shown in Figure 5.17 indicate totally a different velocity stratification above this active region in comparison with that of AR2 (Figure 5.12). At few locations above this active region the flow direction is same both at the lower and higher layers. At few locations, lower layers exhibit upflows whereas higher layers show downflows. Over all in this active region there exist a complicated velocity structure which is totally different from what is observed above AR1 and AR2. As it was seen in chapter 4 that the magnetic field topology above the active regions AR1, AR2 and AR3 are different and so the case with the plasma flow. This implies that the structuring of magnetic field play an important role in guiding the plasma flow. However, the one-to-one relation between the velocity and magnetic stratification is not clear. This further emphasises the need for inversion techniques to be developed so that the spectropolarimetric data can be used effectively to understand the dynamics at the chromosphere.

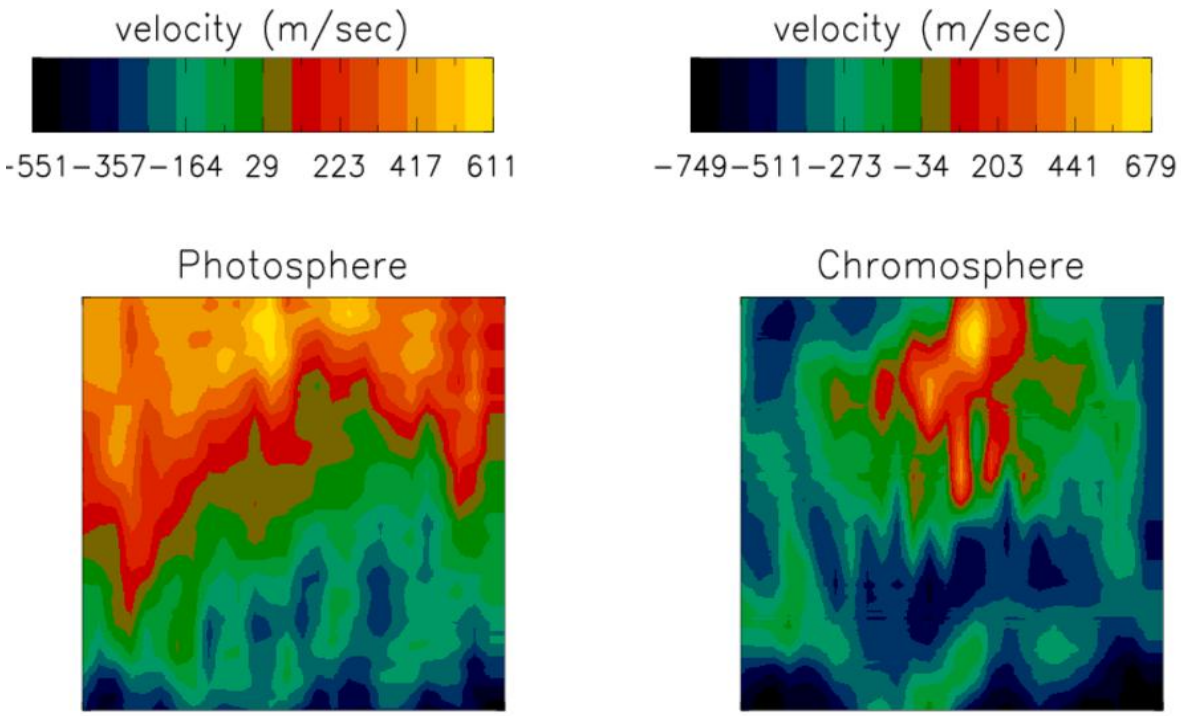

Figure 5.16: Velocity maps of active region NOAA 10941 at the photosphere (left panel) and chromosphere. The color bars on top of each map indicate the magnitude of LOS velocities in ms^{-1}. Negative values correspond to the flows towards the observer and positive values correspond to the flows away from the observer.

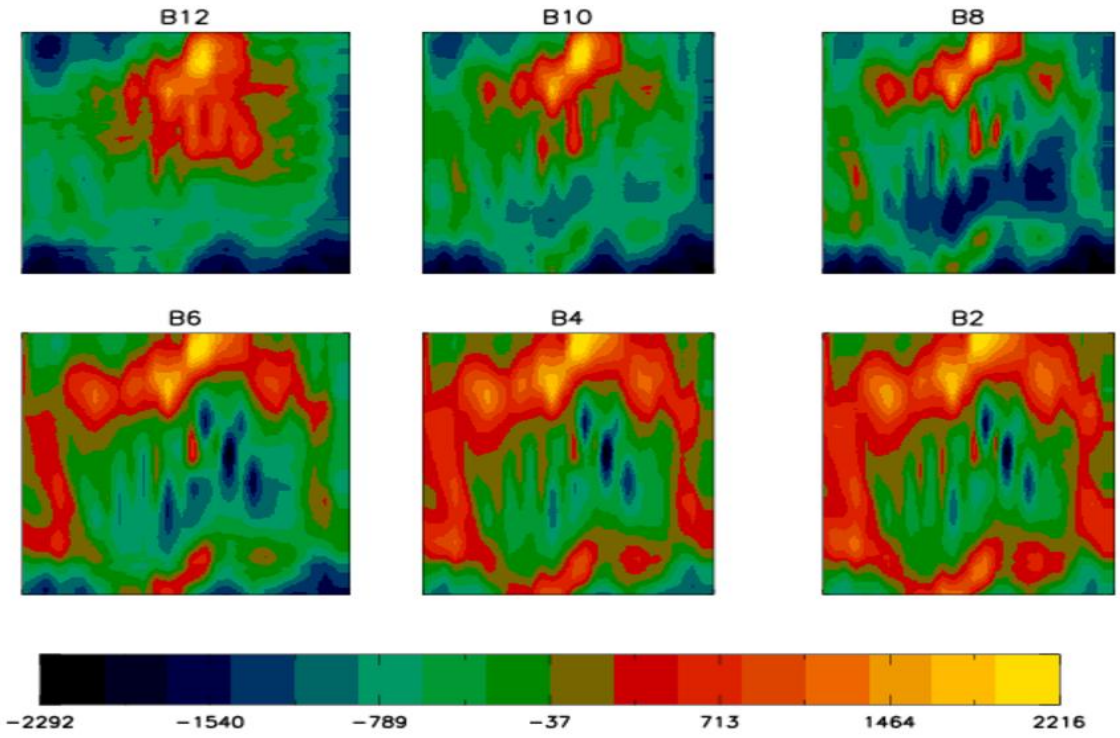

Figure 5.17: Same as Figure 5.12 but for the active region NOAA 10941.

5.4 Summary

The velocity structure above the active regions NOAA 10875, 10940 and 10941 have been discussed in this chapter. The velocities are derived using the COG wavelength positions of Stokes-I profiles with respect to an average central umbra. Velocities thus obtained represent the plasma flow along the LOS, averaged over the height of formation of the line. All the three spots studied in this chapter exhibit the velocity structure which is consistent with the well known Evershed effect at the photosphere. But, at the chromosphere, velocity structure is consistent with the inverse Evershed effect only in AR1, where as AR2 and AR3 do not exhibit any such systematic pattern. They show mix of up- and downflows distributed in a random manner. This may be due to the location of these sunspots on the solar disk as AR2 and AR3 were located much closer to the disk center than AR3. This fact is reflected in the reduced magnitude of the LOS velocities for AR2 and AR3 compared to AR1.

The velocity gradients at the photosphere and chromosphere have been studied using the bisector technique applied to Stokes-I profiles of Fe I line at λ6569 and H α, respectively. The velocity gradients are derived using the differences in wavelength positions of line wing and core side bisectors. At the photosphere, a strip of negative velocity gradients are observed around the central penumbral region.

From the bisector analysis of H α Stokes-I profiles, a monotonic increase in the velocity gradients towards the central umbra is observed in all the three spots. Sur-

prisingly, the magnitude of the velocity gradients of all the three spots are comparable and show similar kind of functional form with respect to the magnetic field strengths though the magnetic field topology above these spots is different from each other. However, the velocity maps corresponding to the individual bisectors with respect to central umbra show different structures for these spots. The velocity structures at lower and higher layers above AR1 are similar, where as flow reversal is observed for AR2, with lower layers showing redshifts and higher layers showing blue shifts with respect to the central umbra. The change over from redshifts to blueshifts is gradual. Above AR3, the velocity pattern at the higher layers is more or less similar to that of lower layers. At few locations, AR3 exhibit flow reversals.

Stokes-V amplitude asymmetry is also studied in this chapter. As expected, the amplitude asymmetries are smaller in the umbral photosphere compared to the penumbral photosphere. In the umbral chromosphere, the Stokes-V amplitude asymmetries are larger compared to their photospheric counterparts. This may be due to the larger velocity and magnetic field gradients in the umbral chromosphere than in the umbral photosphere. One interesting point observed regarding the distribution of the amplitude asymmetry over the sunspots studied in this thesis is that, large number of points have positive amplitude asymmetry for positive polarity sunspots and negative amplitude asymmetry for negative polarity sunspots. This may suggest that the Stokes-V amplitude asymmetry can be used to study the gradient in the field inclination. However, the number of sunspots analyzed is very few to generalize this statement. The amplitude asymmetries can be studied for more sunspots

with different instruments as well as at different disk positions in order to make sure that there are no systematic instrumental errors and bias in the observations. More studies are required involving synthesis of Stokes-V profiles for different field configurations and comparing the changes in the amplitude asymmetries.

Chapter 6

Conclusions and Future Developments

For the purpose of carrying out spectropolarimetric observations on the Sun, a dual-beam polarimeter has been fabricated and installed at KTT. The dual-beam polarimeter was preferred because it reduces the seeing induced spurious polarization. It was seen in chapter 1 that the Stokes parameters are defined using the difference in intensities of orthogonally polarized beams, and recording them simultaneously will reduce the errors introduced due to seeing induced intensity fluctuations. Also, the flat field errors inherent to the dual-beam system are reduced by using a modulation/demodulation scheme (cf. chapter 2) which incorporates the well known beam-swapping technique. The modulation scheme requires eight steps of intensity

measurements to achieve good efficiency for all the Stokes parameters. This is a well balanced scheme, meaning, the output intensity is a function of all the Stokes parameters with equal weights in all the eight measurements and the demodulation is done in such a way that all the eight intensity measurements are used to derive the Stokes parameters. The efficiency in measuring Stokes parameters-Q, U, and V is 0.5, 0.5 and 0.7, respectively at the design wavelength of λ6300. Due to the chromatic nature of the retarders used in the polarimeter, the individual efficiencies of Stokes parameters are different at different wavelengths. An experiment to study the wavelength dependence of the polarimetric efficiency of individual Stokes parameters match very well with the theoretically expected values. Stokes-Q and V have better efficiency in the redder wavelengths of the visible range and Stokes-U has better efficiency in the bluer wavelengths.

Calibration of the polarimeter is done almost on daily basis during the observations. The accuracies achieved in determining the Stokes parameters Q, U and V are 0.3%, 0.36% and 0.34%, respectively. This is limited mainly by the uncertainty in the determination of the retardance of the calibration unit retarder ($\mathrm{R_{CU}}$) which is known to an accuracy of 0.2^o. The accuracy in determining the Stokes parameters can be improved by knowing the retardance of ($\mathrm{R_{CU}}$) with better accuracy.

Through an experiment to study the noise in the polarization data, it was found that the noise in the measurement of Stokes parameters is confined by the photon or statistical noise. For an exposure time of 2.4 s, the noise in the polarization data

was reduced to <0.1%. This means, the polarisation sensitivity of the polarimeter can be improved by availing more number of photons. This may involve regular aluminization of the telescope optics to increase the throughput of the telescope and use of fast CCD cameras with good quantum efficiency. Though longer integrations can increase the number of photons, it will slow down overall measurement process.

It was found through another experiment that the optimum slit width for KTT setup is 48μ and the corresponding spectral resolution is 32.5 ± 0.5 mÅ.

The magnetic field inferred by inverting the Stokes profiles of Fe I at λ6569 observed using this polarimeter matches very well with that of *Hinode*/SOT spectropolarimetric observations. For this purpose, the active region considered was NOAA 10940. The *Hinode*/SOT observations were to be smoothed by $5.12'' \times 5.12''$ to match with the seeing degraded observations of KTT.

Spectropolarimetric observations of several active regions have been carried out using the polarimeter polarimeter installed at KTT. The wavelength region of observations include H α, whose height of formation ranges from upper photosphere to middle chromosphere and Fe I at λ6569 which forms at the photosphere. The main motivation for using these lines was to study the stratification of velocity and magnetic fields simultaneously at the photosphere and chromosphere.

The vector magnetic field at the photosphere was obtained by inverting the Stokes profiles of Fe I line and at the chromosphere from H α using WFA method. The mag-

netic field at the photosphere show a well established distribution. The field strength at the darkest region (central umbra) of the activity is strongest and decreases uniformly along the sunspot radius where as its inclination increases gradually towards the periphery of the sunspot. On the other hand, the magnetic field topology at the chromosphere changes according to the field distribution at the photosphere. For an isolated sunspot, the magnetic field inferred through H α observations indicate regular divergence of the field as it propagates from the photosphere to chromosphere. This is confirmed through X-ray images of the same active region observed by *Hinode*/XRT. The fountain like structure seen in *Hinode*/XRT for this active region is typical of an isolated sunspot. For the spot which is surrounded by opposite polarity activities, the magnetic field does not diverge as fast as that of the isolated spot rather there is a large concentration of the field in the central umbral region. The fields have larger inclinations, as large as 70^o, in the umbral chromosphere. X-ray images of this spot observed by *Hinode*/XRT show more of arcade structures with one of their foot points located in the main sunspot and another in the nearby opposite polarity region. The field inclination at the central umbra is comparable to that of penumbra, and decreases rapidly towards the edge of the umbra. Also the field strength is large in the central umbra and decreases very rapidly with radial distance within the umbra. This may indicate foot point of a magnetic loop located in the umbral region with another foot point located in the nearby activity, as evidenced by the X-ray images. For the third sunspot, observed for this thesis and which show light bridges dividing the umbra and surrounded partially by the penumbra, the field measurement at the chromosphere indicate quicker weakening of the LOS field

strengths in the umbra. For this active region, the H α Stokes-Q and U profiles are hardly discernible. Quicker weakening of the LOS field strengths and the absence of linear polarization signals in H α prompted us to conclude that the umbral fields diverge faster compared to penumbral fields.

The velocity structures at the photosphere and chromosphere are studied by analyzing the spectral lines Fe I line at λ6569 and H α, respectively. The velocities derived using the COG method are consistent with the well known Evershed effect, meaning, the center side penumbra show flows toward the observer and limb side penumbra show flows away from the observer. The velocity gradients are studied using bisector technique applied to Stokes-I profiles. One of the intriguing findings from this analysis is a strip of negative velocity gradients close to central umbra at the photosphere. This is not readily understandable based on the flows which are consistent with the Evershed flows. This is because, the velocity gradients are expected to have opposite signs in the center side penumbra and limb side penumbra [Solanki, 2003]. Many more observations of different sunspots at different locations on the disk are needed to confirm as well as interpreting this result. To understand the cause for this larger negative velocity gradients observed around the central penumbra, more forward modeling of the spectral lines will also be required.

Another new result found in this thesis is the larger velocity gradients in the umbral chromosphere compared to penumbral chromosphere. The velocity gradients gradually increase towards the central umbra. It is interesting to note here that the

magnitude of velocity gradients for all three active regions studied in this thesis are comparable, though the magnetic structuring above these active regions is completely different.

Further examination of the individual bisectors of H α, it was found that, AR1 exhibit larger accelerated upflows in the central umbra. This is consistent with the magnetic field measurements as well, because, it was discussed in chapter 4 that the the magnetic field strength decreases more rapidly with height compared to penumbral fields. For AR2, downflows are observed at the lower layers of the H α line forming region where as in the higher layers upflows are observed. This scenario may indicate net diverging flow. However, the reference used to find the velocities plays a major role in interpreting the shifts in the wavelength position of spectral lines is due to flows towards the observer or due to the flows away from the observer. It is difficult to find a correct reference for H α. Proper wavelength calibration will help in the better interpretation of the wavelength shift measurements. For AR3, the velocity pattern at the higher layers is more or less similar to that of lower layers. At few locations, AR3 exhibit flow reversals. Overall, the velocity structures observed above all three sunspots studied in this thesis are different. It was discussed in chapter 4 that the magnetic field topologies above these sunspots are different from each other. Hence, the structuring of the magnetic field influence the plasma flow, which is well know. However, one-to-one correspondence between magnetic field distribution and the flow pattern observed above these active regions is yet to find satisfactory explanation.

6.1 Limitations and Future Needs

On the instrument side, there are lot of improvements required to establish it an user friendly. The major requirement will be to make it automated before releasing it as a user facility for the Indian solar community. The polarimeter is now being operated through manual rotation of the waveplates. Motorization of the rotations will help in speeding up the observations. The scanning of the region-of-interest (ROI) is also done manually. Automatized scanning of the ROI will help in obtaining a good map of a chosen region through controlled scan at a desired step. Atomization of the scanning will also allow us to go finer steps than the $2''$ steps used in this thesis. The image drift at the tunnel was a major limitation of the previous polarimetric setup. At present, the image stability is quiet good but having an image tracker will make even better. Steps are being taken to implement a limb tracker for the tunnel as well as a correlation tracker for a particular ROI. These facility upgradation along with atomizing the scanning will allow the user to go for scanning steps finer than $1''$

The intriguing structures seen in H α prompted us to do the vector magnetic field estimation above these structures and hence used the WFA method for these estimations. However, we would like to point out here that the magnetic field derived using WFA method has its own limitation. Also, it is not possible to derive the stratification of the magnetic field over the line formation height which will be required in order to study the structuring at different layers as seen in tunable narrow-band imaging. To make use of H α spectro-polarimetry to its full potential, inversion of

Stokes profiles of this line is essential. At present, it seems to be a very difficult task [Socas-Navarro and Uitenbroek, 2004]. Given the constraints for the full inversion of H α, it is best to use the WFA method along with simultaneous imaging in H α. This will give atleast a qualitative picture of the magnetic structuring in the chromosphere. It has been shown in this thesis that, indeed the magnetic structuring in the chromosphere show up in the derived magnetic and velocity parameters. Another option is to use a different spectral line for magnetic field diagnostics at the chromosphere like the Ca II triplet [Socas-Navarro, 2005]. However, the Ca triplet does not show the similar chromospheric structuring as is seen with H α. Also, being close to the near IR region it is not always possible to use this line in observatories where the sky condition has an upper cut-off wavelength. However, it will be wise to first do a simultaneous spectro-polarimetric observations with H α and Ca triplet and estimate the relative advantages and dis-advantages of these two spectral lines especially with a view to study the chromospheric structuring.

Bibliography

H. I. Abdussamatov. On the Magnetic Fields and Motions in Sunspots at Different Atmospheric Levels. *Solar Phys.*, 16:384–397, 1971.

C. E. Alissandrakis, D. Dialetis, P. Mein, B. Schmieder, and G. Simon. The Evershed flow in the solar photosphere, chromosphere and chromosphere-corona transition region. *Astron. Astrophys.*, 201:339–349, 1988.

S. K. Antiochos. The Magnetic Topology of Solar Eruptions. *Astrophys. J. Lett.*, 502:L181+, 1998.

J. Arnaud, P. Mein, and J. Rayrole. The Solar Telescope THEMIS. In *Crossroads for European Solar and Heliospheric Physics. Recent Achievements and Future Mission Possibilities*, volume 417 of *ESA Special Publication*, pages 213–+, 1998.

M. J. Aschwanden. *Physics of the Solar Corona. An Introduction with Problems and Solutions (2nd edition)*. Pour la Science, 2005.

L. H. Auer, L. L. House, and J. N. Heasley. The determination of vector magnetic fields from Stokes profiles. *Solar Phys.*, 55:47–61, 1977.

K. S. Balasubramaniam. *Stokes polarimetry and the measurement of vector magnetic fields in solar active regions.* PhD thesis, Indian Institute of Science, 1988.

K. S. Balasubramaniam, P. Venkatakrishnan, and J. C. Bhattacharyya. Measurement of vector magnetic fields. I - Theoretical approach to the instrumental polarisation of the Kodaikanal Solar Tower. *Solar Phys.*, 99:333–348, 1985.

K. S. Balasubramaniam, S. L. Keil, and S. Tomczyk. Stokes Profile Asymmetries in Solar Active Regions. *Astrophys. J.*, 482:1065–+, 1997.

K. S. Balasubramaniam, E. B. Christopoulou, and H. Uitenbroek. Promises and Pitfalls of Solar Hα Zeeman Spectropolarimetry. *Astrophys. J.*, 606:1233–1238, 2004.

M. K. V. Bappu. Solar Physics at Kodaikanal. *Solar Phys.*, 1:151–156, 1967.

C. Beck. A 3D sunspot model derived from an inversion of spectropolarimetric observations and its implications for the penumbral heating. *Astron. Astrophys.*, 480:825–838, 2008.

C. Beck, R. Schlichenmaier, M. Collados, L. Bellot Rubio, and T. Kentischer. A polarization model for the German Vacuum Tower Telescope from in situ and laboratory measurements. *Astron. Astrophys.*, 443:1047–1053, 2005.

J. M. Beckers. Inhomogeneities in the Evershed flow. In *Atti del Convegno Sulle Macchie Solari*, pages 186–+, 1964.

L. R. Bellot Rubio. Stokes Inversion Techniques: Recent Advances and New Challenges. In R. Casini and B. W. Lites, editors, *Astronomical Society of the Pacific*

Conference Series, volume 358 of *Astronomical Society of the Pacific Conference Series*, pages 107–+, 2006.

L. R. Bellot Rubio, H. Balthasar, M. Collados, and R. Schlichenmaier. Field-aligned Evershed flows in the photosphere of a sunspot penumbra. *Astron. Astrophys.*, 403:L47–L50, 2003.

L. R. Bellot Rubio, K. Langhans, and R. Schlichenmaier. Multi-line spectroscopy of dark-cored penumbral filaments. *Astron. Astrophys.*, 443:L7–L10, 2005.

L. R. Bellot Rubio, R. Schlichenmaier, and A. Tritschler. Two-dimensional spectroscopy of a sunspot. III. Thermal and kinematic structure of the penumbra at 0.5 arcsec resolution. *Astron. Astrophys.*, 453:1117–1127, 2006.

P. R. Bevington and D. K. Robinson. *Data reduction and error analysis for the physical sciences*. Data reduction and error analysis for the physical sciences, 3rd ed., by Philip R. Bevington, and Keith D. Robinson. Boston, MA: McGraw-Hill, ISBN 0-07-247227-8, 2003., 2003.

J. C. Bhattacharyya. *Studies of solar magnetic and velocity fields*. PhD thesis, University of Calcutta, 1969.

M. Bianda, S. K. Solanki, and J. O. Stenflo. Hanle depolarisation in the solar chromosphere. *Astron. Astrophys.*, 331:760–770, 1998.

M. Born and E. Wolf, editors. *Principles of optics : electromagnetic theory of propagation, interference and diffraction of light*, 1999.

C. Briand and A. Vecchio. Chromospheric polarity reversal on sunspots: New insight from spectro-polarimetric measurements. *Astron. Astrophys.*, 403:L33–L36, 2003.

N. Brynildsen, P. Maltby, P. Brekke, S. V. H. Haugan, and O. Kjeldseth-Moe. SOHO Observations of the Structure and Dynamics of Sunspot Region Atmospheres. *Solar Phys.*, 186:141–191, 1999.

N. Brynildsen, P. Maltby, T. Fredvik, O. Kjeldseth-Moe, and K. Wilhelm. Sunspot Plumes and Flow Channels. *Solar Phys.*, 198:89–131, 2001.

R. Casini and E. Landi degl'Innocenti. Properties of the first-order moments of the polarization profiles of hydrogen lines. *Astron. Astrophys.*, 291:668–678, 1994.

G. Cauzzi, L. A. Smaldone, K. S. Balasubramaniam, and S. L. Keil. On the calibration of line-of-sight magnetograms. *Solar Phys.*, 146:207–227, 1993.

S. Chandrasekhar. *Radiative transfer*. New York: Dover, 1960, 1960.

D. P. Choudhary, Y. Suematsu, and K. Ichimoto. Observational Study of the Three-Dimensional Magnetic Field Structure and Mass Motion in Active Regions. *Solar Phys.*, 209:349–360, 2002.

H. C. Dara, S. Koutchmy, and C. E. Alissandrakis. Photospheric and chromospheric magnetic field structure of a bipolar sunspot region. *Astron. Astrophys.*, 277: 648–+, 1993.

E. L. Degl'Innocenti and M. L. Degl'Innocenti. Quantum theory of line formation in a magnetic field. *Solar Phys.*, 27:319–329, 1972.

del Toro Iniesta and M. Collados. Optimum Modulation and Demodulation Matrices for Solar Polarimetry. *Applied Optics*, 39:1637–1642, 2000.

J. C. del Toro Iniesta. *Introduction to Spectropolarimetry*. Introduction to Spectropolarimetry, by Jose Carlos del Toro Iniesta, pp. 244. ISBN 0521818273. Cambridge, UK: Cambridge University Press, April 2003., 2003.

J. C. Del Toro Iniesta and B. Ruiz Cobo. Stokes Profiles Inversion Techniques. *Solar Phys.*, 164:169–182, 1996.

J. C. del Toro Iniesta, L. R. Bellot Rubio, and M. Collados. Cold, Supersonic Evershed Downflows in a Sunspot. *Astrophys. J. Lett.*, 549:L139–L142, 2001.

J.-P. Delaboudinière, G. E. Artzner, J. Brunaud, A. H. Gabriel, J. F. Hochedez, F. Millier, X. Y. Song, B. Au, K. P. Dere, R. A. Howard, R. Kreplin, D. J. Michels, J. D. Moses, J. M. Defise, C. Jamar, P. Rochus, J. P. Chauvineau, J. P. Marioge, R. C. Catura, J. R. Lemen, L. Shing, R. A. Stern, J. B. Gurman, W. M. Neupert, A. Maucherat, F. Clette, P. Cugnon, and E. L. van Dessel. EIT: Extreme-Ultraviolet Imaging Telescope for the SOHO Mission. *Solar Phys.*, 162:291–312, 1995.

K. P. Dere, B. Schmieder, and C. E. Alissandrakis. Flow patterns in a sunspot region observed in the photosphere, chromosphere and transition region. *Astron. Astrophys.*, 233:207–219, 1990.

D. Dialetis, P. Mein, and C. E. Alissandrakis. The Evershed flow as a steady-state homogeneous phenomenon. *Astron. Astrophys.*, 147:93–102, 1985.

J.-F. Donati, M. Semel, and J. C. del Toro Iniestia. The magnetic field of the AP star Epsilon UMa. *Astron. Astrophys.*, 233:L17–L20, 1990.

D. F. Elmore, B. W. Lites, S. Tomczyk, A. P. Skumanich, R. B. Dunn, J. A. Schuenke, K. V. Streander, T. W. Leach, C. W. Chambellan, and H. K. Hull. The Advanced Stokes Polarimeter - A new instrument for solar magnetic field research. In D. H. Goldstein and R. A. Chipman, editors, *Polarization analysis and measurement; Proceedings of the Meeting, San Diego, CA, July 19-21, 1992 (A93-33401 12-35), p. 22-33.*, volume 1746 of *Presented at the Society of Photo-Optical Instrumentation Engineers (SPIE) Conference*, pages 22–33, 1992.

R. Erdélyi. Heating of the Solar Corona: Review. *Publications of the Astronomy Deparment of the Eotvos Lorand University*, 15:7–+, 2005.

R. Erdélyi and I. Ballai. Heating of the solar and stellar coronae: a review. *Astronomische Nachrichten*, 328:726–733, 2007.

J. Evershed. Radial movement in sun-spots. *Mon. Not. Roy. Astron. Soc.*, 69:454–+, 1909.

D. M. Fluri and J. O. Stenflo. Continuum polarization in the solar spectrum. *Astron. Astrophys.*, 341:902–911, 1999.

P. Foukal, C. Fröhlich, H. Spruit, and T. M. L. Wigley. Variations in solar luminosity and their effect on the Earth's climate. *Nature*, 443:161–166, 2006.

A. Gandorfer. Liquid crystal based polarimetric system, a process for the calibration

of this polarimetric system, and a polarimetric measurement process. *Appl. Optics*, 38:1402–, 1999.

G. A. Gary. Plasma Beta above a Solar Active Region: Rethinking the Paradigm. *Solar Phys.*, 203:71–86, 2001.

A. A. Georgakilas and E. B. Christopoulou. Temporal Behavior of the Evershed Effect. *Astrophys. J.*, 584:509–523, 2003.

A. A. Georgakilas, E. B. Christopoulou, A. Skodras, and S. Koutchmy. Chromospheric Evershed flow. *Astron. Astrophys.*, 403:1123–1133, 2003.

L. Golub, E. Deluca, G. Austin, J. Bookbinder, D. Caldwell, P. Cheimets, J. Cirtain, M. Cosmo, P. Reid, A. Sette, M. Weber, T. Sakao, R. Kano, K. Shibasaki, H. Hara, S. Tsuneta, K. Kumagai, T. Tamura, M. Shimojo, J. McCracken, J. Carpenter, H. Haight, R. Siler, E. Wright, J. Tucker, H. Rutledge, M. Barbera, G. Peres, and S. Varisco. The X-Ray Telescope (XRT) for the Hinode Mission. *Solar Phys.*, 243: 63–86, 2007.

S. Gosain and D. Prasad Choudhary. Simultaneous Stokes-V diagnostic of a Sunspot using Mg b and Fe I lines. *Solar Phys.*, 217:119–132, 2003.

V. M. Grigorev and J. M. Katz. Magnetoactive lines in the medium with the velocity gradient. *Solar Phys.*, 42:21–35, 1975.

V. M. Grigorjev and J. M. Katz. The Crossover and Magneto-Optical Effects in Sunspot Spectra. *Solar Phys.*, 22:119–128, 1972.

G. E. Hale. On the Probable Existence of a Magnetic Field in Sun-Spots. *Astrophys. J.*, 28:315–+, 1908.

Y. Hanaoka. Hα Stokes V/I Features Observed in a Solar Active Region. *Pub. Astron. Soc. Japan*, 57:235–244, 2005.

J. Harvey, W. Livingston, and C. Slaughter. A Line-Profile Stokesmeter: Preliminary Results on Non-Sunspot Fields. In *Line Formation in the Presence of Magnetic Fields*, pages 227–+, 1972.

J. W. Harvey. Chromospheric Magnetism. In R. Casini and B. W. Lites, editors, *Astronomical Society of the Pacific Conference Series*, volume 358 of *Astronomical Society of the Pacific Conference Series*, pages 419–+, 2006.

E. Hetch. *Optics*. Pierson education Asia publisher, 2002.

R. M. E. Illing, D. A. Landman, and D. L. Mickey. Broad-band circular polarization of sunspots - Spectral dependence and theory. *Astron. Astrophys.*, 41:183–185, 1975.

J. Jefferies, B. W. Lites, and A. Skumanich. Transfer of line radiation in a magnetic field. *Astrophys. J.*, 343:920–935, 1989.

J. T. Jefferies and D. L. Mickey. On the inference of magnetic field vectors from Stokes profiles. *Astrophys. J.*, 372:694–702, 1991.

J. Jurčák and L. R. Bellot Rubio. Penumbral models in the light of Hinode spectropolarimetric observations. *Astron. Astrophys.*, 481:L17–L20, 2008.

O. Kjeldseth-Moe, N. Brynildsen, P. Brekke, O. Engvold, P. Maltby, J.-D. F. Bartoe, G. E. Brueckner, J. W. Cook, K. P. Dere, and D. G. Socker. Gas flows in the transition region above sunspots. *Astrophys. J.*, 334:1066–1075, 1988.

N. I. Kobanov, D. V. Makarchik, and A. A. Sklyar. Photospheric and chromospheric oscillations in the base of coronal holes. *Solar Phys.*, 217:53–67, 2003.

T. Kosugi, K. Matsuzaki, T. Sakao, T. Shimizu, Y. Sone, S. Tachikawa, T. Hashimoto, K. Minesugi, A. Ohnishi, T. Yamada, S. Tsuneta, H. Hara, K. Ichimoto, Y. Suematsu, M. Shimojo, T. Watanabe, S. Shimada, J. M. Davis, L. D. Hill, J. K. Owens, A. M. Title, J. L. Culhane, L. K. Harra, G. A. Doschek, and L. Golub. The Hinode (Solar-B) Mission: An Overview. *Solar Phys.*, 243:3–17, 2007.

A. Lagg. Recent advances in measuring chromospheric magnetic fields in the He I 10830 Å line. *Advances in Space Research*, 39:1734–1740, 2007.

A. Lagg, J. Woch, S. K. Solanki, and N. Krupp. Supersonic downflows in the vicinity of a growing pore. Evidence of unresolved magnetic fine structure at chromospheric heights. *Astron. Astrophys.*, 462:1147–1155, 2007.

E. Landi degl'Innocenti and M. Landi degl'Innocenti. A Perturbative Solution of the Transfer Equations for the Stokes Parameters in a Magnetic Field. *Solar Phys.*, 31:299–+, 1973.

E. Landi Degl'Innocenti and M. Landolfi. Thermodynamical properties of unresolved

magnetic flux tubes. I: A diagnostic method based on circular polarization ratios in line pairs. *Solar Phys.*, 77:13–26, 1982.

M. Landolfi. A possible diagnostic method for magnetic field and velocity gradients in sunspots. *Solar Phys.*, 109:287–306, 1987.

M. Landolfi, P. Arena, and E. Landi Degl'Innocenti. On the diagnostic of magnetic fields in sunspots through the interpretation of Stokes parameters profiles. *Solar Phys.*, 93:269–287, 1984.

K. Langhans, G. B. Scharmer, D. Kiselman, M. G. Löfdahl, and T. E. Berger. Inclination of magnetic fields and flows in sunspot penumbrae. *Astron. Astrophys.*, 436:1087–1101, 2005.

W. Li, G. Ai, and H. Zhang. Reversed-polarity structures of chromospheric magnetic field. *Solar Phys.*, 151:1–14, 1994.

B. W. Lites. Steady flows in the chromosphere and transition-zone above active regions as observed by OSO-8. *Solar Phys.*, 68:327–337, 1980.

B. W. Lites. Rotating Waveplates as Polarization Modulators for Status Polarimetry on the Sun: Evaluation of Seeing-Induced Crosstalk Errors. *Appl. Optics*, 26: 3838–3845, 1987.

B. W. Lites, A. Skumanich, D. E. Rees, and G. A. Murphy. Stokes profile analysis and vector magnetic fields. IV - Synthesis and inversion of the chromospheric MG I B lines. *Astrophys. J.*, 330:493–512, 1988.

B. W. Lites, D. F. Elmore, K. V. Streander, C. M. Hoffmann, T. D. Tarbell, A. M. Title, R. A. Shine, K. Ichimoto, S. Tsuneta, T. Shimizu, and Y. Suematsu. Performance Characteristics of the Solar-B Spectro-Polarimeter. In K. Shibata, S. Nagata, and T. Sakurai, editors, *New Solar Physics with Solar-B Mission*, volume 369 of *Astronomical Society of the Pacific Conference Series*, pages 55–+, 2007.

D. H. Mackay and A. A. van Ballegooijen. Models of the Large-Scale Corona. II. Magnetic Connectivity and Open Flux Variation. *Astrophys. J.*, 642:1193–1204, 2006.

P. Maltby. The chromospheric Evershed flow. *Solar Phys.*, 43:91–105, 1975.

V. Mártinez Pillet, M. Collados, J. Sánchez Almeida, V. González, A. Cruz-Lopez, A. Manescau, E. Joven, E. Paez, J. Diaz, O. Feeney, V. Sánchez, G. Scharmer, and D. Soltau. LPSP & TIP: Full Stokes Polarimeters for the Canary Islands Observatories. In T. R. Rimmele, K. S. Balasubramaniam, and R. R. Radick, editors, *High Resolution Solar Physics: Theory, Observations, and Techniques*, volume 183 of *Astronomical Society of the Pacific Conference Series*, pages 264–+, 1999.

F. Meyer and H. U. Schmidt. Magnetically Aligned Flows in the Solar Atmosphere. *Astronomical Journal, Vol. 73, p. 71*, 73:71–+, 1968.

C. E. Moore, M. G. J. Minnaert, and J. Houtgast. *The solar spectrum 2935 A to 8770 A*. National Bureau of Standards Monograph, Washington: US Government Printing Office (USGPO), 1966, 1966.

K. Nagaraju, K. B. Ramesh, K. Sankarasubramanian, and K. E. Rangarajan. An efficient modulation scheme for dual beam polarimetry. *Bulletin of the Astronomical Society of India*, 35:307–318, 2007.

K. Nagaraju, K. Sankarasubramanian, and K. E. Rangarajan. On the Weakening of the Chromospheric Magnetic Field in Active Regions. *Astrophys. J.*, 678:531–540, 2008a.

K. Nagaraju, K. Sankarasubramanian, K. E. Rangarajan, K. B. Ramesh, J. Singh, P. Devendran, and Hariharan. On the Performance of a Dual-Beam Polarimeter at Kodaikanal Tower Telescope. 2008b.

H. P. Povel, C. U. Keller, and J. O. Stenflo. Two-dimensional polarimeter with CCD image sensors and piezo-elastic modulators. In *11. National Solar Observatory / Sacramento Peak Summer Workshop: Solar polarimetry, p. 100 - 112*, pages 100–112, 1991.

D. N. Rachkovsky. . *Izv. Krymsk. Astrofiz. Obs.*, 27:148–+, 1962.

D. E. Rees. *A Gentle Introduction to Polarized Radiative Transfer*, pages 213–+. Numerical Radiative Transfer, 1987.

D. E. Rees and M. D. Semel. Line formation in an unresolved magnetic element - A test of the centre of gravity method. *Astron. Astrophys.*, 74:1–5, 1979.

T. Rimmele. On the Relation between Umbral Dots, Dark-cored Filaments, and Light Bridges. *Astrophys. J.*, 672:684–695, 2008.

T. Rimmele and J. Marino. The Evershed Flow: Flow Geometry and Its Temporal Evolution. *Astrophys. J.*, 646:593–604, 2006.

T. R. Rimmele. Evidence for thin elevated evershed channels. *Astron. Astrophys.*, 298:260–+, 1995.

B. Ruiz Cobo and J. C. del Toro Iniesta. Inversion of Stokes profiles. *Astrophys. J.*, 398:375–385, 1992.

R. J. Rutten. Observing the Solar Chromosphere. In P. Heinzel, I. Dorotovič, and R. J. Rutten, editors, *The Physics of Chromospheric Plasmas*, volume 368 of *Astronomical Society of the Pacific Conference Series*, pages 27–+, 2007.

J. Sanchez Almeida. Physical Properties of the Solar Magnetic Photosphere under the MISMA Hypothesis. I. Description of the Inversion Procedure. *Astrophys. J.*, 491:993–+, 1997.

J. Sanchez Almeida and B. W. Lites. Observation and interpretation of the asymmetric Stokes Q, U, and V line profiles in sunspots. *Astrophys. J.*, 398:359–374, 1992.

K. Sankarasubramanian. *Solar polarimetry: techniques and applications*. PhD thesis, Bangalore University, 2000.

K. Sankarasubramanian and T. Rimmele. Bisector Analysis of Stokes Profiles: Effects Due to Gradients in the Physical Parameters. *Astrophys. J.*, 576:1048–1063, 2002.

K. Sankarasubramanian, J. P. A. Samson, and P. Venkatakrishnan. Measurement of instrumental polarisation of the Kodaikanal tunnel tower telescope. In K. N.

Nagendra and J. O. Stenflo, editors, *Polarization*, volume 243 of *Astrophysics and Space Science Library*, pages 313–320, 1999.

K. Sankarasubramanian, C. Gullixson, S. Hegwer, T. R. Rimmele, S. Gregory, T. Spence, S. Fletcher, K. Richards, E. Rousset, B. Lites, D. Elmore, K. Streander, and M. Sigwarth. The Diffraction Limited Spectro-Polarimeter: a new instrument for high-resolution solar polarimetry. In S. Fineschi and M. A. Gummin, editors, *Telescopes and Instrumentation for Solar Astrophysics. Edited by Fineschi, Silvano; Gummin, Mark A. Proceedings of the SPIE, Volume 5171, pp. 207-218 (2004).*, volume 5171 of *Presented at the Society of Photo-Optical Instrumentation Engineers (SPIE) Conference*, pages 207–218, 2004.

G. B. Scharmer, B. V. Gudiksen, D. Kiselman, M. G. Löfdahl, and L. H. M. Rouppe van der Voort. Dark cores in sunspot penumbral filaments. *Nature*, 420:151–153, 2002.

G. B. Scharmer, K. Langhans, D. Kiselman, and M. G. Löfdahl. Recent High Resolution Observations and Interpretations of Sunspot Fine Structure. In K. Shibata, S. Nagata, and T. Sakurai, editors, *New Solar Physics with Solar-B Mission*, volume 369 of *Astronomical Society of the Pacific Conference Series*, pages 71–+, 2007.

G. B. Scharmer, Å. Nordlund, and T. Heinemann. Convection and the Origin of Evershed Flows in Sunspot Penumbrae. *Astrophys. J. Lett.*, 677:L149–L152, 2008.

P. H. Scherrer, R. S. Bogart, R. I. Bush, J. T. Hoeksema, A. G. Kosovichev, J. Schou, W. Rosenberg, L. Springer, T. D. Tarbell, A. Title, C. J. Wolfson, I. Zayer, and

MDI Engineering Team. The Solar Oscillations Investigation - Michelson Doppler Imager. *Solar Phys.*, 162:129–188, 1995.

R. Schlichenmaier. The Sunspot Penumbra: New Developments (Invited review). In A. A. Pevtsov and H. Uitenbroek, editors, *Current Theoretical Models and Future High Resolution Solar Observations: Preparing for ATST*, volume 286 of *Astronomical Society of the Pacific Conference Series*, pages 211–+, 2003.

R. Schlichenmaier and M. Collados. Spectropolarimetry in a sunspot penumbra. Spatial dependence of Stokes asymmetries in Fe I 1564.8 nm. *Astron. Astrophys.*, 381:668–682, 2002.

R. Schlichenmaier and W. Schmidt. Flow geometry in a sunspot penumbra. *Astron. Astrophys.*, 358:1122–1132, 2000.

R. Schlichenmaier, K. Jahn, and H. U. Schmidt. Magnetic flux tubes evolving in sunspots. A model for the penumbral fine structure and the Evershed flow. *Astron. Astrophys.*, 337:897–910, 1998a.

R. Schlichenmaier, K. Jahn, and H. U. Schmidt. A Dynamical Model for the Penumbral Fine Structure and the Evershed Effect in Sunspots. *Astrophys. J. Lett.*, 493: L121+, 1998b.

R. Schlichenmaier, L. R. Bellot Rubio, and A. Tritschler. Two-dimensional spectroscopy of a sunspot. II. Penumbral line asymmetries. *Astron. Astrophys.*, 415: 731–737, 2004.

W. Schmidt and R. Schlichenmaier. Small-scale flow field in a sunspot penumbra. *Astron. Astrophys.*, 364:829–834, 2000.

C. J. Schrijver. A Characteristic Magnetic Field Pattern Associated with All Major Solar Flares and Its Use in Flare Forecasting. *Astrophys. J. Lett.*, 655:L117–L120, 2007.

C. J. Schrijver, M. L. DeRosa, T. Metcalf, G. Barnes, B. Lites, T. Tarbell, J. McTiernan, G. Valori, T. Wiegelmann, M. S. Wheatland, T. Amari, G. Aulanier, P. Démoulin, M. Fuhrmann, K. Kusano, S. Régnier, and J. K. Thalmann. Nonlinear Force-free Field Modeling of a Solar Active Region around the Time of a Major Flare and Coronal Mass Ejection. *Astrophys. J.*, 675:1637–1644, 2008.

M. Semel, J.-F. Donati, and D. E. Rees. Zeeman-Doppler imaging of active stars. 3: Instrumental and technical considerations. *Astron. Astrophys.*, 278:231–237, 1993.

A. Skumanich and B. W. Lites. Stokes profile analysis and vector magnetic fields. I - Inversion of photospheric lines. *Astrophys. J.*, 322:473–482, 1987.

H. Socas-Navarro. Stokes Inversion Techniques: Recent Achievements and Future Horizons. In M. Sigwarth, editor, *Advanced Solar Polarimetry – Theory, Observation, and Instrumentation*, volume 236 of *Astronomical Society of the Pacific Conference Series*, pages 487–+, 2001.

H. Socas-Navarro. The Three-dimensional Structure of a Sunspot Magnetic Field. *Astrophys. J. Lett.*, 631:L167–L170, 2005.

H. Socas-Navarro and H. Uitenbroek. On the Diagnostic Potential of Hα for Chromospheric Magnetism. *Astrophys. J. Lett.*, 603:L129–L132, 2004.

H. Socas-Navarro, B. Ruiz Cobo, and J. Trujillo Bueno. Non-LTE Inversion of Line Profiles. *Astrophys. J.*, 507:470–481, 1998.

H. Socas-Navarro, J. Trujillo Bueno, and B. Ruiz Cobo. Non-LTE Inversion of Stokes Profiles Induced by the Zeeman Effect. *Astrophys. J.*, 530:977–993, 2000.

H. Socas-Navarro, D. Elmore, A. Pietarila, A. Darnell, B. W. Lites, S. Tomczyk, and S. Hegwer. Spinor: Visible and Infrared Spectro-Polarimetry at the National Solar Observatory. *Solar Phys.*, 235:55–73, 2006.

S. K. Solanki. Sunspots: An overview. *Astron. Astrophys. Rev.*, 11:153–286, 2003.

S. K. Solanki, A. Lagg, J. Woch, N. Krupp, and M. Collados. Three-dimensional magnetic field topology in a region of solar coronal heating. *Nature*, 425:692–695, 2003.

H. C. Spruit and G. B. Scharmer. Fine structure, magnetic field and heating of sunspot penumbrae. *Astron. Astrophys.*, 447:343–354, 2006.

C. E. St. John. Radial Motion in Sun-Spots. *Astrophys. J.*, 37:322–+, 1913.

J. O. Stenflo. Solar magnetic and velocity-field measurements: new instrument concepts. *Appl. Optics*, 23:1267–, 1984.

J. O. Stenflo, editor. *Solar magnetic fields: polarized radiation diagnostics*, volume 189 of *Astrophysics and Space Science Library*, 1994.

J. O. Stenflo and H. Povel. Astronomical polarimeter with 2-D detector arrays. *Appl. Optics*, 24:3893–3898, 1985.

J. O. Stenflo, C. U. Keller, and H. P. Povel. Demodulation of all four Stokes parameters with a single CCD - ZIMPOL II. Conceptual design. *LEST Found., Tech. Rep., No. 54,*, 54, 1992.

A. C. Sterling and R. L. Moore. External and Internal Reconnection in Two Filament-Carrying Magnetic Cavity Solar Eruptions. *Astrophys. J.*, 613:1221–1232, 2004.

M. Stix. *The sun : an introduction.* The sun : an introduction, 2nd ed., by Michael Stix. Astronomy and astrophysics library, Berlin: Springer, 2004. ISBN: 3540207414, 2004.

G. G. Stokes. On the composition and resolution of streams of polarized light from different sources. *Trans. Cambridge Phil. Soc.*, 9:399–450, 1852.

P. A. Sturrock. The role of eruption in solar flares. *Solar Phys.*, 121:387–397, 1989.

K. F. Tapping, D. Boteler, P. Charbonneau, A. Crouch, A. Manson, and H. Paquette. Solar Magnetic Activity and Total Irradiance Since the Maunder Minimum. *Solar Phys.*, 246:309–326, 2007.

J. H. Thomas. Evershed Flows along Penumbral Flux Tubes in Sunspots. In J. Leibacher, R. F. Stein, and H. Uitenbroek, editors, *Solar MHD Theory and Observations: A High Spatial Resolution Perspective*, volume 354 of *Astronomical Society of the Pacific Conference Series*, pages 224–+, 2006.

J. H. Thomas and B. Montesinos. A siphon-flow model of the photospheric Evershed flow in a sunspot. *Astrophys. J.*, 407:398–401, 1993.

A. Tritschler, R. Schlichenmaier, L. R. Bellot Rubio, the KAOS Team, T. Berkefeld, and T. Schelenz. Two-dimensional spectroscopy of a sunspot. I. Properties of the penumbral fine structure. *Astron. Astrophys.*, 415:717–729, 2004.

S. Tsuneta, K. Ichimoto, Y. Katsukawa, S. Nagata, M. Otsubo, T. Shimizu, Y. Suematsu, M. Nakagiri, M. Noguchi, T. Tarbell, A. Title, R. Shine, W. Rosenberg, C. Hoffmann, B. Jurcevich, G. Kushner, M. Levay, B. Lites, D. Elmore, T. Matsushita, N. Kawaguchi, H. Saito, I. Mikami, L. D. Hill, and J. K. Owens. The Solar Optical Telescope for the Hinode Mission: An Overview. *Solar Phys.*, 249: 167–196, 2008.

H. Uitenbroek. The Accuracy of the Center-of-Gravity Method for Measuring Velocity and Magnetic Field Strength in the Solar Photosphere. *Astrophys. J.*, 592: 1225–1233, 2003.

W. Unno. Line Formation of a Normal Zeeman Triplet. *Pub. Astron. Soc. Japan*, 8:108–+, 1956.

J. E. Vernazza, E. H. Avrett, and R. Loeser. Structure of the solar chromosphere. III - Models of the EUV brightness components of the quiet-sun. *Astrophys. J. Suppl.*, 45:635–725, 1981.

J.-X. Wang and Z.-X. Shi. An instance of the localized chromospheric polarity reversal. *Chinese Astronomy and Astrophysics*, 16:325–330, 1992.

N. O. Weiss. Sunspot Structure and Dynamics. *Space Science Reviews*, 124:13–22, 2006.

C. Westendorp Plaza, J. C. del Toro Iniesta, B. Ruiz Cobo, V. Martinez Pillet, B. W. Lites, and A. Skumanich. Evidence for a downward mass flux in the penumbral region of a sunspot. *Nature*, 389:47–+, 1997.

C. Westendorp Plaza, J. C. del Toro Iniesta, B. Ruiz Cobo, and V. M. Pillet. Optical Tomography of a Sunspot. III. Velocity Stratification and the Evershed Effect. *Astrophys. J.*, 547:1148–1158, 2001a.

C. Westendorp Plaza, J. C. del Toro Iniesta, B. Ruiz Cobo, V. M. Pillet, B. W. Lites, and A. Skumanich. Optical Tomography of a Sunspot. II. Vector Magnetic Field and Temperature Stratification. *Astrophys. J.*, 547:1130–1147, 2001b.

S. M. White, M. R. Kundu, and N. Gopalswamy. Strong magnetic fields and inhomogeneity in the solar corona. *Astrophys. J. Lett.*, 366:L43–L46, 1991.

Appendix A: Mueller Matrices

The polarization properties of an optical component can be represented through a 4×4 matrix. For e.g., Mueller matrix of a linear polarizer with its fast axis at angle θ with respect to a chosen reference is given by

$$\mathbf{M_P}(\theta) = \begin{pmatrix} 1 & c_2 & s_2 & 0 \\ c_2 & c_2^2 & c_2 s_2 & 0 \\ s_2 & c_2 s_2 & s_2^2 & 0 \\ 0 & 0 & 0 & 0 \end{pmatrix},$$

and linear retarder of retardance δ with its fast axis at an angle with the chosen reference is given by

$$\mathbf{M_R}(\theta, \delta) = \begin{pmatrix} 1 & 0 & 0 & 0 \\ 0 & c_2^2 + s_2^2 \cos\delta & c_2 s_2 (1 - \cos\delta) & -s_2 \sin\delta \\ 0 & c_2 s_2 (1 - \cos\delta) & s_2^2 + c_2^2 \cos\delta & c_2 \sin\delta \\ 0 & s_2 \sin\delta & -c_2 \sin\delta & \cos\delta \end{pmatrix},$$

where $c_2 = \cos 2\theta$, $s_2 = \sin 2\theta$.

If $\mathbf{S}_{in}$ and $\mathbf{S}_{op}$ represent the input and output Stokes vectors of an optical system composed of n separate optical components whose polarization properties are

described by the Mueller matrices $\mathbf{M}_i$, with $i = 1, 2, ...n$. Then we can write

$$\mathbf{S}_{op} = \mathbf{M}\mathbf{S}_{in}, \tag{6.1}$$

where

$$\mathbf{M} = \mathbf{M_n}\mathbf{M_{n-1}}.....\mathbf{M_1}, \tag{6.2}$$

with $\mathbf{M_1}$ being the first element to be encountered by the light and $\mathbf{M_n}$ being the last.

Appendix B: Matrix Structures Related to Polarimeter Calibration

The structure of the measured Stokes signal matrix in Eq. (3.3) is given by

$$\mathbf{S}_{op}^{c} = \begin{pmatrix} S_{op}^{1}(0) & S_{op}^{1}(1) & S_{op}^{1}(2) & S_{op}^{1}(3) \\ S_{op}^{2}(0) & S_{op}^{2}(1) & S_{op}^{2}(2) & S_{op}^{2}(3) \\ S_{op}^{3}(0) & S_{op}^{3}(1) & S_{op}^{3}(2) & S_{op}^{3}(3) \\ S_{op}^{4}(0) & S_{op}^{4}(1) & S_{op}^{4}(2) & S_{op}^{4}(3) \\ S_{op}^{5}(0) & S_{op}^{5}(1) & S_{op}^{5}(2) & S_{op}^{5}(3) \\ S_{op}^{6}(0) & S_{op}^{6}(1) & S_{op}^{6}(2) & S_{op}^{6}(3) \\ S_{op}^{7}(0) & S_{op}^{7}(1) & S_{op}^{7}(2) & S_{op}^{7}(3) \\ S_{op}^{8}(0) & S_{op}^{8}(1) & S_{op}^{8}(2) & S_{op}^{8}(3) \\ S_{op}^{9}(0) & S_{op}^{9}(1) & S_{op}^{9}(2) & S_{op}^{9}(3) \\ S_{op}^{10}(0) & S_{op}^{10}(1) & S_{op}^{10}(2) & S_{op}^{10}(3) \\ S_{op}^{11}(0) & S_{op}^{11}(1) & S_{op}^{11}(2) & S_{op}^{11}(3) \\ S_{op}^{12}(0) & S_{op}^{12}(1) & S_{op}^{12}(2) & S_{op}^{12}(3) \\ S_{op}^{13}(0) & S_{op}^{13}(1) & S_{op}^{13}(2) & S_{op}^{13}(3) \end{pmatrix},$$

and that of input Stokes matrix is given by

$$\mathbf{S}_{in}^{c} = \begin{pmatrix} S_{in}^{1}(0) & S_{in}^{1}(1) & S_{in}^{1}(2) & S_{in}^{1}(3) \\ S_{in}^{2}(0) & S_{in}^{2}(1) & S_{in}^{2}(2) & S_{in}^{2}(3) \\ S_{in}^{3}(0) & S_{in}^{3}(1) & S_{in}^{3}(2) & S_{in}^{3}(3) \\ S_{in}^{4}(0) & S_{in}^{4}(1) & S_{in}^{4}(2) & S_{in}^{4}(3) \\ S_{in}^{5}(0) & S_{in}^{5}(1) & S_{in}^{5}(2) & S_{in}^{5}(3) \\ S_{in}^{6}(0) & S_{in}^{6}(1) & S_{in}^{6}(2) & S_{in}^{6}(3) \\ S_{in}^{7}(0) & S_{in}^{7}(1) & S_{in}^{7}(2) & S_{in}^{7}(3) \\ S_{in}^{8}(0) & S_{in}^{8}(1) & S_{in}^{8}(2) & S_{in}^{8}(3) \\ S_{in}^{9}(0) & S_{in}^{9}(1) & S_{in}^{9}(2) & S_{in}^{9}(3) \\ S_{in}^{10}(0) & S_{in}^{10}(1) & S_{in}^{10}(2) & S_{in}^{10}(3) \\ S_{in}^{11}(0) & S_{in}^{11}(1) & S_{in}^{11}(2) & S_{in}^{11}(3) \\ S_{in}^{12}(0) & S_{in}^{12}(1) & S_{in}^{12}(2) & S_{in}^{12}(3) \\ S_{in}^{13}(0) & S_{in}^{13}(1) & S_{in}^{13}(2) & S_{in}^{13}(3) \end{pmatrix}.$$

Where $\mathbf{S}_{op}^{j}(i)$ and $\mathbf{S}_{in}^{j}(i)$, $j = 1.....13$ correspond to 13 orientations of the calibration retarder and $i = 0, 1, 2, 3$ corresponding to Stokes I,Q,U,V are the measured Stokes signals and input Stokes parameters respectively.

Appendix C: Space Based Instruments

Some of the data from the space based observations have been used in this thesis for a comprehensive study of the structuring of the velocity and magnetic fields in the active regions. Only a few relevant details are given in this appendix. Further details can be found in the papers which give the overviews of these instruments given in the respective sections.

SOT and XRT Onboard *Hinode*

The Solar Optical Telescope (SOT) is a 50 cm diffraction-limited Gregorian telescope. For eg., the diffraction limited spatial resolution is $\approx 0.32''$ at λ6300. The focal plane instruments of SOT include spectropolarimeter (SP) and filtergraphs (FG). Using FG assembly, high resolution narrow band images of the selected region on the Sun are obtained in various wavelengths. In this thesis we have used filtergrams centered around λ4305, the wavelength band well known as G-band. The FOV of FG is 328 $\times$ 164 arcsec^2. Two dimensional images of Stokes parameters are also obtained using FG. On the otherhand SP provide full Stokes profiles of Fe I λ6301.5/6302.5 lines. This is an off-axis Littrow Echelle spectrograph and is a dual-beam system. The solar image is stepped across the slit to map an ROI, upto $320''$ FOV. See Tsuneta et al. [2008] for an overview of SOT instruments.

X-ray Telescope (XRT) is a grazing incidence telescope. The plate scale of this telescope is $1.2''$ with a spatial resolution of $\approx 2''$. Limits of temperature coverage is

1.2 to 30 MK. See a review by Golub et al. [2007] about XRT.

EIT Onboard *SOHO*

Extreme-ultraviolet Imaging Telescope (EIT) is a telescope of Ritchey-Chretien design for full disk coronal and transition images of the Sun. The telescope has a $45'' \times 45''$ field of view and $5''$ spatial resolution with a plate scale of $2''$/pixel. The temperature sensitivity of this telescope is 0.08 MK to 2 MK. More details on EIT can be found in a paper by Delaboudinière et al. [1995].